DECOMPOSITION OF AUSTENITIC MANGANESE STEELS CONTAINING MOLYBDENUM

K. F. DOLMAN

B. App. Sc. (Adelaide).

A thesis submitted for the degree of Master of Applied Science in December, 1979. The investigation was carried out in the Materials Engineering Group, Chemical Engineering Department, University of Adelaide.

D E C L A R A T I O N

This thesis contains no material which has been accepted for the award of any other degree in any university, and to the best of the author's knowledge and belief contains no previously published material or that written by any other person except where due reference is made or common knowledge is assumed.

K.F. DOLMAN

A C K N O W L E D G E M E N T S

The author wishes to thank his supervisors, Professor D.R. Miller and Dr. G.J. Cocks for their assistance in the preparation of this thesis. Particular thanks are also due to M.H. Ainsley for his advice and critical appraisal at various stages of this work.

S U M M A R Y

Austenitic manganese steels containing molybdenum decompose during isothermal ageing in the temperature interval 300-900^{o}C to produce five quite distinct transformation reaction products: (i) Widmanstatten Cementite, $(Fe,Mn)_3C$; (ii) proeutectoid grain boundary and intragranular carbide identified as $M_{23}C_6$; (iii) alloy pearlite consisting of $M_{23}C_6$ and ferrite; (iv) discontinuous precipitation of $M_{23}C_6$ + solute depleted austenite; (v) a heterogeneous matrix precipitation of Mo_2C in austenite.

The Widmanstatten Cementite is the only transformation reaction product identical with that occurring in the basic austenitic manganese steel system, whereas the grain boundary $M_{23}C_6$ carbide and the alloy pearlite reactions are analogous to the proeutectoid and pearlitic cementite transformation products observed in Hadfield steel. The $M_{23}C_6$ carbide (fcc) was shown to exhibit a simple cube-cube orientation relationship with the adjacent austenite grain and the alloy pearlite constituents display the familiar Kurdjumov-Sachs relation between bcc and fcc structures.

It is shown that Mo_2C precipitation on dislocations is the primary mode of nucleation and growth of the heterogeneous matrix reaction which occurs at elevated ageing temperatures (above 600^{o}C). A simultaneous transformation reaction of grain boundary nucleated coarse lamellar $M_{23}C_6$ + solute depleted austenite, shown to be a classical example of discontinuous precipitation, also occurs within a narrow composition limit.

TABLE OF CONTENTS

CHAPTER 1

1. SCOPE OF PRESENT WORK

1.1 Introduction

The isothermal decomposition of austenite to ferrite in low alloy steels containing the addition of strong carbide forming elements (Cr, Mo, V, W, Nb, Ti) is accompanied by the precipitation of alloy carbides at the advancing α/γ boundary. A number of different alloy carbide dispersions, including a pearlitic form, fine fibres and banded arrays of fine, discrete particles, are formed during the transformation reaction. These morphologies are influenced by the composition of the carbide phase, the growth kinetics of the ferrite and the crystallographic nature of the advancing α/γ boundary. Although the first two factors have been well documented in a recent review by Honeycombe (1976), crystallographic studies of the α/γ boundary interface have proved difficult due to the instability of the parent austentite which transforms to martensite on subsequent cooling to room temperature.

In a recent study of the isothermal decomposition of austenite to pearlite (Dippenaar and Honeycombe 1973) the problem of the transformation of the retained austenite to martensite on cooling was circumvented by using a high manganese steel. After partial transformation of the alloy Fe-13Mn-0.8C (compositions are expressed in weight percent) pearlite and retained austenite coexisted at room temperature permitting a complete crystallographic examination of the reaction. During the course of that work the precipitation of vanadium carbide in association with stable austenite was briefly reported on ageing the alloy Fe-13Mn-2V-0.8C (Dippenaar 1970).

This alloy was investigated in greater detail (Ainsley et al. 1979) and a number of quite distinct transformation reactions were reported during isothermal ageing over a wide temperature range. In particular, in the temperature interval 550-710^{o}C, discontinuous precipitation of fibrous and extremely fine particulate vanadium carbide to austenite was observed and the reaction is described by the expression:

$$\gamma_1 \longrightarrow \gamma_2 + VC$$

The fine discontinuous precipitation (d.p.) reaction was recognised as being eminently suitable for crystallographic analysis for a number of reasons. Firstly, the untransformed austenite (γ_1) remained stable at room temperature. Secondly, the vanadium carbide adopted a simple cube-cube orientation relationship with the advancing austenite phase (γ_2) which was also stable at room temperature. Thirdly, the application of the Coincident Site Lattice Model to the crystallographic analysis of the advancing austenite boundary (γ_1/γ_2) was directly amenable since it involved grains of the same crystal structure. As a result of these investigations it was shown that fibrous vanadium carbide formed behind advancing planar boundaries that exhibited a high density of coincidence lattice sites and that particulate VC formed being non-planar boundaries that had a low density of coincidence sites.

1.2 Aim of Present Work

The aim of the present investigation was to examine the isothermal transformation characteristics of austenitic manganese steels containing the addition of alternative strong carbide forming elements in the anticipation of observing similar d.p. reactions.

1.3 Scope of Present Work

A preliminary investigation of the effect of the addition of strong carbide forming elements on the ageing characteristics of austenitic manganese steel was undertaken to delineate an alloy composition suitable for examination. Initially titanium and niobium were considered since it has been shown that Fe-C alloys containing Ti and Nb as the principal carbide forming elements exhibit similar isothermal ageing behaviour to vanadium steels (Freeman 1971, Gray et al. 1968, Davenport et al. 1968). The reaction rates are comparable and the formation of carbides isomorphous with vanadium carbide (f.c.c. structure) occur. Microstructural examination of the following alloys, based on the published solid solubility limits of Ti and Nb in austenite (Aaronson 1969):

Fe-13Mn-0.8C-0.5Ti

Fe-13Mn-0.8C-0.5Nb

showed that, although age hardening due to continuous precipitation of alloy carbides occurred, no d.p. reactions were observed after prolonged ageing over a wide temperature range.

Indeed, it has been shown (Ainsley, private communication) that only continuous precipitation of VC occurred on ageing the alloy Fe-13Mn-0.8C-0.5V which is comparable in solute content to the above alloys and confirms previous observations (Hornbogen 1972) that the transition from continuous to discontinuous precipitation occurs with increasing supersaturation. Since the maximum solid solubility of Ti and Nb (approximately 0.5%) in austenitic manganese steels is much less than V (2.0%) it is suggested that the low level of solute saturation obtainable may be a contributing factor to the absence of a d.p. reaction in these alloys.

Thus the addition of molybdenum, which has a relatively high solid solubility in austenite, was considered since, all other conditions being equal, it appears that the concentration of the carbide forming element in solution in austenitic manganese steels is a significant factor in determining the nature of the transformation reactions on isothermal ageing.

An exploratory investigation of a number of Mo bearing austenitic manganese steels revealed several transformation reactions hitherto unreported in this alloy system. At elevated ageing temperatures (above 600°C) a fine fibrous and particulate precipitation reaction of Mo_2C in austenite formed over a wide composition range. A simultaneous transformation of a d.p. reaction of $M_{23}C_6$ associated with grain boundary migration occurred at the same temperatures over a narrow composition range. Below 600°C the austenite transformed to an alloy pearlite consisting of $M_{23}C_6$ + ferrite preceded by the formation of proeutectoid $M_{23}C_6$ and Widmanstatten cementite.

A detailed examination of the Fe-Mn-Mo-C system was subsequently undertaken to determine the factors controlling the presence and nature of these various transformation products. The results of a systematic variation in alloy composition on the ageing characteristics of this alloy system are outlined in Chapter 3. A brief examination of the transformation products that occurred on ageing below 600°C is also described. A study of the discontinuous and matrix precipitation reactions that occurred on ageing above 600°C is outlined in Chapter 4 together with an investigation of their mutual interactions.

The austenite phase in the host alloy, austenitic manganese steel, is metastable and undergoes a number of transformation reactions during isothermal ageing in the temperature range studied in this work. The stability of the austenite is also dependent on the solute carbon and manganese contents which vary during ageing as carbide is precipitated and martensite may be formed on subsequent cooling. Since these reactions complicate the microstructure rendering crystallographic studies difficult and mask age hardening effects, a review of the literature on austenitic manganese steels (Chapter 2) was undertaken in order to determine the range of compositions in the alloy system Fe-Mn-Mo-C that would yield stable austenite at room temperature after isothermal ageing.

CHAPTER 2

2. LITERATURE REVIEW OF AUSTENITIC MANGANESE STEELS

2.1 Introduction

When Hadfield announced the discovery of austenitic manganese steels in 1882 the practical implications of its unique properties were immediately recognised. Its principal virtues are: outstanding toughness, a high work hardening capacity and paramagnetism. The mechanical properties, in combination with the low cost of manganese and the simple casting and heat treatment procedures, render Hadfield steel almost indispensible in many industrial, heavy duty applications where resistance to abrasive wear under severe service conditions is demanded.

The nominal composition of austenitic manganese steels ranges from 1.0-1.4% carbon and 10-14% manganese. The austenitic structure is retained at room temperature by water quenching from 1050^{o}C to produce a soft, tough steel. During service the steel acquires a hardened surface layer by abrasion or impact loading. However, since Hadfield steel possesses a relatively low yield point, substantial dimensional changes occur in service before an effective surface hardened layer forms. In many cases this may be overcome by cold working prior to service but in other situations, where the component is a complex shape, this is not a practical approach.

Since the final toughening treatment necessary to develop the characteristic properties of manganese steels consists of rapid cooling from the solution treatment temperature (in order to maintain complete solution of the carbon in the retained austenite) the rate of quenching is important. The necessity to exceed a minimum critical cooling velocity throughout the mass being treated to prevent precipitation of carbides

imposes a limitation on the maximum size of section that may be effectively toughened. In practice this maximum section is restricted to about 125mm. Furthermore, the retained austenite in a suitably toughened steel will readily decompose during reheating, for example conventional welding operations, resulting in a loss in toughness due to carbide precipitation.

Austenitic manganese steels have been the subject of extensive research for nearly a century by a large number of workers in four main avenues of investigation:-

(a) The influence of carbon and manganese on the stability of the austenite phase after quenching from the solution treatment temperature.

(b) The effect of cold working on the structure and mechanical properties in an attempt to elucidate the nature of its high work hardening capacity.

(c) The isothermal decomposition of the retained austenite on reheating at elevated temperatures.

(d) The effect of alloying additions on its mechanical properties and isothermal transformation characteristics.

In the literature there are a number of contradictory results in these investigations which can be attributed to a variety of factors (Smith 1957, White et al. 1962). Firstly, there is a large variation in the initial compositions of the steels examined. This is further aggravated by the fact that austenitic manganese steels are very susceptible to segregation on solidification and to decarburization during heat

treatment. Secondly, because of the difficulties associated with the fabrication of high manganese steels, some workers inadvertantly induced work hardening and/or decomposition during specimen preparation. Finally, the significance of impurity elements such as silicon and phosphorous was not always considered.

2.2 Austenite Stability

The solution treatment of Hadfield steel followed by water quenching produces a single phase austenitic structure that imparts optimum mechanical properties (Oliver and Boyd 1956). The austenite is metastable and its retention on quenching is a function of composition (Hall 1966), temperature of the quenchant and the degree of subsequent cold working, Cina 1958, White et al. 1962). However, even though these conditions may be satisfied, decomposition of the retained austenite may occur during isothermal ageing at elevated temperatures to form a number of transformation products. This aspect of austenitic manganese steels will be examined in depth in a later Section.

The first systematic study of the retention of the austenite phase on quenching Fe-Mn-C alloys as a function of manganese and carbon contents was carried out by Bain et al. (1932). However, their results were subject to a systematic error since all of the alloys were solution treated at 950^{o}C for very short periods. Equilibrium conditions for the higher manganese steels were not achieved on solution treatment, and, furthermore, this temperature is below the solvus lines of the higher carbon steels investigated (Benz et al. 1973). The resultant microstructures of the steels within the Hadfield composition range contained austenite and undissolved carbide after quenching. Also, since the free carbon contents

of the remaining austenite were less than the reported analyses, some alloys exhibited a martensitic structure which is at variance with more recent investigators who reported the presence of austenite only (Maratray 1964, Bernshteyn 1977).

Four distinct structures have been reported in the Fe-Mn-C alloy system at various carbon and manganese contents after quenching from the solution treatment temperature:

(a) The austenite phase (γ_{fcc}, a = 0.360 nm) is an interstitial solid solution of carbon retained at room temperature on quenching and is metastable with respect to ferrite and $(Fe,Mn)_3C$ which readily form on reheating above 350°C.

(b) Alpha martensite (α_{bct}, a = 0.2859nm, a/c = 1.032) reported in the alloy Fe-6Mn-0.9C (Dautovich et al. 1972), is similar to that occurring in Fe-C alloys. However, the Ms is depressed from approximately 250°C in binary steels to well below room temperature in Fe-Mn-C alloys containing high manganese additions.

(c) Alpha prime martensite (α'_{bcc}, a = 0.2873nm) observed in Fe-Mn alloys (Holden et al. 1971, Grunes et al. 1972), has also been reported in the alloy Fe-12Mn-0.1C (Sedriks et al. 1964).

(d) Epsilon martensite (ε_{cph} a = 0.2541nm, a/c = 1.615) observed in the system Fe-26Mn-0.2C (Sipos 1975) is analogous to that occurring in austenitic Ni-Cr steels (Otte 1957, Cina 1958, Venables 1961, Mangonon et al. 1970 and Remy et al. 1974).

The transition γ_{fcc} to ε_{cph} may occur in fcc metals of low stacking fault energy (Remy et al. 1974) by the superpositioning of stacking faults on every second $(111)_{fcc}$ plane. Trioana et al. (1943), who reported the existence of ε_{cph} in Fe-Mn alloys, considered the structure to be a transition phase in the transformation reaction $\gamma_{fcc} \rightarrow \alpha'_{bcc}$. This view was reaffirmed by Cina (1957) who also observed an analogous process in the $\gamma_{fcc} \rightarrow \alpha_{bct}$ transformation in Fe-Mn-C alloys. Crocker (1962) suggested that the accomodation distortion for the reaction $\gamma_{fcc} \rightarrow \alpha'_{bcc}$ may be significantly reduced by the presence of an intermediate ε_{cph} phase. Grunes et al. (1972) examined the transformation of austenite in Fe-15Mn using electron microscopy techniques and found that α'_{bcc} nucleated as thin platelets at the intersection of two ε_{cph} laths and concluded that in this system the two stage reaction:-

$$\gamma_{fcc} \longrightarrow \varepsilon_{cph} \longrightarrow \alpha'_{bcc}$$

occurred with ε_{cph} acting as an intermediate phase in the decomposition of the austenite to α'_{bcc} martensite.

Although several investigators (Bain et al. 1932, Hall 1966) have examined the influence of carbon and manganese on the as-quenched structure of a number of Fe-Mn-C alloys no systematic review of the vast range of alloys reported in the literature has been published. A compilation of this data, indicating the approximate demarcation lines between austenite and the various martensite products, has been constructed by the author of the present work and is illustrated in Fig. 2.1.

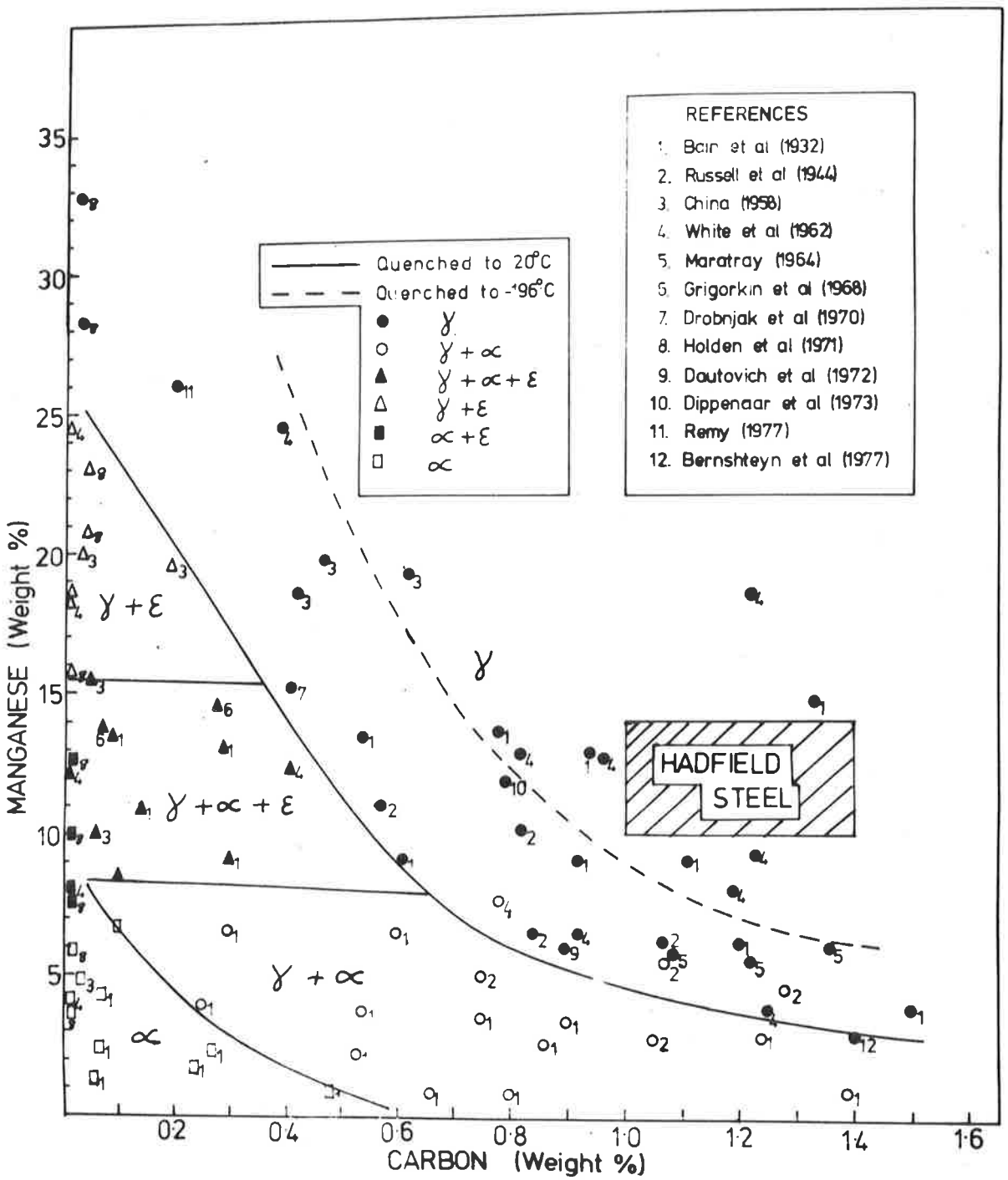

Fig. 2.1 Effect of alloy composition on the structure of solution treated and water quenched Fe-Mn-C Alloys.

It can be seen that the composition range of Hadfield steel lies well within the austenite region. High manganese-low carbon alloys exhibit $\gamma + \varepsilon$ martensite whereas low manganese-high carbon steels exhibit $\gamma + \alpha$ martensite. The boundaries of the 3 phase $\gamma + \alpha + \varepsilon$ structure observed at an intermediate composition range are only tentatively indicated due to a lack of sufficient data in the literature. Not included in the diagram is the α'_{bcc} structure which is formed at very low carbon levels in the range 0-15% Mn (Holden et al. 1971, Grunes et al. 1972).

Since high manganese steels are very susceptible to segregation on solidification (Collette et al. 1957), and decarburization on heating in air (Sedriks et al. 1966), this diagram may explain some of the discrepancies in the microstructures obtained by a number of investigators examining the Fe-Mn-C system. For example, the alloy Fe-13Mn-0,7C (wholly austenitic on quenching) has been shown to exhibit $\gamma + \alpha + \varepsilon$ on quenching after soaking in air at 1150-1200^{o}C for several hours (Grigorgin et al. 1968).

The composition limits of alloys whose microstructures are found to be austenitic on quenching to subzero temperatures (-196^{o}C) are also indicated in Fig. 2.1. Observations reported by White et al. (1962) tend to suggest that the retained austenite boundary line is shifted horizontally to the right and that the overall effect in the microstructures of the alloys on quenching to -196^{o}C is approximately equivalent to reducing the carbon content by about 0.3%.

The effect of subsequent cold working on the microstructures of quenched Fe-Mn-C alloys has been extensively investigated by a number of workers in an attempt to explain the high work hardening capacity of austenitic manganese steels. It has been found that both α and ε martensite may be induced in some alloys by deformation at room temperature. Although it is not possible to quantify the published data since different modes of deformation were used (slow compression, impact loading, rolling and tensile loading) the general effect observed is a vertical shift of the boundary lines in Fig. 2.1. For example, it has been shown that Fe-20Mn-0.2C ($\gamma + \varepsilon$) transforms to $\gamma + \alpha + \varepsilon$ (Cina 1958); while the alloy Fe-4Mn-1.2C (γ) transforms to $\gamma + \alpha$ (White et al. 1962).

Deformation at subzero temperatures has been observed to further enhance the presence of the martensitic structures. It has been shown that the alloy Fe-13Mn-0.8C, which remains wholly austenitic on quenching to subzero temperatures or after deformation at room temperature, transforms to $\gamma + \alpha + \varepsilon$ when deformed at $-196^{o}C$ (White et al. 1962). It is therefore proposed that the overall effect of deformation at subzero temperatures on the structure of quenched Fe-Mn-C alloys may be qualitatively described by a vertical and horizontal shift of the boundary lines in Fig. 2.1.

Detailed investigations of austenitic manganese steels of Hadfield composition, which lie well within the austenite region in the diagram, have shown that they remain wholly austenitic even after severe deformation at $-196^{o}C$ (Otte 1957, Cina 1958, White et al. 1962). Thus only those manganese steels with compositions close to the austenite boundary line are susceptible to martensitic transformation by cold working and/or quenching to subzero temperatures.

2.3 Work Hardening of Austenitic Manganese Steels

Although the mechanism responsible for the unusually high work hardening capacity of austenitic manganese steels has been the subject of extensive research and speculation by numerous investigators no conclusive evidence has yet been presented to satisfactorily explain this phenomena. Earlier views that work hardening resulted from decomposition of the austenite to martensite (Hall 1929, Krivobok 1929, Collette et al. 1957) have been discounted since it has been shown by electron microscopy studies that the structure remains wholly austenitic after severe deformation (Roberts 1964, Sastri 1973). It can be seen from Fig. 2.1 that carbon depletion of Hadfield steel by either localized segregation or decarburization during specimen preparation (as suggested by White et al. 1962) will result in a structural change to α and ε martensite.

Several investigators have attributed the high work hardening ability of Hadfield steel to its low stacking fault energy (10-20 mJ/m^2, Filippov et al. 1971). It has been shown from detailed electron microscopy techniques (Raghavan et al. 1969, Sastri 1973) that numerous intrinsic stacking faults are observed at small plastic strains. The individual stacking faults thicken with increased deformation to form twin lamellae which subdivide the original austenitic matrix into smaller domains. (Deformation twinning may occur in austenite by the superpositioning of stacking faults on every $(111)_\gamma$ plane (Remy et al. 1974)). It was concluded that work hardening was caused by the formation of a large number of twin boundaries which were observed to be effective barriers to dislocation movement.

Since the stacking fault energy of austenitic manganese steels decreases with decreasing temperature (Otte 1957) this mechanism would seem to account for the higher work hardening rate of Fe-13Mn-1.2C at subzero temperatures (White et al. 1962, Raghavan 1969). However, two difficulties arise with this suggested mechanism. First, a reduction in stacking fault energy brought about by decreasing the carbon content to say 0.8% results in a decrease rather than an increase in work hardening rate (White et al. 1962). Second, Hadfield steel still exhibits a high work hardening rate above 225^{o}C where, as Daster et al. (1979) have shown, mechanical twinning is no longer observed.

The suggested twinning mechanism for the high work hardening of austenitic manganese steels was discounted by Roberts (1964) when he noted that this process is also observed to Fe-Ni alloys (Cohen 1962) but does not produce the same hardening effect. He proposed that dislocation locking occurred in Hadfield steel during deformation either by segregation of the interstitial solute carbon or precipitation of a fine carbide dispersion. Sastri et al. (1974) also considered this approach when they found that heavily deformed austenitic manganese steel age hardened from 750 Hv to 850 Hv after heating at 350^{o}C for 3 hours. Although no evidence of carbide precipitation was detected by electron microscopy techniques, an indication of carbon clustering was obtained by Mossbauer Spectroscopy.

Daster et al. (1979) reported that the stress/strain curves of a commercial grade Hadfield steel exhibited serrated flow during tensile loading over a range of testing temperatures. Kinetic studies indicated

that this effect was related to volume diffusion of carbon in austenite and it was tentatively proposed that work hardening is caused by reorientation of C-Mn couples in the strain fields of dislocations by short range jumps of carbon atoms.

Thus current speculations on the work hardening mechanism of austenitic manganese steels tend to involve the interstitial solute carbon. This is not unexpected since Hadfield steel containing 1.2%C is an intensely supersaturated solid solution with perhaps the highest interstitial solute content of any ferrous alloy known at ambient temperature.

2.4 Isothermal Decomposition of Austenite

The austenite obtained on quenching high manganese steel is metastable and readily undergoes decomposition during isothermal ageing in the temperature range 300-700^{o}C (Irvine et al. 1956, Collette et al. 1957, Imai et al. 1962). The Fe-Mn-C equilibrium phase diagram indicates that the equilibrium structure of these steels at 600^{o}C consists of ferrite and carbide (Benz et al. 1973). The carbide, with the stoichiometric composition M_3C containing considerable amounts of manganese in solid solution, has an orthorhombic crystal structure whose unit cell dimensions increase with manganese content.

The microstructure of high manganese steels after partial transformation exhibits Widmanstatten cementite, grain boundary carbide and nodular pearlite colonies in an austenite matrix. The decomposition characteristics of a number of selected alloys published in the literature are reproduced in Fig. 2.2 where the C-curves represent the onset of the transformation reactions. The formation of pearlite on isothermal ageing of Hadfield

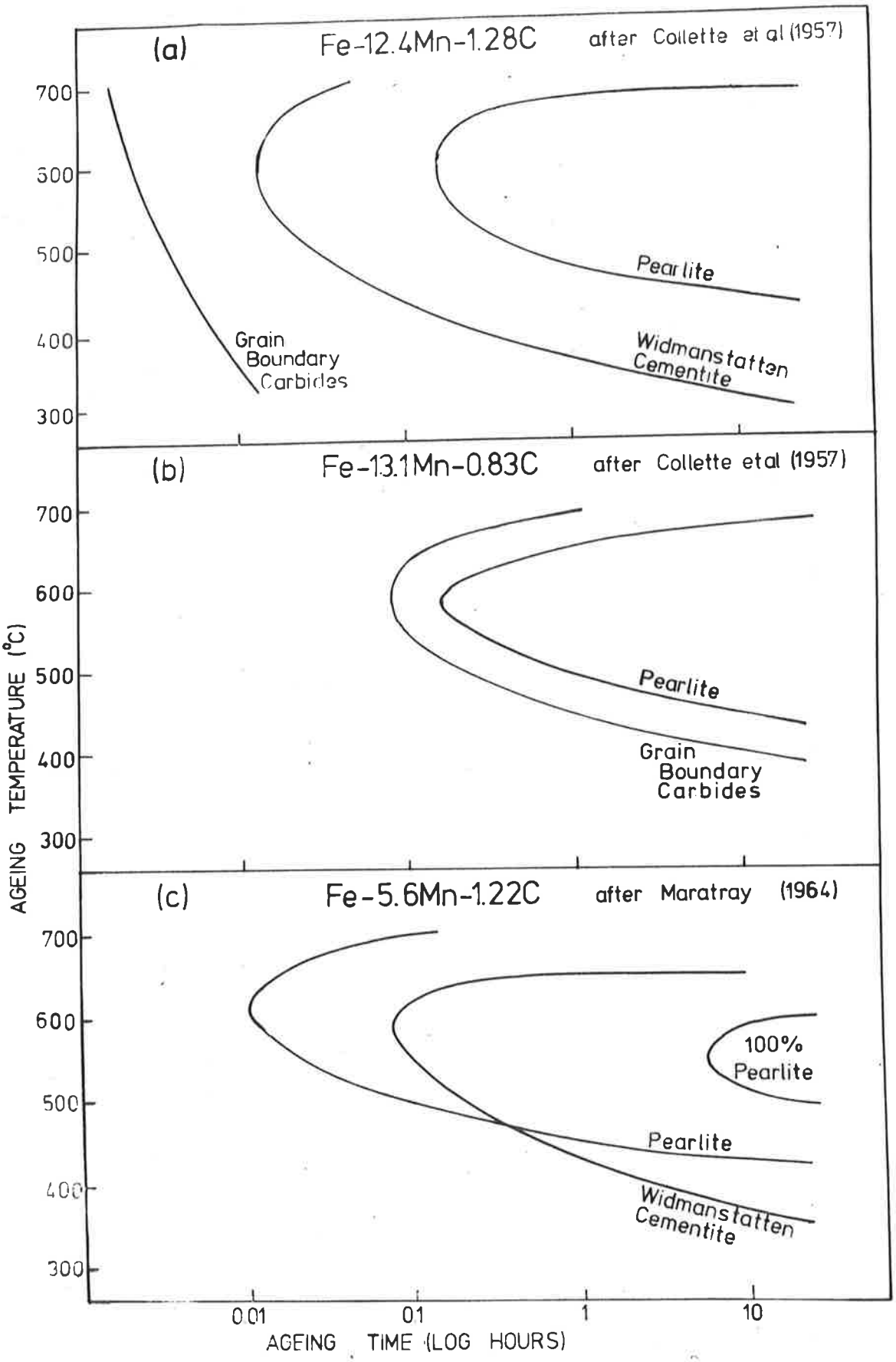

Fig. 2.2 *Isothermal Transformation characteristics of Austenitic manganese steels.*

steel (Fig. 2.2a) is preceded by the nucleation of proeutectoid cementite since the composition of the alloy is hyper-eutectoid (Rohrig 1974). A continuous film of grain boundary carbide forms almost immediately on ageing above 300°C and intragranular plates of Widmanstatten cementite initiate within one minute at about 550°C. Nodular pearlite colonies nucleate on the grain boundary carbide and Widmanstatten cementite at 600°C after an incubation period of 15 minutes. Transformation to 50% volume fraction of pearlite occurs at 500°C and it is estimated that approximately 5 years would be required for the reaction to go to completion (Imai et al. 1962).

A reduction in the carbon content to 0.8%(Fig. 2.2b) retards the formation of grain boundary carbides and eliminates the Widmanstatten cementite reaction on isothermal ageing. The onset of the pearlite reaction is unaffected but the maximum volume fraction transformed is only about 20% after 24 hours ageing (Dippenaar 1970).

Reducing the manganese content from 13% to 6% (Fig. 2.2c) greatly affects the kinetics of the transformation reactions. Although Maratray observed the presence of grain boundary carbides in this alloy the reaction was not included in the transformation diagram. However, this reaction is expected to be similar to that in Fig. 2.2a but shifted somewhat to the left. Above 450°C the pearlite reaction precedes the Widmanstatten cementite and goes to completion in 10 hours at 550°C.

The remaining austenite in high manganese steels that are partially transformed to pearlite undergoes a further transformation to ε martensite on subsequent cooling to room temperature (Nishiyama 1935, Isobe 1951, Collette et al. 1957). A gradually broadening layer of ε martensite is observed at room temperature in the austenite immediately ahead of the advancing pearlite colonies. Detailed examination of this martensitic reaction in the alloy Fe-13.7Mn-1.2C (Imai et al. 1962) using metallographic techniques supplemented by dilatrometry and X-ray difftraction has revealed that:-

(a) The remaining austenite, after ageing at 500^{o}C for 100 hours transforms fully to ε martensite on cooling to room temperature.

(b) The $\gamma \rightarrow \varepsilon$ transformation temperature on cooling is just above room temperature.

(c) The martensitic reaction is reversible and the $\varepsilon \rightarrow \gamma$ transformation occurs over the temperature range 200-280^{o}C on reheating.

The formation of ε martensite can be considered to be a result of a dynamic change in the composition of the remaining austenite as the pearlite reaction proceeds. Since it can be shown that the mean carbon content of pearlite nuclei is higher than the matrix it follows that the remaining austenite becomes carbon depleted by long range diffusion as the pearlite colonies advance. Thus it can be seen with reference to Fig. 2.1 that, as the carbon content is reduced, the austenite becomes less stable and has a greater tendency to form martensite on quenching. The absence of α martensite in the structure is not unexpected since

quenching is carried out from relatively low isothermal ageing temperatures (approximately 500^{o}C).

Imai et al. (1962) had proposed that long range diffusion of manganese during isothermal ageing was also significant in the formation of ε martensite. However, other studies by Collette et al. (1957) using electron beam micro-analysis techniques showed that there was no variation in manganese content between the austenite regions immediately ahead of the advancing pearlite and those far removed from the colonies.

Kinetic studies by Collette et al. (1957) have shown that the diffusion of manganese in the ferrite is the rate controlling process in the formation of pearlite in Fe-Mn-C alloys. Since the solid solubility of manganese in ferrite at the isothermal ageing temperatures is about 2% (Benz et al. 1973) partitioning of manganese occurs and the carbide $(Fe,Mn)_3C$ forms. This view is consistent with earlier observations that the pearlite transformation reaction rate increases with lower manganese content.

The effect of carbon content on the transformation rate of the pearlite reaction in high manganese steels is not quite as evident. A mechanism, suggested by the author of the present work to account for this influence, is outlined in Section 3.6.2.

The adverse effects of the transformation products on the mechanical properties obtained on ageing austenitic manganese steels have received considerable attention in the literature because of the wide practical

implications (Irvine et al. 1956, Oliver and Boyd 1956, Collette et al. 1957, Imai et al. 1962). The ductility of Hadfield steel is reduced from 65% elongation to less than 5% on isothermal ageing for one hour at 600°C. This loss in ductility is also accompanied by a substantial decrease in tensile strength. The influence of ageing for one hour over a wide temperature range on the mechanical properties of the alloy Fe-13Mn-1.2C is shown in Fig. 2.3. A dramatic decrease in the characteristic toughness of austenitic manganese steel begins at 400°C due to the precipitation of grain boundary and Widmanstatten cementite and is maintained up to 800°C where redissolution of the carbide occurs. Although tensile strength, elongation and reduction in area follow a similar pattern the yield strength remains constant over the entire ageing temperature range.

In contrast, there is an increase in hardness over the corresponding temperature interval. Imai et al. (1962) considered this to be due to the precipitation of Widmanstatten cementite but microhardness measurements of pearlite nodules by the author of the present work showed that this structure exhibited a hardness of 500-600Hv_{200g}. This relatively high value for pearlite is attributed to a number of factors: the extremely fine interlamellar spacing, the subgrain structure of the colonies and solution hardening of the ferrite phase which contains dissolved manganese. Wear tests have shown that the abrasion resistance of high manganese steel, isothermally transformed to 50% pearlite and exhibiting a gross hardness of 450Hv_{10}, is inferior to austenitic manganese steels. This may be due to a decrease in the work hardening capacity of the remaining austenite because of carbon depletion.

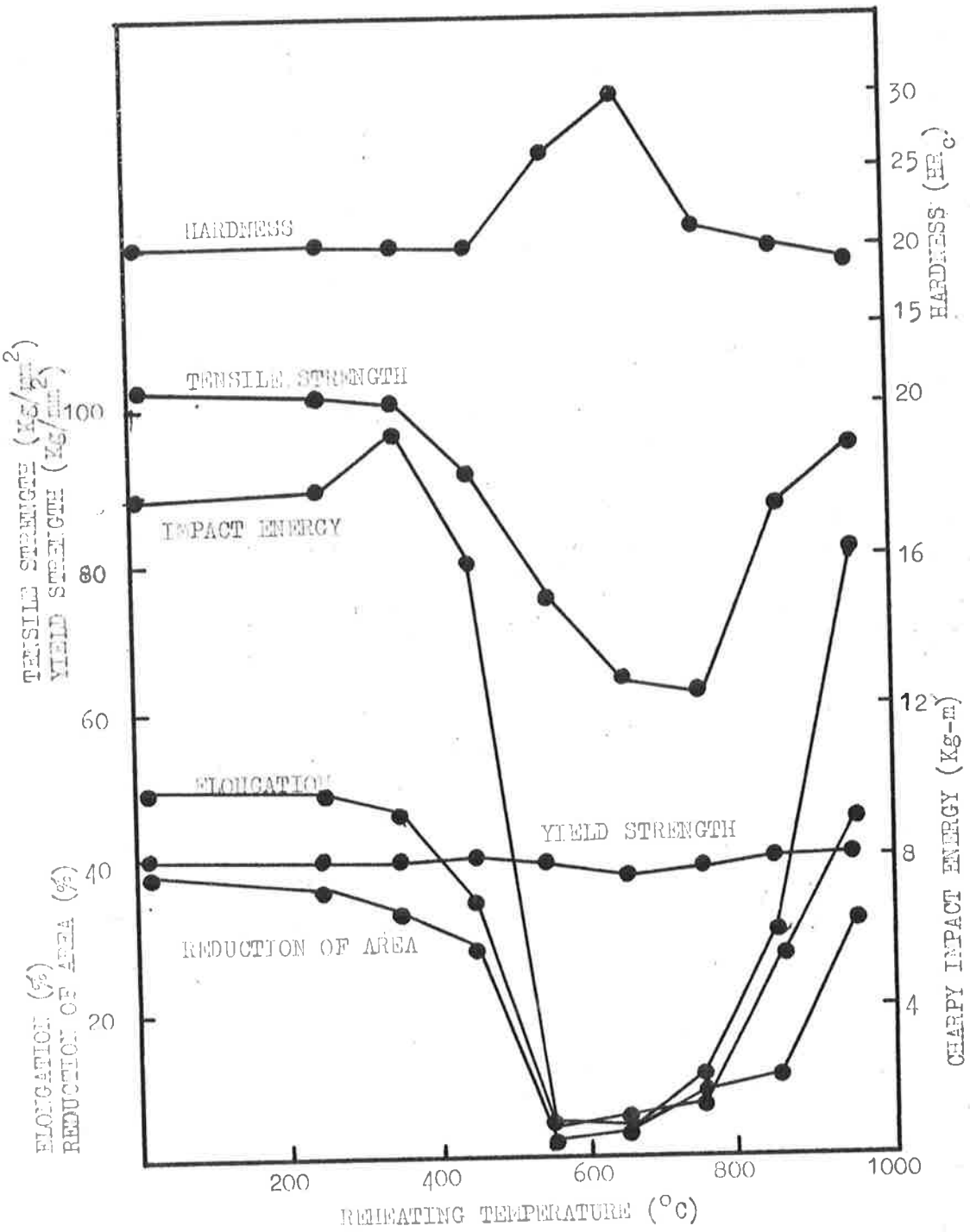

Fig.2.3 Fe-13Mn-1.2C
Effect of isothermal ageing for one hour on the mechanical properties tested at room temperature.

after Imai et al. (1962)

2.5 Crystallography of the Decomposition Products

2.5.1 Proeutectoid Cementite

(a) Widmanstatten cementite

The orientation relationship between Widmanstatten cementite and the adjacent austenite was determined in the alloy Fe-12.8Mn-1.28C, (Pitsch 1963), and the centres of the range of orientations were found to be:- Pitsch Relation

$$(0\ 0\ 1)_C \ //\ (\bar{2}\ 2\ 5)$$

$$(0\ 1\ 0)_C \ //\ (1\ 1\ 0)$$

$$(1\ 0\ 0)_C \ //\ (5\ \bar{5}\ 4)$$

This result has been confirmed by other investigators and agrees with the relations predicted by Sleeswyk (1966) and Jack (1974).

(b) Grain boundary cementite

Proeutectoid cementite also nucleates at austenite (γ_1/γ_2) grain boundaries and grows for a short distance into one of the austenite grains (γ_1) to form a continuous carbide network. It has been shown that the grain boundary cementite and the adjacent austenite grain (γ_2) into which it is not growing also exhibit the Pitsch relation (Dippenaar 1970).

2.5.2 Pearlite

In binary Fe-C steels two distinct crystallographic orientation relationships have been established between the cementite and ferrite phases (Ohmori et al. 1972).

(i) Pitsch-Petch Relation

$(1\ 0\ 0)_C$ 2.6° from $(1\ 3\ \bar{1})_\alpha$

$(0\ 1\ 0)_C$ 2.6° from $(1\ 1\ 3)_\alpha$

$(0\ 0\ 1)_C$ // $(5\ \bar{2}\ \bar{1})_\alpha$

(ii) Bagaryatski Relation

$(1\ 0\ 0)_C$ // $(0\ \bar{1}\ 1)_\alpha$

$(0\ 1\ 0)_C$ // $(1\ 1\ 1)_\alpha$

$(0\ 0\ 1)_C$ // $(2\ \bar{1}\ \bar{1})_\alpha$

Shackleton et al. (1969) investigated a number of pearlite colonies in the alloy Fe-12.8Mn-1.15C and found that the pearlite constituents exhibited both the Pitsch-Petch and Bagarystski orientation relationships indicating that there is a strong similarity in the nucleation process of pearlite in plain carbon and austenitic manganese steels.

It is proposed by Jack (1974) that the orientation relationships between carbides and the matrix in steels could be considered in terms of a simple correspondence between the metal atoms that coordinate the interstitial atoms in the carbide and the octahedron of metal atoms that surround the carbon in the parent phase. Both the Pitsch and the Bagaryatski relations can be derived from this consideration and, furthermore, a combination of the ferrite-cementite and cementite-austenite relationships is consistent with the well established Kurdjumov-Sachs orientation between ferrite and austenite.

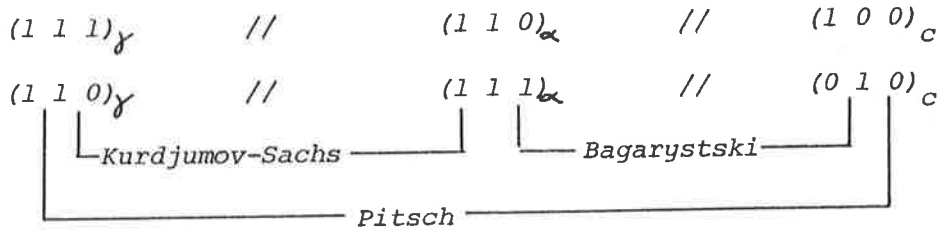

Indeed, Darken et al. (1962) have suggested these orientations between the pearlite constituents and the prior austenite in plain carbon steels although they were unable to determine a complete crystallographic analyses of all phases due to the transformation of the remaining austenite to martensite on quenching to room temperature.

This problem was overcome by utilizing the unique properties of austenitic manganese steel. Since the Ms is depressed to subzero temperatures (Section 2.2) the remaining austenite coexists with pearlite after partial transformation. Dippenaar et al. (1973) succeeded in obtaining a full crystallographic description of the pearlite phase and the adjacent austenite in the alloy Fe-11.9Mn-0.79C. In essence it was shown that the pearlite constituents of colonies that nucleated on grain boundary proeutectoid cementite displayed the Bagaryatski relationship whereas those pearlite colonies that nucleated on 'clean' austenite grain boundaries exhibited the Pitsch-Petch relation. In both cases the pearlitic cementite was found to be related by the Pitsch relationship to the adjacent austenite grain (γ_2) in which it was not growing. In addition, the pearlitic ferrite, in the case where colonies nucleated on clean austenite grain boundaries, was found to display the Kurdjumov-Sachs relationship with (γ_2).

It can be concluded from that work that the ferrite which forms at the grain boundary between two austenite grains is in direct contact with γ_1 and, moreover, has a low energy interface with γ_2 defined by the Kurdjumov-Sachs relationship. Conversely, the random orientation between the ferrite and the austenite grain (γ_1) in which nodule growth occurs results in a high energy interface of high mobility. Similarly, the pearlitic cementite also has a high energy mobile interface with γ_1. The overall effect of pearlite growth is the migration of the original γ_1/γ_2 grain boundary interface into the γ_1 austenite grain and the process may be defined as a discontinuous precipitation reaction (Hornbogen 1972).

Thus the major contribution of the above work to the study of the pearlite nucleation and growth processes in steels was to show that there existed an orientation relationship between one or both of the pearlite constituents and the adjacent austenite grain (γ_2) in which it was not growing. However, some of the conclusions are inconsistent with the suggestions and observations of other workers. Firstly, it was shown that pearlite colonies displaying the Bagaryatski orientation relationship invariably nucleated on pre-existing grain boundary cementite. The pearlitic cementite was shown by dark field electron microscopy to have the same orientation as the proeutectoid cementite which in turn was related to the adjacent austenite grain (γ_2) by the Pitsch relation. But the pearlitic ferrite was stated to be randomly orientated with respect to γ_2, contrary to the suggestions of Darken et al (1969) and Jack (1974) who showed that the Kurdjumov-Sachs relationship must exist between the ferrite and austenite phases under these conditions.

Secondly, Dippenaar et al. predicted, on the basis of their experimental results, that the Bagaryatski orientation relationship would predominate in pearlite colonies in a more hyper-eutectoid steel since the formation of proeutectoid grain boundary cementite is enhanced (Section 2.4). However, Shackleton et al. (1969) showed that only one of eleven pearlite nodules examined in the alloy system Fe-12.8Mn-1.15C displayed the Bagaryatski relation and the remaining ten colonies exhibited the Pitsch-Petch relation.

A number of factors may contribute to these discrepencies. It has been observed by the author of the present work that pearlite nodules in these steels are not simple duplex structures but consist of multiple subgrains that display different variants of the orientation relationships. In addition, the interlamellar spacing within each subgrain, which are only several 1000nm in diameter, are of the order of 100-500nm (Honeycombe 1976). Under these conditions extreme care must be exercised in order to obtain a true representation of the various orientations by electron diffraction techniques. It is shown later that the utilization of Kikuchi patterns, which are readily available in the austenite phase, greatly simplifies the orientation determinations.

2.6 Modifications of Austenitic Manganese Steel

The loss of toughness and the inability to form an effective work hardened surface layer after reheating is a severe restriction on the practical applications of high manganese steels. The maximum working temperature is limited to 260^{o}C (Avery 1961), and repair or resurfacing operations using welding techniques must be approached with caution. In

addition, heavy section castings made from high carbon grades of austenitic manganese steels are prone to cracking in the foundry during slow cooling from the melt because of carbide precipitation. Although a reduction in the carbon content from 1.2% to 0.8% will reduce the tendency to cause embrittlement there is also a substantial decrease in the work hardening potential of the matrix (White et al. 1962).

A second modification to the composition of Hadfield steel is the alloy Fe-6Mn-1.2C which has been found to offer a higher resistance to gouging and grinding abrasion but possesses only moderate toughness, (Norman et al. 1960). It can be seen with reference to Fig. 2.1 that these properties are the result of partial transformation to α martensite on subsequent cold working. Another drawback with this lower manganese steel is that it is even more susceptible to carbide precipitation on reheating than conventional Hadfield steel.

A third variation in the microstructure of austenitic manganese steels that has received some attention in the literature is a process described as 'dispersion hardening' (Maratray et al. 1961, Hall 1966). Nominal Hadfield steel is solution treated, followed by isothermal ageing to produce partial transformation to pearlite, then upquenched to approximately 900^{o}C to spherodise the carbide lamellae and finally water quenched. The resultant microstructure consists of a refined grain size and an uneven distribution of undissolved carbide which is generally located in the vicinity of grain boundaries. The affect is a moderate increase in yield strength and initial hardness which slightly reduces the undersirable plastic flow that occurs in service.

However, the presence of undissolved carbide not only lowers the ductility of the steel but also its work hardening capacity due to the removal of carbon from solution. Since control of the carbide dispersion is also limited by the inherent segregation of cast austenitic manganese steels (Sedriks et al. 1964), and the critical requirements of the heat treatment procedure in the upquenching stage, the process is not recommended.

Thus the modification of Hadfield steel by varying the carbon/ manganese ratio or the conventional heat treatment procedure causes a decrease in the characteristic toughness and/or work hardening potential with a resultant restriction in its general applications.

The additions of strong carbide forming elements to high manganese steels, in particular chromium and molybdenum up to 2 weight per cent, is an established practise (Maratray 1964, Middleham 1964, Avery 1961). In the solution treated condition these additions cause a slight increase in the initial hardness of the austenite and marginally improve both the yield point and the tensile strength due to solid solution hardening. Thus excessive dimensional changes of austenitic manganese steels that occur in service as a result of plastic flow prior to work hardening are reduced. Both chromium and molybdenum bearing manganese steels are reported to display a greater wear resistance than the basic Hadfield steel in some applications (Hall 1966).

Rao et al. (1963) examined the influence of a number of carbide formers (Cr, Mo, W, V, Ti) on the transformation characteristics of austenitic manganese steels. Their results were inconclusive since the wide variation in the solid solubility of these carbides in austenite was not considered. All steels. irrespective of the kind and quantity of carbide former added, were solution treated at 1100^{o}C producing microstructures consisting of undissolved alloy carbides in austenite. The formation of these carbides effectively removed varying amounts of carbon from the austenite matrix. Since it has been shown earlier that the transformation characteristics of austenitic manganese steels are greatly influenced by the carbon content (Section 2.4) no quantitative results can be obtained from this work.

Maratray et al. (1961) have reported that 2%Mo completely dissolved in austenitic manganese steel eliminates the formation of Widmanstatten cementite on isothermal ageing and increases the incubation period for the onset of the pearlite reaction. It will be shown in later chapters of the present work that the addition of molybdenum has a more fundamental influence on the transformation characteristics of austenitic manganese steels in so far as the decomposition products are concerned. The crystal structure of the proeutectoid carbide and the pearlitic carbide will be shown to be the complex cubic carbide $M_{23}C_6$. It will also be shown that at higher ageing temperatures ($>600^{o}$C) two further transformation reactions occur; discontinuous precipitation of grain boundary nucleated nodules composed of $M_{23}C_6$ + austenite and precipitation of Mo_2C in austenite causing substantial hardening of the matrix.

Precipitation hardening of austenitic manganese steels containing other strong carbide forming elements have been reported in the literature. The alloy Fe-14Mn-4Cr-0.8C age hardens in the temperature range 650°-900°C (with a maximum hardness of 375Hv) due to matrix precipitation of the alloy carbide $M_{23}C_6$ (Saito 1972). Decomposition of the austenite to grain boundary carbide and pearlite was also observed at lower ageing temperatures but not reported in any detail. The addition of 0.55V to this alloy increases the age hardening response to 440Hv due to the precipitation of VC in the austenite.

Imai et al. (1970) reported a greater age hardening response in the more complex alloy system Fe-17Mn-12Cr-2.4V-2.2Ni-0.44C . Peak hardness is attributed to precipitation of extremely fine coherent particles in the matrix and overageing coincides with loss of coherency when the particles size exceeds 16nm in diameter.

Age hardening of the alloy Fe-25Mn-5Cr-5Ni-1Nb-0.1C due to precipitation of NbC on dislocations at 800°C and on stacking faults over a range of temperatures below 700°C has also been reported (Chaturvedi et al. 1968).

Although the compositions of the above alloys are complex and deviate by varying amounts from the basic Hadfield system, they illustrate the propensity of austenitic manganese steels to age harden by the precipitation of a number of different alloy carbides. The additions of chromium and nickel have been included in these alloys to increase the stability of the austenite phase. However, the same result can also be achieved by simply increasing the carbon content of high manganese steels (Fig. 2.1) and the complicating effect of the precipitation of chromium carbide, which can occur in these systems (Saito 1972) is eliminated. Thus, in the present

work,, more meaningful and fundamental information may be obtained by considering the addition of a single carbide forming element to maximum supersaturation in a host alloy close to the basic Hadfield composition. A discussion of a recent investigation of the alloy Fe-13Mn-2V-0.8C (Ainsley 1979) which satisfies these criteria is outlined below.

The maximum solid solubility of vanadium in Fe-13Mn-0.8C is 2% at 1300^{o}C which is about 20-30^{o}C below the solidus temperature. Precipitation of VC, under equilibrium conditions at the isothermal ageing temperature (600^{o}C) removes approximately 0.45%C from solution reducing the composition of the remaining austenite to Fe-13Mn-0.35C. Thus, from Fig. 2.1, VC precipitates coexist with stable austenite on subsequent cooling to room temperature in this alloy system.

Three quite distinct transformation reactions, observed over the ageing temperature interval 400-900^{o}C, are summarized in Table 2.1.

Table 2.1

TRANSFORMATION REACTION	TEMPERATURE RANGE (^{o}C)
General Matrix Precipitation	400-900
Pearlite, $(Fe,Mn)_3C + \alpha$	400-550
Discontinuous Precipitation — fine	550-710
Discontinuous Precipitation — coarse	640-900

The first reaction, general matrix precipitation, is identical with that observed by Imai (1970) discussed elsewhere. An extremely fine dispersion of semi-coherent VC particles form homogeneously throughout the matrix and

results in a very substantial age hardening effect (550Hv).

The second reaction, decomposition of austenite to $(Fe,Mn)_3C + \alpha$ is similar to that occurring in Fe-Mn-C alloys. In addition, VC precipitates, also observed within the ferrite lamellae, are considered to have developed in contact with the advancing α/γ boundary.

In the third reaction supersaturated austenite (γ_1) decomposes in a discontinuous manner at grain boundaries to yield a dispersion of VC precipitates in solute depleted austenite (γ_2). At the higher ageing temperature range coarse lamallae VC forms and is easily resolved in the optical microscope. At lower temperatures the morphology of the VC precipitates, revealed by electron microscopy, consists of long thin fibres and small discrete particles. The results of crystallographic studies of this transformation reaction have been previously discussed in Chapter 1. Although the fine d.p. reaction occurs over the temperature interval 550-710°C it only proceeds to completion below 640°C. Above this temperature general matrix precipitation ahead of the advancing colonies prevents complete transformation from taking place. In fact, termination of the d.p. reaction coincides with peak hardness of the untransformed austenite (γ_1).

Although the hardness of the structure after complete transformation to the fine d. p. reaction product is about 550Hv the work hardening capacity is expected to be much lower than Hadfield steel because of the reduced carbon content (0.35%C) of the austenite phase. In addition there is a marked reduction in tensile properties. The very low ductility of this alloy (1% elongation compared with 65% for Hadfield steel) causes premature fracture during tensile loading.

It would seem to the author of the present work, however, that the utilization of the general matrix precipitation product that forms readily at higher ageing temperatures may be of some practical significance. If the carbon content of the solute depleted austenite can be increased by carburization during the isothermal ageing process, a steel of essentially Hadfield composition containing a dispersion of extremely fine precipitates may be realised. Thus, an alloy with the characteristic toughness and work hardening potential of convenional austentic manganese steel coupled with a high initial hardness and improved yield strength is envizaged.

CHAPTER 3

3. ISOTHERMAL TRANSFORMATION OF Fe-Mn-Mo-C ALLOYS

3.1 General Observations and Preliminary Investigations

3.1.1 Solubility of Molybdenum in Austenitic Manganese Steels

Although it is known that approximately 8% Mo will dissolve in austenitic Fe-C alloys the solubility limit of molybdenum in austenitic manganese steels has not been reported in the literature. Manganese tends to increase the solubility of carbide forming elements in austenite (Freeman 1971) while carbon has an opposing effect and also substantially lowers the solidus temperature. The partial phase diagram of the relevant portion of the quarternary system Fe-Mn-Mo-C was determined by metallographic techniques (Appendix A1) and the resultant solvus and solidus temperatures as a function of molybdenum content for Fe-13Mn-0.8C and Fe-13Mn-1.2C steels are shown in Fig. 3.1.

3.1.2 Isothermal Transformation Reactions

A number of austenitic manganese steels containing up to 8% Mo with a systematic variation in manganese, molybdenum and carbon content were isothermally aged in the temperature range 300-900^{o}C. A total of five distinct transformation reactions which were restricted to fixed ageing temperature limits were observed, Table 3.1a. However, the presence and the extent of transformation of these various reactions were found to depend on alloy composition. A summary of the reactions observed in the range of alloys investigated after isothermal ageing for a maximum of 250 hours in the range 300-900^{o}C is outlined in Table 3.1b.

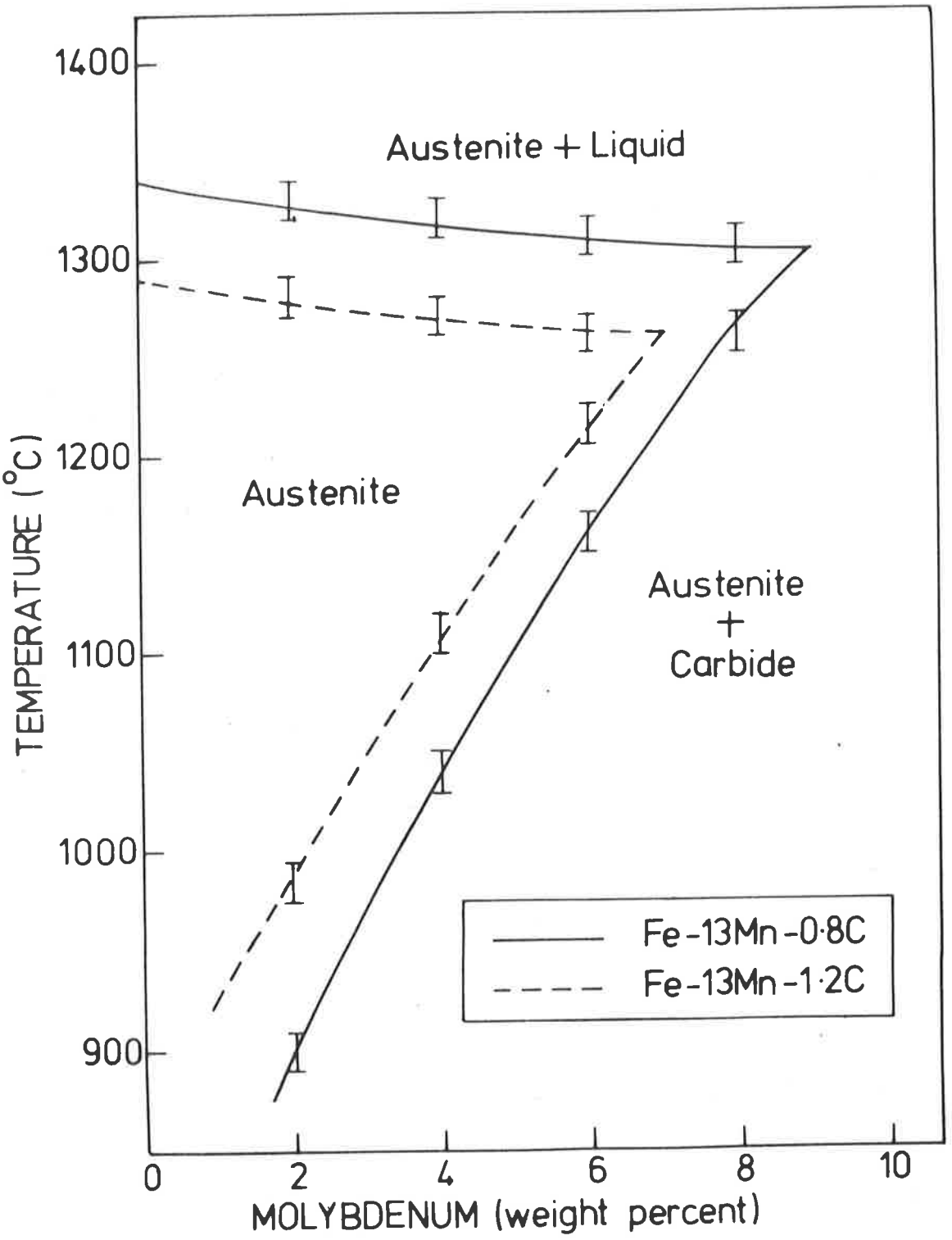

Fig. 3.1 Solubility of Molybdenum in Fe-13Mn-1.2C and Fe-13Mn-0.8C.

TABLE 3.1a

TRANSFORMATION PRODUCT	TEMPERATURE RANGE (^{o}C)
Widmanstatten Cementite $(Fe,Mn)_3C$	350 - 550
Grain Boundary and Intragranular $M_{23}C_6$	450 - 625
Lamellar $M_{23}C_6$ + Ferrite	475 - 625
Lamellar $M_{23}C_6$ + Austenite	650 - 850
Particulate and fibrous Mo_2C	600 - 900

TABLE 3.1b

ALLOY COMPOSITION	WIDMAN-STATTEN CEMENTITE	G.B. AND INTRAGRANULAR CARBIDE	PEARLITE	$M_{23}C_6$ + AUSTENITE	Mo_2C
Fe-13Mn-0.4C					
Fe-13Mn-0.8C			X(42)*		
" -2Mo			X(25)		X(310)**
" -4Mo			X(12)		X(510)
" -6Mo					X(550)
" -7Mo					X(590)
" -8Mo					X(605)
" -10Mo					X(625)
Fe-13Mn-1.2C	X	X	X(85)		
" -2Mo	X	X	X(50)	X(5)*	X(321)
" -4Mo	X	X	X(45)	X(20)	X(480)
Fe-13Mn-1.6C	X	X	X(80)		
" -2Mo	X	X	X(42)		X(319)
" -4Mo	X	X	X(35)	X(5)	X(473)
Fe-8Mn-0.8C			X(87)		
" -1Mo			X(76)	n.d.	n.d.
" -2Mo			X(75)	n.d.	n.d.
Fe-8Mn-1.2C	X	X	X(100)		
" -1Mo	X	X	X(86)	n.d.	n.d.
" -2Mo	X	X	X(78)	n.d.	n.d.

TABLE 3.1 Transformation reactions in Fe-Mn-Mo-C alloys
(a) Temperature Range
(b) Composition Range.

(X) Transformation reaction observed.
(n.d.) Not determined
* Maximum volume fraction achieved within 250 hours
** Maximum hardness (HV_{10}) achieved within 250 hours.

The alloy Fe-13Mn-4Mo-1.2C was selected for detailed examination since it exhibited all the transformation reactions observed in this alloy system. The isothermal transformation diagram, Fig. 3.2a, was constructed by determining the onset on the precipitation reactions using metallographic techniques. None of the reactions went to completion in the maximum ageing time (250 hours) used in this study. The precipitation of Mo_2C in austenite could not be included in the transformation diagram because of the heterogeneous nature of the reaction. The age hardening characteristics of the matrix due to the precipitation of Mo_2C in austenite were determined over the range 600°C to 850°C and are shown in Fig. 3.2b. The curves illustrated the classical behaviour of an age hardening material. Maximum peak hardness occurred at a lower ageing temperature whereas the hardening rate increased at higher temperatures. However, over-ageing in the alloy was very slight resulting in a decrease in hardness of about 20 Vickers after prolonged ageing at 650°C.

The microstructures of the five transformation products observed in this alloy system are illustrated in the optical micrographs in Fig. 3.3. The individual reaction products were studied by selecting different alloy compositions that presented optimum conditions for the precipitation of each transformation mode. The Widmanstatten cementite, grain boundary carbide and pearlite reactions are briefly examined in the following sections while the two elevated temperature reactions, matrix and discontinuous precipitation and their mutual interaction, are investigated in detail in a later chapter.

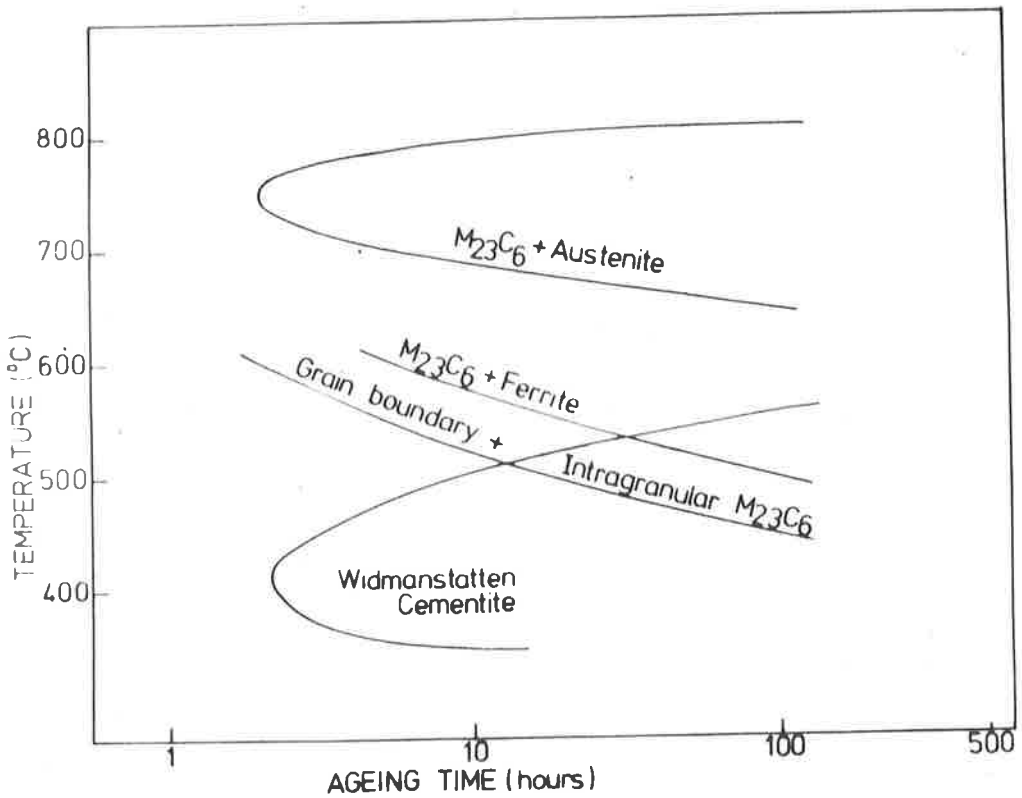

Fig. 3.2a. Isothermal transformation diagram for Fe-13Mn-4Mo-1.2C.

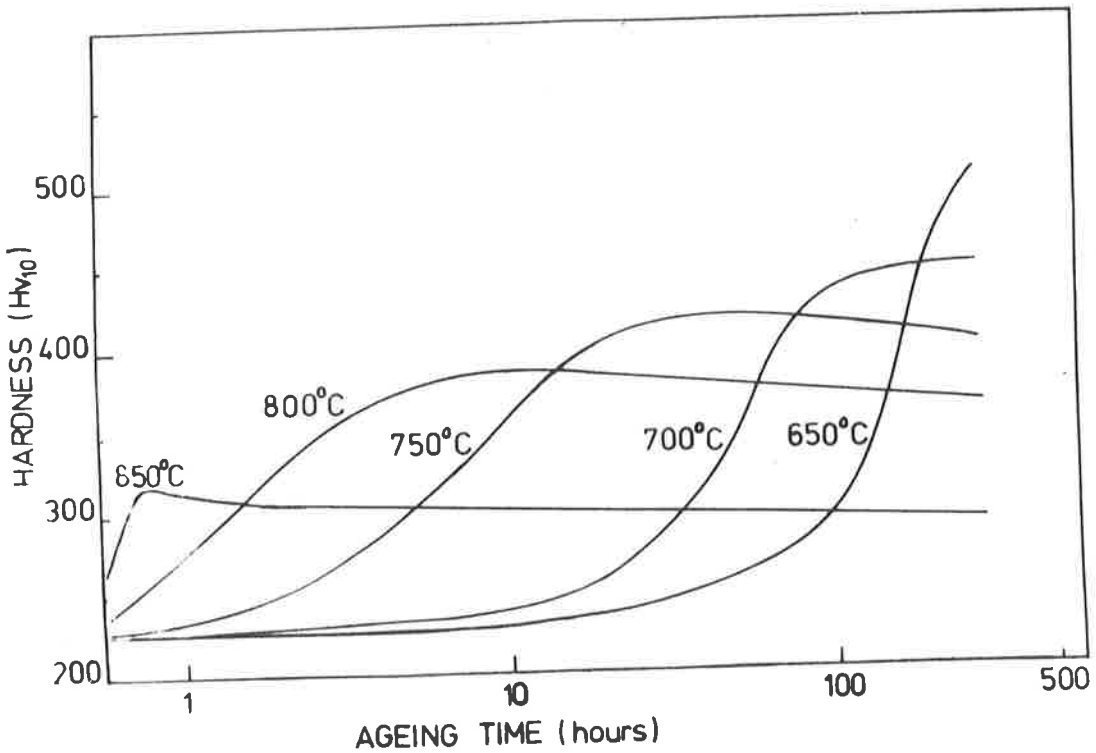

Fig. 3.2b. Age hardening characteristics of Fe-13Mn-4Mo-1.2C.

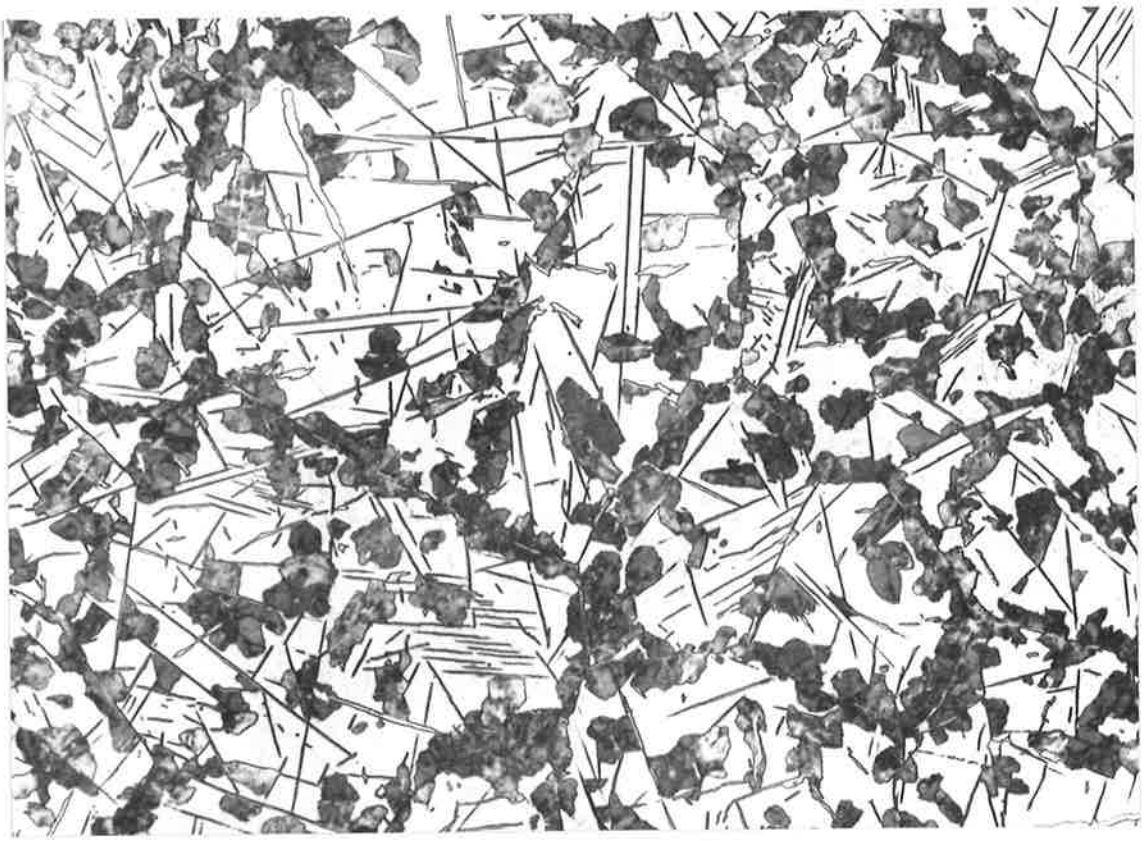

Fig. 3.3a. Fe-13Mo-4Mo-1.2C aged at 500°C for 100 hours.

Optical micrograph x 350

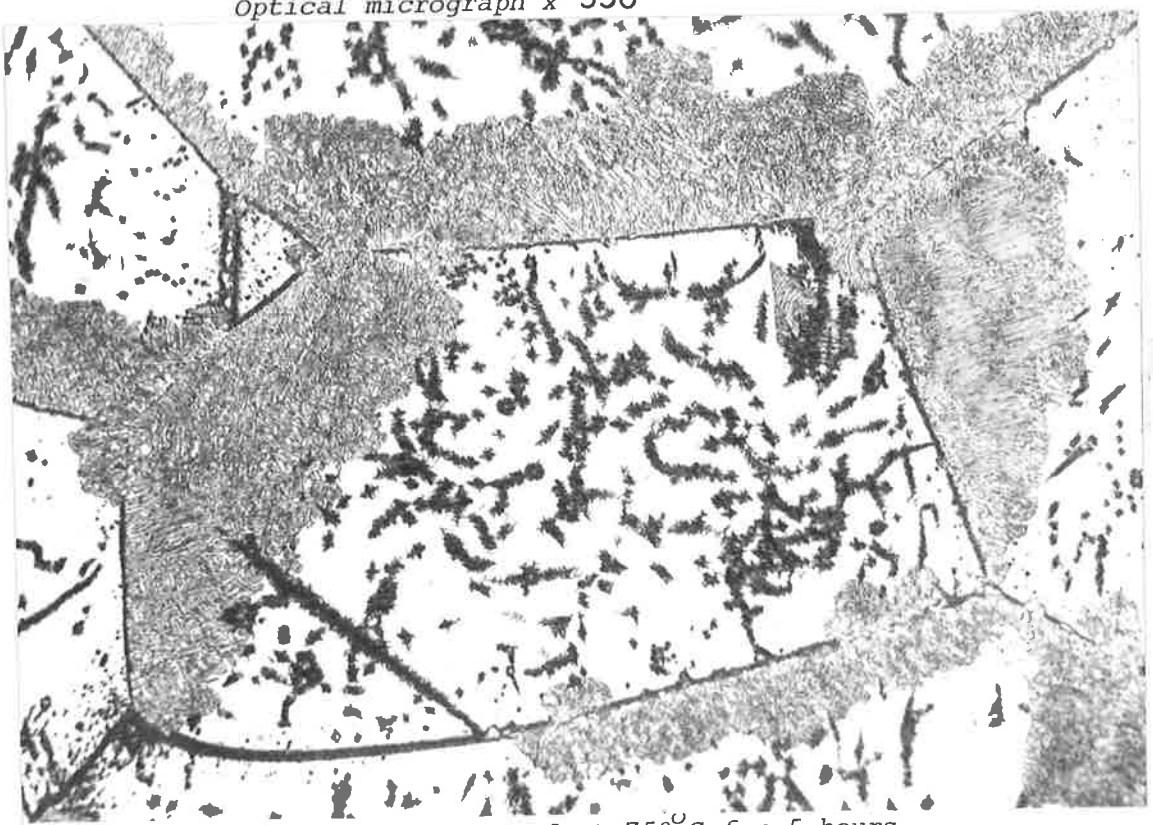

Fig. 3.3b. Fe-13Mn-4Mo-1.2C aged at 750°C for 5 hours.

*Optical micrograph x*350

3.2 Widmanstatten Cementite

3.2.1 The microstructure of the proeutectoid carbide observed in the transformation range 350°C to 550°C consisted of approximately parallel arrays of Widmanstatten plates within each grain (Fig. 3.4a). Close inspection showed that these plates were often not continuous and some degree of discontinuity and branching was observed in electron microscopy. A bright field electron micrograph with the austenite in two beam conditions for the desired contrast (Fig. 3.4b) showed the presence of dislocations and stacking faults in the matrix. Although dislocations in the austenite were always associated with the transformation product in agreement with Dippenaar (1970), stacking faults were only evident when a number of plates formed in close proximity.

The plates were identified as cementite by selected area electron diffraction (SAD) using the austenite phase, whose lattice parameter had been determined by X-ray diffraction, as a built in calibration. The inherent ambiguity of indexing spot patterns from the cementite structure was resolved by obtaining at least two zone axes over a measured tilt angle using Kikuchi patterns from the adjacent austenite to accurately measure the tilt angle.

3.2.2 Crystallographic Investigation

The crystallography of a similar Widmanstatten product in basic austenitic manganese steel had previously been determined by Pitsch (1963) and Dippenaar (1970) and found to be within the orientation range predicted by Sleeswyk (1966) and Jack (1974). In these works the empircally determined orientation relationships, obtained by electron diffraction techniques with estimated experimental errors of

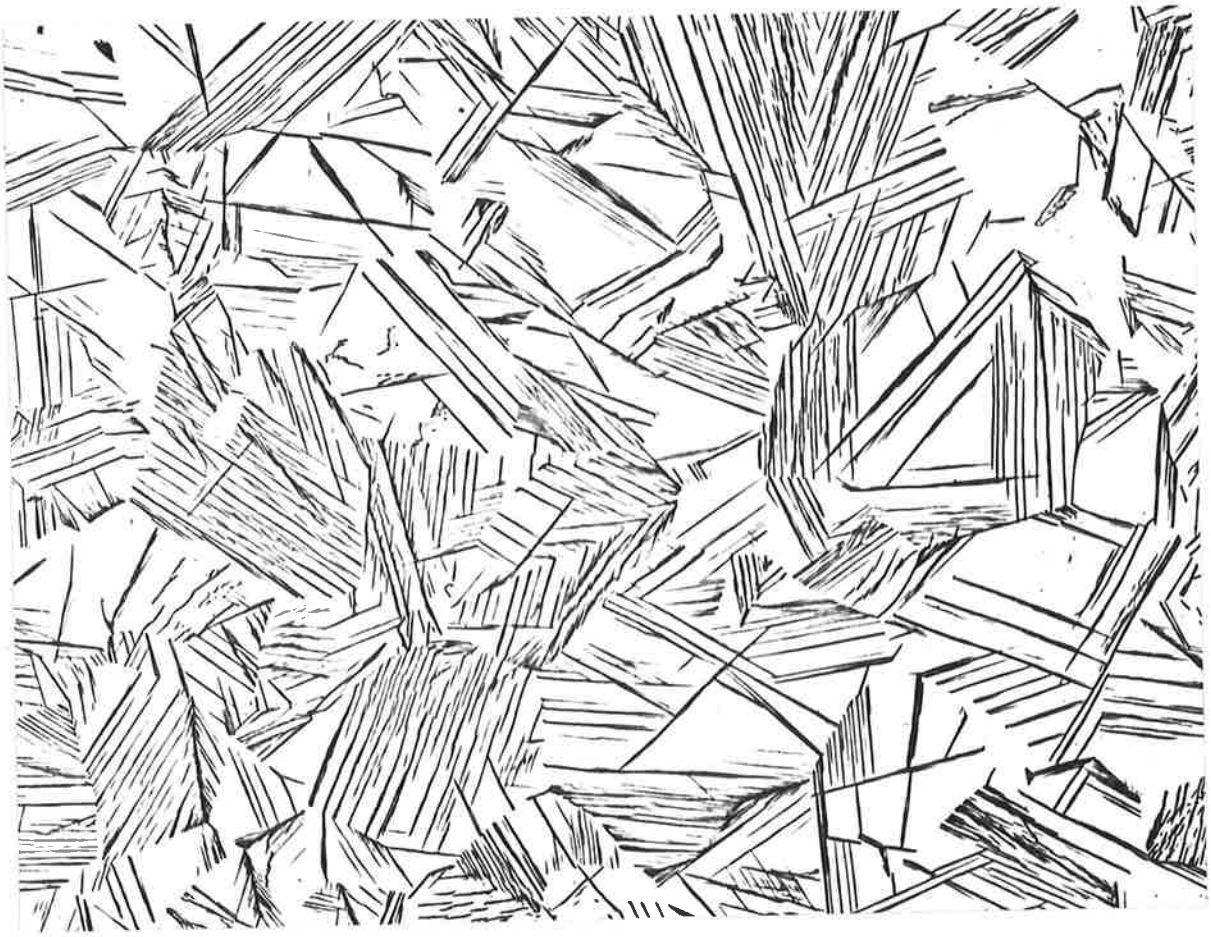

Fig. 3.4a. Fe-13Mn-4Mo-1.2C aged at 450°C for 50 hours.
Optical micrograph x 350

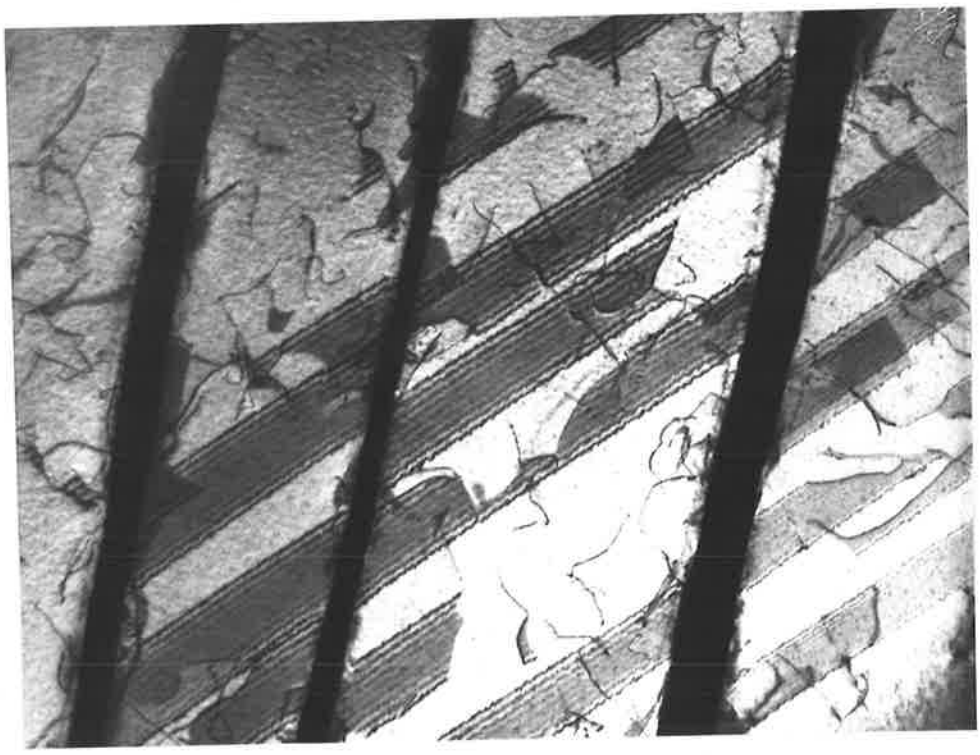

Fig. 3.4b. Fe-13Mn-4Mo-1.2C aged at 450°C for 50 hours.
Thin foil electron micrograph x 23,000

$\pm 2^{o}$ were found to be scattered over a rather large angular range of about $\pm 10^{o}$. An inspection of the published diffraction patterns showed that the orientations were obtained from the analyses of superimposed spot patterns of cementite and austenite exhibiting a single zone axis of each phase. Experience by the author of the present work had indicated that this condition was extremely difficult to achieve since the orientations were not a simple relationship and occurred over an angular range. Furthermore, it was observed that higher order Laue zones from the carbide phase readily formed in electron diffraction, (Hirsch et al. 1965), and in many instances bands of these zones which were $\pm 5^{o}$ or more from the actual zone axis could be mistaken for the zero order Laue zone at large camera constants.

This difficulty was overcome by developing a technique requiring a separate diffraction pattern from each phase at two tilt conditions (Appendix A3.2). A typical set of SAD patterns of cementite and the adjacent austenite is shown in Fig. 3.5. Since the use of graphical methods, e.g. the stereographic projection, introduce experimental errors of about $\pm 2^{o}$ (Johari and Thomas (1970)), matrices, constructed from the diffraction data, were used to complete the analysis (Appendix A3.2). The orientation relationship between cementite and austenite was found to be:

$$[001]_{c} \;//\; [\overline{2.00} \quad 2.10 \quad 4.97]\ \gamma$$

$$[010]_{c} \;//\; [1.00 \quad 1.08 \quad \overline{0.06}]\ \gamma$$

$$[100]_{c} \;//\; [5.04 \quad \overline{4.45} \quad 4.00]\ \gamma$$

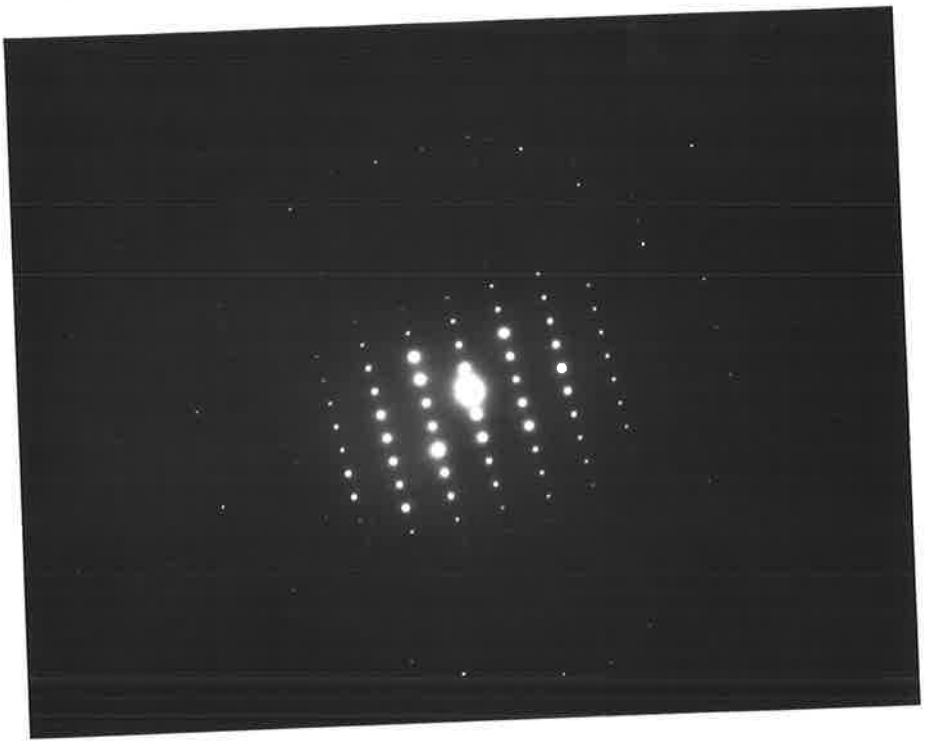

Fig. 3.5a. [201] *zone axis of cementite exhibiting a concentric first order Laue zone.*

Fig. 3.5b. [31 $\overline{24}$ 92] *Kikuchi pole of the adjacent austenite.*

which is within 3.5^{o} of the Pitsch relationship:-

$[001]_C$ // $[\bar{2}\ 2\ 5]$ Y

$[010]_C$ // $[1\ 1\ 0]$ Y

$[100]_C$ // $[5\ \bar{5}\ 4]$ Y

Orientation relationships determined from three further sets of diffraction data were all found to be within 5^{o} of the Pitsch relationship.

3.3 Grain Boundary and Intragranular Carbide

3.3.1 Microstructural Investigation

Grain boundary and intragranular carbides preceded the formation of pearlite on ageing the alloy Fe-13Mn-4Mo-1.2C in the temperature range 450°C to 625°C. A thin film of carbide, similar to the proeutectoid cementite observed in the basic Fe-13Mn-1.2C steel, formed on the austenite grain boundaries (Fig. 3.3b). Examination by thin foil electron micrscopy showed that the carbide film was continuous along the grain boundary and growth occurred into one of the adjacent austenite grains (Fig. 3.6a). Extensive faulting of the carbide film is also evident in this micrograph.

3.3.2 Crystallographic Investigation

The crystallography of the grain boundary carbide was determined by thin foil electron microscopy techniques. A superimposed SAD pattern of the carbide and austenite (Y_2) is shown in Fig. 3.6b. The analysis of this diffraction pattern showed the following results:-

(a) The carbide structure was isomorphous with the austenite (f.c.c.) and a cube-cube orientation relationship;

$$[uvw]\ C \quad // \quad [uvw]\ Y$$

$$(hkl)\ C \quad // \quad (hkl)\ Y$$

was confirmed from a number of diffraction patterns at various tilts.

(b) The carbide was identified as $M_{23}C_6$ from the measured lattice parameters using the lattice parameter of the austenite as a calibration standard. Andrews et al. (1968) have stressed the difficulty of interpretating SAD patterns of $M_{23}C_6$ and M_6C in ferrite since they are isomorphous and have nearly

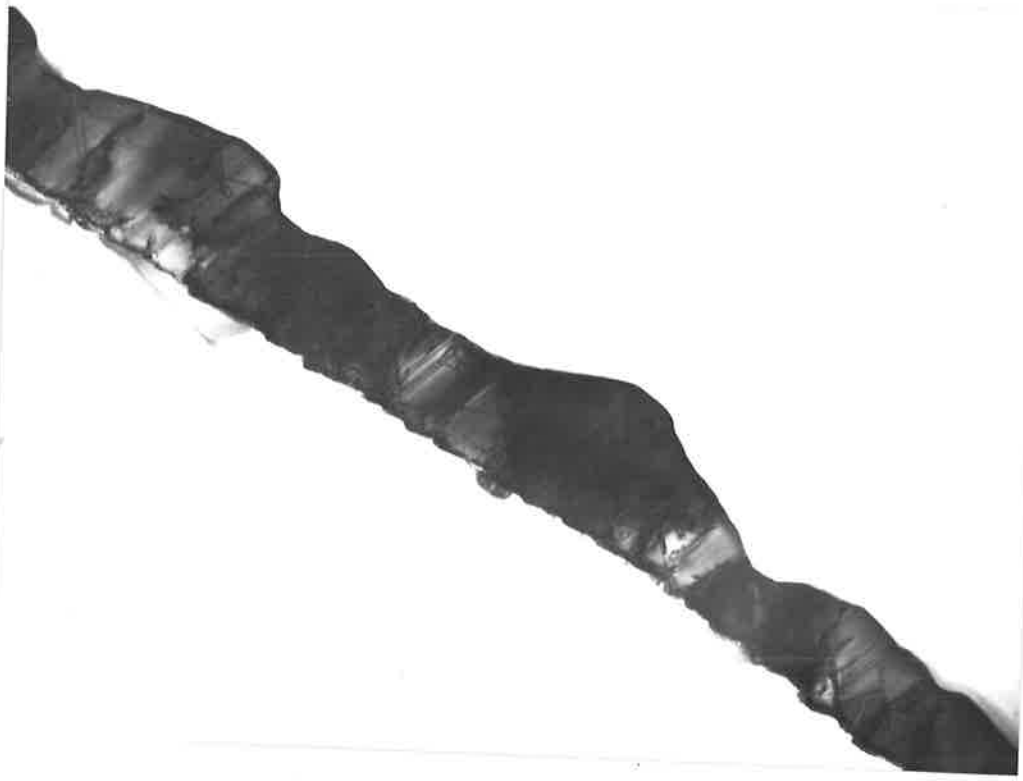

Fig. 3.6a. Fe-13Mn-4Mo-1.2C aged at 600°C for 5 hours. Thin foil electron micrograph x 13,500

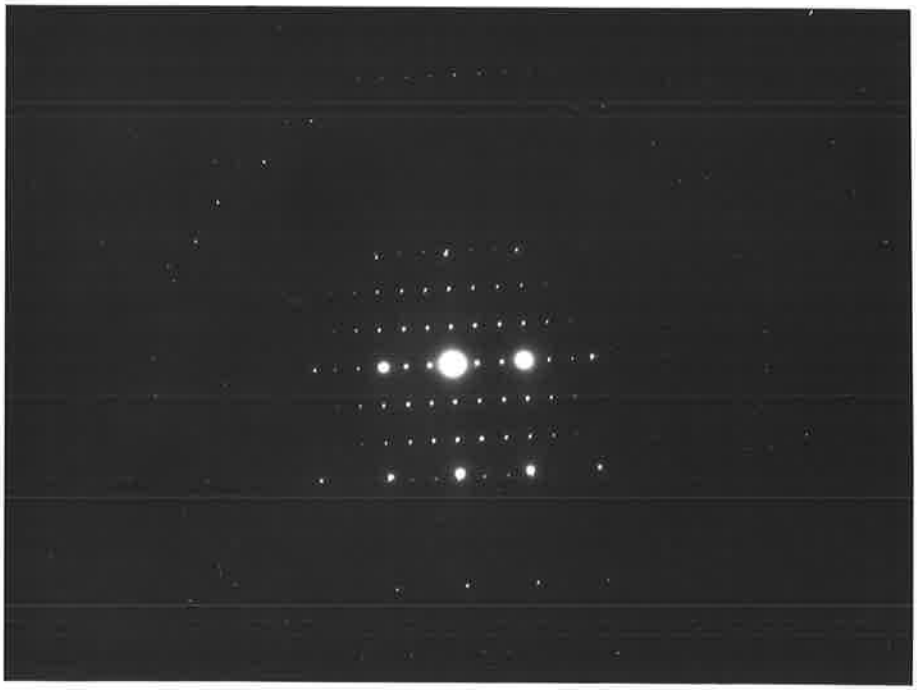

Fig. 3.6b. Superimposed [$\bar{1}12$] zone axes of austenite γ_2 and $M_{23}C_6$ in fig. 3.6a.

the same lattice parameters; 1.062 nm and 1.108 nm respectively. However, differentiation between these structures precipitating in austenite in the current work was simplified because of the cube-cube orientation relationship and by the fact that the lattice parameter of $M_{23}C_6$ is just less than 3 times the lattice parameter of the austenite (0.364 nm) whereas the lattice parameter of M_6C is just greater than 3 times that of austenite. Inspection of the relative positions of the carbide and austenite diffraction spots was sufficient to identify the precipitating carbide.

3.4 Pearlite

3.4.1 Effect of Alloy Composition

Extensive decomposition of austenite to pearlite occurred during isothermal ageing over a wide composition range in the Fe-Mn-Mo-C system. The effects of alloy composition on the pearlite reaction, indicated in Table 3.1b, are summarized below:

(a) Manganese

It was found that a reduction of the basic austenitic manganese steel (Fe-13Mn-1.2C) to 8% Mn not only accelerated the decomposition reaction but also resulted in 100% transformation to pearlite.

(b) Carbon

A reduction in carbon content from the basic steel to Fe-13Mn-0.8C decreased the decomposition rate and the final volume fraction of pearlite formed. No pearlite was observed in Fe-13Mn-0.4C after prolonged ageing over a wide temperature range.

(c) Molybdenum

An increase in molybdenum content was found to retard the pearlite reaction in agreement with the observed effects of the additions of other strong carbide forming elements in the transformation behaviour of austenitic manganese steels (Ainsley et al. 1979), Imai et al (1970). Indeed, in alloys containing more than 4% Mo it was found that the pearlite reaction was completely suppressed.

3.4.2 Microstructural Investigation

Pearlite nucleated at a variety of heterogeneous sites; on 'clean' austenite grain boundaries, grain boundary carbide films, intragranular carbides and on Widmanstatten cementite plates. Transformation proceeded by the discontinuous growth of pearlite colonies in the austenite matrix. Investigations of pearlite nodules

in the alloy Fe-13Mn-4Mo-1.2C showed that individual pearlite colonies consisted of numerous subgrains about 5,000 nm in diameter with interlamellar spacings in the order of 100 nm (Fig. 3.7a). Dark field electron microscopy studies indicated that there was a change in the orientation of both the carbide and ferrite phases across the subgrain boundries. Instability of the austenite adjacent to the advancing interface of the pearlite colonies was observed after prolonged ageing (Fig. 3.7b). Extensive stacking fault formation, indicative of the $\gamma \rightarrow \varepsilon$ martensite transformation reported in austenitic manganese steels containing a low carbon content (Remy 1974) is evident.

3.4.3 Crystallographic Investigation

A typical electron diffraction pattern of a pearlite subgrain is shown in Fig. 3.8a. A low index zone axis of the carbide phase was obtained by tilting until a uniformly spatial zero order Laue zone was observed. Minor tilting adjustments, producing a concentric ring of higher order Laue zones around the central spot, permitted an orientation estimated within $\pm$ 0.5^{o} of the calculated zone axis. Analysis of the carbide spot pattern showed the following:-

(a) The carbide was a face centered cubic structure with lattice parameter a = 1.062 nm. This interpretation was confirmed by several other diffraction patterns and the structure was identified as $M_{23}C_6$.

(b) The determined zone axis was $[\bar{1}\ 1\ 2]$.

An irrational zone axis of the ferrite, evident by the non uniform distribution of diffraction spots around the central beam, showed that the orientation of this phase was close to $[\bar{1}\ 5\ 7]$ in

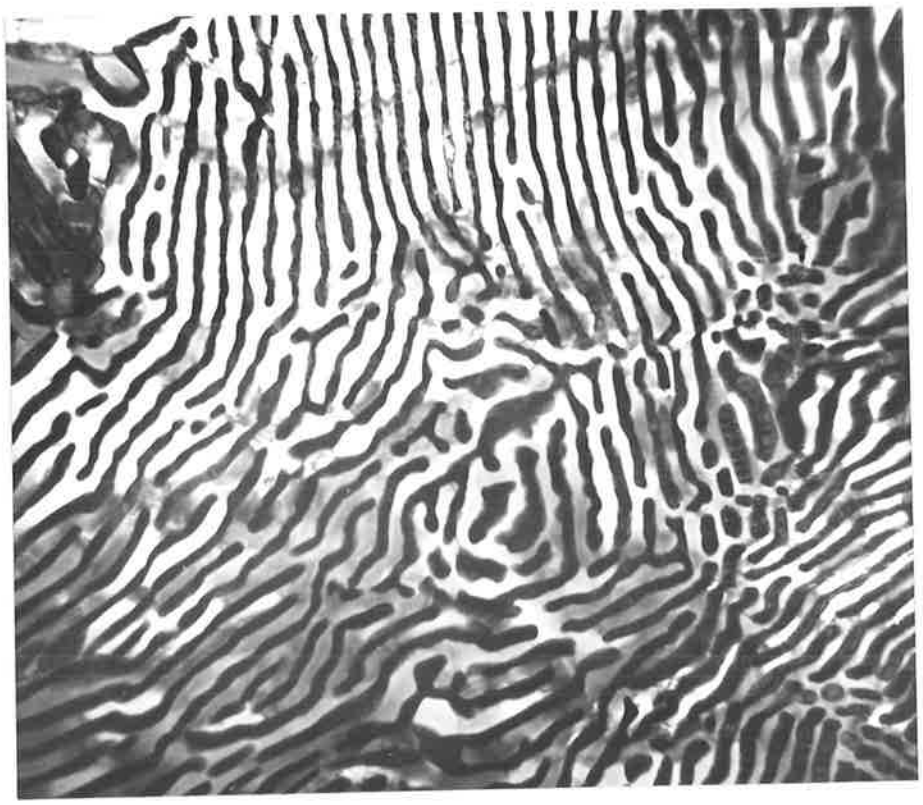

Fig. 3.7a. Fe-13Mn-4Mo-1.2C aged at 600°C for 25 hours. Thin foil electron micrograph x19,000

Fig. 3.7b. Fe-13Mn-4Mo-1.2C aged at 600°C for 100 hours. Thin foil electron micrograph x45,000

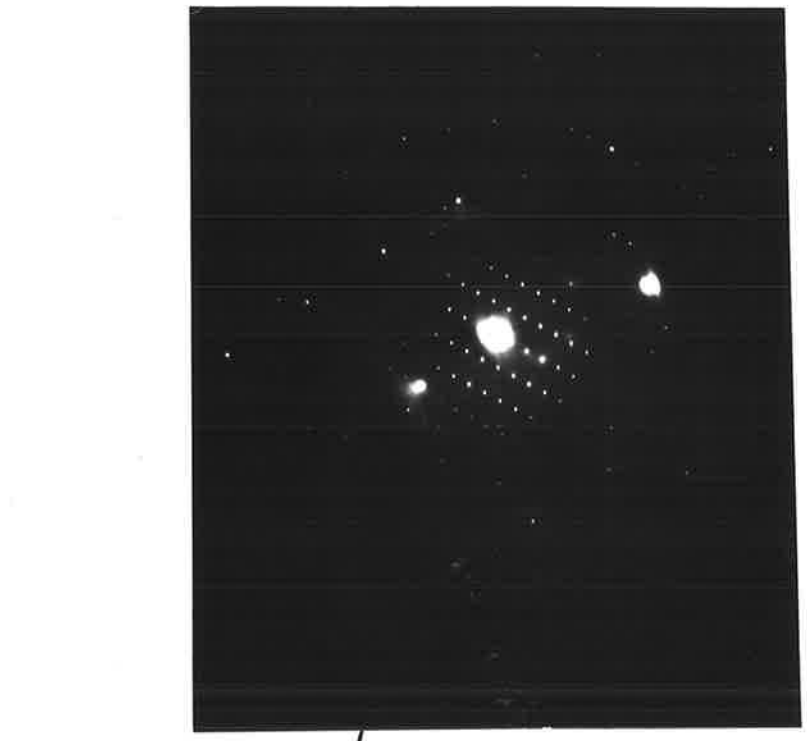

(a)

Composite Diffraction pattern of $M_{23}C_6$ and Ferrite.

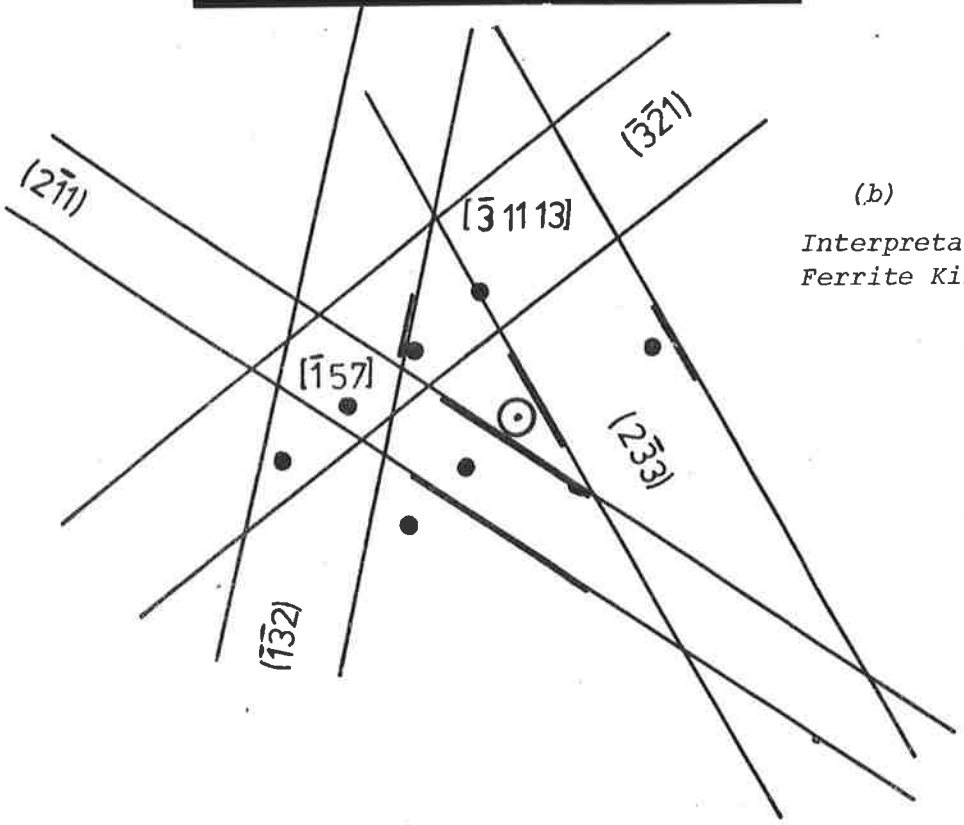

(b)

Interpretation of Ferrite Kikuchi pattern.

Fig. 3.8. Electron diffraction pattern of alloy pearlite.

$[\bar{1}\ \ 1\ \ 2]_{M_{23}C_6}$ // $[\bar{1}\ \ 6.44\ \ 7.75]$ ferrite.

the standard stereographic triangle bounded by the poles $[001]$ - $[011]$ - $[\bar{1}11]$. The anaylses of a number of patterns had indicated that the Kurdjumov-Sachs orientation relationship between the carbide and the ferrite phase was operative in this system. This relationship, described stereographically by Andrews et al. (1968), was reduced to matrix form by the present author:

$$\begin{bmatrix} h \\ k \\ l \end{bmatrix}_{bcc} = \begin{bmatrix} .742 & \overline{.667} & \overline{.075} \\ .650 & .742 & \overline{.167} \\ .167 & .075 & .983 \end{bmatrix} \begin{bmatrix} h \\ k \\ l \end{bmatrix}_{fcc}$$

Substitution of the accurately determined carbide zone axis $[\bar{1}\ 1\ 2]$ yielded the corresponding orientation $[\overline{6.44}\ \bar{1}\ 7.75]$ for the ferrite phase. Since the above Kurdjumov-Sachs relation is only one of 24 possible variants due to symmetry of the cubic system (Jaswon et al. 1948) the allowable rotation $(001)^{\frac{1}{4}}$ locates the ferrite zone axis within the standard stereographic triangle. That is:

$$[\bar{1}\ 1\ 2]_{M_{23}C_6} \quad // \quad [\bar{1}\ 6.44\ 7.75]_{\alpha}$$

A B.C.C. Kikuchi map within 10^{o} about the $[\bar{1}\ 6.44\ 7.75]$ Kikuchi pole was constructed (Fig. 3.8b) and compared with the ferrite diffraction pattern in Fig. 3.8a. The following observations were made:-

(a) The location, direction and spacings of the ferrite Kikuchi lines are in agreement with the constructed map.

(b) The nearest low index zone axes are $[\bar{1}\ 5\ 7]$ and $[\bar{3}\ 11\ 13]$ which are 4.27^{o} and 4.35^{o} respectively from the Kikuchi pole. Both of these zone axes may be derived from the ferrite diffraction spots thus confirming the interpretation of the Kikuchi lines and hence the Kurdjumov-Sachs orientation

relationship.

This result augments the reported relationships (Shackleton et al. 1969 and Bee et al. 1979) between pearlitic constituents with isostructural $M_{23}C_6$ carbides formed in alloy steels containing Mo and Cr. The present work is the only known reported observation of pearlite with a carbide constituent other than cementite coexisting with stable austenite at room temperature and is analogous to the pearlite system consisting of $(Fe, Mn)_3C$ and ferrite examined in detail by Dippenaar and Honeycombe (1973) in Fe-13Mn-0.8C. However, it was not possible to obtain a complete crystallographic description of the austenite and pearlite phases since the single beam tilt unit in the Philips EM200 electron microscope was used exclusively for magnetic correction due to the presence of ferrite. In addition, the existing subgrain structure of the pearlite required microdiffraction facilities which were unavailable. The above analyses were obtained by examining well developed pearlite colonies that were coarsened by prolonged ageing and thus far removed from the original nucleating grain boundary.

3.5 Summary

(a) The addition of molybdenum to austenitic manganese steel markedly influences the decomposition characteristics during isothermal ageing resulting in 5 distinct transformation reactions over the temperature interval 300^{o} - 900^{o} C.

(b) The formation of Widmanstatten carbide plates at low ageing temperatures is identical with that reported in the basic Hadfield alloy; i.e. $(Fe, Mn)_3C$ exhibiting the Pitsch relationship with the adjacent austenite.

(c) The proeutectoid grain boundary nucleated carbide was shown to be $M_{23}C_6$ with a cube-cube orientation relationship with the austenite grain into which it was not growing.

(d) The carbide constituent of the pearlite reaction was also found to be $M_{23}C_6$ which displayed the Kurdjumov-Sachs orientation relationship with the accompanying ferrite phase.

(e) Two further transformation reactions which were observed on ageing above 600^{o}C, discontinuous precipitation of $M_{23}C_6$ + solute depleted austenite and matrix hardening due to the precipitation of Mo_2C in austenite, are examined in greater detail in Chapter 4.

3.6 Discussion

3.6.1 Crystallography of the Pearlite Reaction

The pearlite reaction in molybdenum bearing austenitic manganese steels is similar in a number of respects to the pearlite formed during isothermal decomposition at elevated temperatures of plain carbon steels containing Cr and/or Mo. Firstly, the formation of the alloy carbides, $Cr_{23}C_6$ (Bee 1974) and $M_{23}C_6$ (Shackleton et al. 1969) are isomorphous with the Kappa carbide observed in the present work. Both Cr and Mo are stronger carbide formers than either Fe or Mn and replacement of cementite in the pearlitic product by alloy carbides is not unexpected when a sufficient quantity of the strong carbide forming elements is present. Secondly, the Kurdjumov-Sachs relation between the ferrite and carbide phases in both steels indicates a strong similarity in the pearlite nucleation processes. The K-S relation minimizes the interfacial surface energy between the pearlitic constituents since the matching of the closes packed planes in the fcc lattice (111) and the bcc lattice (110) gives the lowest degree of atomic misfit (Honeycombe 1976).

In the alloy Fe-13Mn-4Mo-1.2C the proeutectoid grain boundary carbide $M_{23}C_6$ was shown to have a cube-cube orientation relationship with the austenite grain (γ_2) into which it was not growing (Fig. 3.6). It can be envizaged that the carbide constituent of the pearlite formed on this product (Fig. 3.3a) is continuous in lattice orientation at the initial nucleating stage in analogy to the process observed in detail in the alloy Fe-13 Mn-0.8C (Dippenaar et al.1973). The K-S relation between the pearlitic ferrite and the adjacent austenite (γ_2) may be deduced from the crystallographic data obtained in the

present work, i.e.

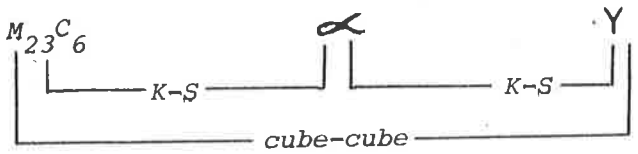

The pearlitic carbide and ferrite in this case would have a low energy interface with the grain boundary nucleated carbide and a high energy interface of high mobility with the austenite grain (γ_1) in which colony growth occurs.

3.6.2 Influence of Carbon on the Transformation Rate of the Pearlite Reaction

It has been reported (Collette et al. 1957, Fig. 2.2) that a reduction in the carbon content of the basic Hadfield steel results in a decreased transformation rate of the pearlite reaction. A similar effect has also been observed in the present work (Table 3.1b). The following mechanism is proposed to account for this phenomena.

It can be determined from volume fraction analysis of newly formed pearlite nuclei and from the stoichiometry of the carbide that the mean carbon content of pearlite in the alloy Fe-13Mn-1.2C is approximately 3%C. At long isothermal ageing times, when most of the austenite has transformed to pearlite, the mean carbon content of the colonies tends towards the original composition of the steel, that is 1.2%C. Thus, the carbide content of the pearlite at the advancing front must gradually decrease with colony growth. This effect may be achieved by an increase in the interlamellar spacing of the carbide phase. Indeed, this is augmented by reported observations of lamellar

coarsening at the advancing front of well developed pearlite colonies by a number of workers.

Preferential partitioning of the manganese to the carbide occurs during pearlite formation in high manganese steels (Razik et al. 1974) and is the rate controlling step in the transformation process. Since the partitioning rate of manganese from the ferrite to the carbide decreases as the diffusion distance increases with coarsening of the ferrite lamellae it follows that the growth rate of the pearlite colonies will decrease with interlamellar coarsening. This may explain the observations by Irvine et al. (1956) and Imai et al (1962) that, although the nose of the pearlite reaction during isothermal ageing of austenitic manganese steels occurs at 600^{o}C, the transformation rate is a maximum of 500^{o}C where it has been shown (Dippenaar 1970) that the interlamellar spacing of the pearlite constituents is finer.

A number of predictions that can be used to test the validity of this proposal are outlined below:-

(a) Isothermal ageing of thin sheets of Fe-13Mn-1.2C in a carburizing atmosphere should accelerate the pearlite transformation rate. The ready supply of carbon will eliminate lamellar coarsening and produce a steel with a final carbon content of approximately 3%C. The ε martensite reaction normally observed in the austenite ahead of the pearlite colonies should be absent.

(b) Higher interlamellar spacing and greater coarsening should occur in Fe-Mn-C steels containing a lower carbon content.

(c) The carbide $(Fe,Mn)_3C$ at the advancing front of a well develope coarse pearlite nodule should contain a higher proportion of manganese than the carbide in the pearlite nucleus since

manganese partitioning from a greater volume of ferrite will occur during the coarsening stage.

3.6.3 Influence of Molybdenum on the Transformation Rate of the Pearlite Reaction

It can be seen from a comparison of Figs. 2.2a and 3.2a that the addition of 4%Mo to austenitic manganese steel greatly increases the incubation period for the onset of the pearlite reaction and also substantially reduces the overall transformation kinetics (Table 3.1b). A similar influence has been reported in the alloy Fe-4Mo-0.2C (Bee et al. 1979) and is attributed to the relatively slow substitutional diffusion of Mo which partitions to the carbide constituent of the pearlite colonies (to form alloy carbides) during the transformation reaction (Razik et al. 1976). Thus the sluggish pearlite transformation reaction in austenitic manganese steels containing Molybdenum is due to the accumulative effect of the slow diffusion of the substitutional solutes Mn and Mo to the carbide phase to form $(Fe,Mn)_{21}Mo_2C_6$.

3.6.4 Epsilon Martensite Formation

The structural change in the austenite immediately ahead of the developing pearlite colonies (Fig. 3.7b) substantiates the ε martensite formation reported in basic Hadfield steel (Imai et al. 1962). The extensive martensite formation is indicative of the $\gamma \rightarrow \varepsilon$ transformation reaction that occurs on subsequent cooling to room temperature after partial transformation to pearlite. Since it has been pointed out (Remy et al. 1974) that ε_{cph} may form in austenite of low stacking fault energy by superpositioning of stacking faults on every second $(111)_\gamma$ plane and it has been previously shown that there is carbon depletion of the remaining austenite as pearlite forms, it can be concluded that there is a reduction in the stacking fault energy of the austenite in this system as the carbon content is

lowered. This proposal also accounts for the observed presence of stacking faults in the austenite regions between closely spaced Widmanstatten cementite plates (Fig. 3.4b) and is an alternative explanation to that described elsewhere (Dippenaar 1970).

3.7 Conclusions

1. The decomposition of austenite in Fe-13Mn-4Mo-1.2C in the temperature range 475-625^{o}C results in the formation of an alloy pearlite consisting of $M_{23}C_6$ and ferrite.

2. The pearlite colonies are heterogeneously nucleated and nodular in appearance. The slow transformation kinetics, as compared with plain carbon steels, indicates the need for substitutional diffusion of Mo and Mn during the reaction. Well developed colonies consist of subgrains of carbide and ferrite exhibiting variants of the Kurdjumov-Sachs orientation relationship.

3. The orientation of the carbide constituent of pearlite nuclei is continuous with the grain boundary proeutectoid $M_{23}C_6$ which has a simple cube-cube relationship with the austenite grain (γ_2) into which it is not growing.

4. Long range diffusion of carbon to the pearlite colonies during isothermal ageing reduces the stability of the remaining austenite by lowering its stacking fault energy and results in the formation of ε martensite on subsequent cooling to room temperature.

3.8 Suggestions for Future Work

1. Since the alloy pearlite formed in the present system coexists with stable austenite at room temperature a detailed crystallographic analysis of the pearlite nuclei using electron micro-diffraction techniques may yield further insight into the mechanisms of the decomposition of austenite to alloy pearlite reported by a number of investigators in plain carbon steels containing Cr and Mo.

2. The origin and growth process of the observed subgrain structure of the alloy pearlite nodules (displaying variants of the Kurdjumov-Sachs relation) may also be elucidated by crystallographic examination of the pearlite nuclei.

3. A brief, casual examination of a commercial grade Hadfield steel containing 2%Cr indicated that an alloy pearlite reaction, similar to the present work, also formed and warrants further investigation.

CHAPTER 4

4. AGEING CHARACTERISTICS OF Fe-Mn-Mo-C ALLOYS ABOVE 600°C - MATRIX PRECIPITATION AND DISCONTINUOUS PRECIPITATION

4.1 Experimental Results and Observations on Matrix Precipitation

4.1.1 Alloy Composition

Precipitation of Mo_2C in austenite was accompanied by a substantial increase in hardness of the matrix. The maximum age hardening response was expected to occur in an alloy with the greatest degree of supersaturation, (Kelly and Nicholson(1963)). Reference to the phase diagram (Fig. 3.1) indicates that this condition is achieved in the alloy Fe-13Mn-8Mo-0.8C. Reducing the carbon content from 1.2% to 0.8% raised the solidus temperature by approximately 50°C and resulted in complete dissolution of the carbide at the solution treatment temperature of 1300°C. However, if it is assumed that all of the available molybdenum in this alloy is precipitated as Mo_2C then the composition of the matrix austenite would be reduced to Fe-13Mn-0.3C which, according to Fig. 2.1, White and Honeycombe (1962), Grigorkin et al. (1968), Drabnjok (1970), is unstable at room temperature. The alloy composition was modified to Fe-13Mn-7Mo-0.8 in order to retain stable austenite after complete precipitation of Mo_2C and thereby avoid the complicating effects of the martensitic transformation on the microstructural investigations and hardness measurements.

4.1.2 Ageing Characteristics

Micro hardness measurements of the matrix austenite regions containing precipitates (discussed in detail in the next section) indicated a hardness of approximately 550 HV_{200g} from the onset of

the reaction. However, similar measurements of the untransformed matrix showed that these regions maintained the solution treated hardness of 230 HV_{200g} even in the latter stages of the reaction. Consequently macro hardness measurements with a 10 kg load were used to study the progress of the reaction since the indentation measured an average hardness of both regions.

The age hardening characteristics of the alloy Fe-13Mn-7Mo-0.8C, determined at temperatures in the range 600°C-850°C using macro hardness measurements, are shown in Fig. 4.1a. These curves again illustrated the classical behaviour of an age hardening material and exhibited a higher peak hardness and hardening rate than Fe-13Mn-4Mo-1.2C at the same ageing temperatures (Fig. 3.2b). The curves also indicated that although overageing was marginal, e.g. a decrease in hardness from 550 to 490 HV_{10} at 650°C, there was a tendency for a lower degree of overageing to occur at higher transformation temperatures, i.e. 470 to 430 HV_{10} at 850°C. The time required to reach peak hardness at each temperature coincided with the time required for complete precipitation to occur in all regions of the matrix austenite which were previously precipitate free. The time of complete precipitation was determined optically and considered to be the point when a uniform dark etching appearance was observed throughout the microstructure.

The activation energy for the precipitation of Mo_2C in austenite was obtained from the slope of the straight line in the Arrhenius plot of the hardness data, Fig. 4.1b, and found to be 164 $\pm$ 10 KJ/gram-atom. This is considerably less than the activation energy of 245 KJ/gram-atom for the volume diffusion of molybdenum

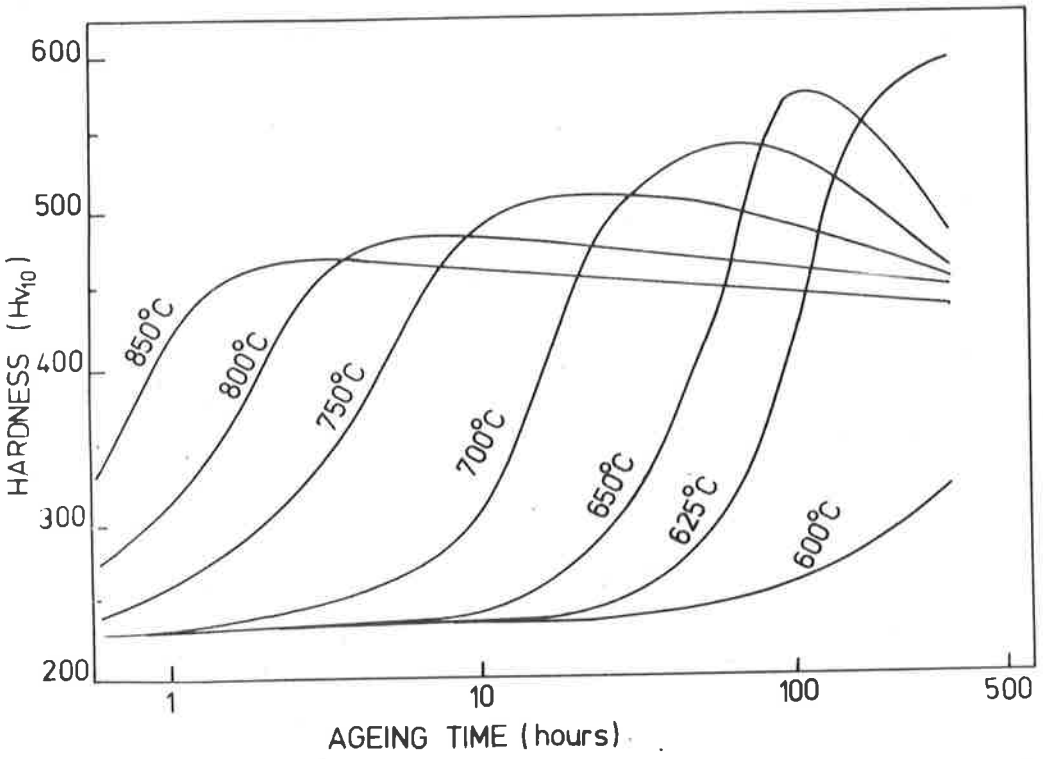

Fig. 4.1a. Age hardening characteristics of Fe-13Mn-7Mo-0.8C.

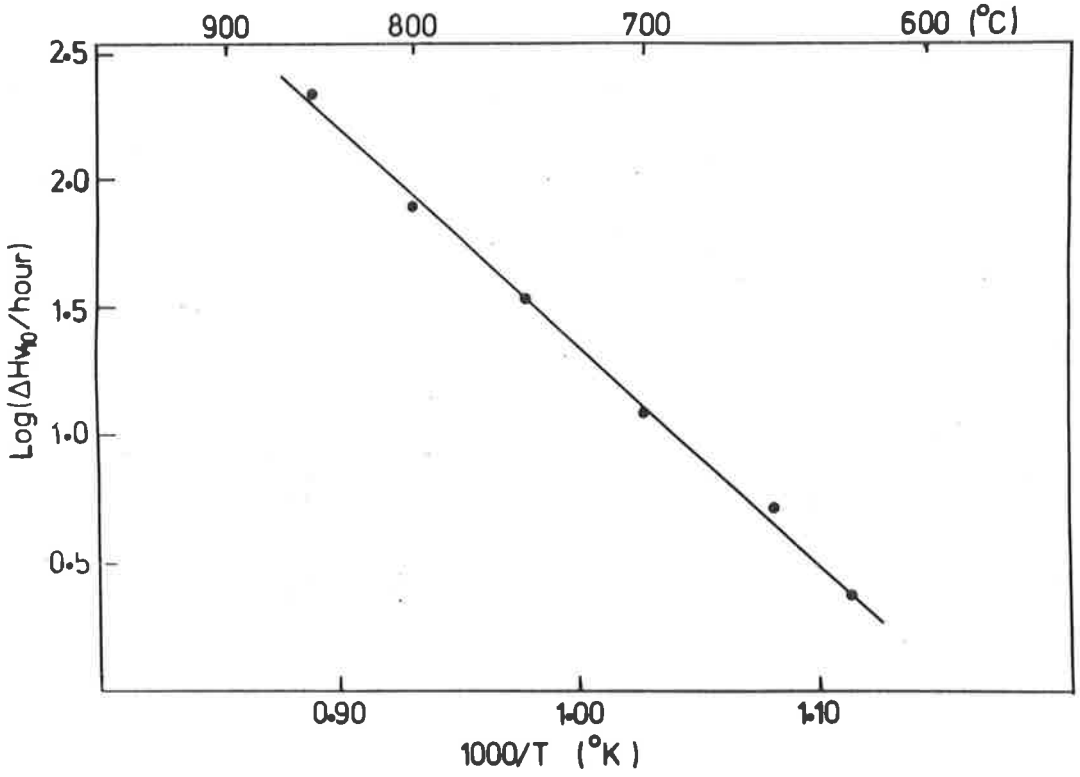

Fig. 4.1b Determination of activation energy from temperature dependence of the age hardening rate of Fe-13Mn-7Mo-0.8C.

in austenite reported by Ham (1945). Since volume diffisuion of molybdenum in austenite was clearly not the rate controlling step in the reaction a microstructural investigation was undertaken to elucidate the process responsible for the low activation energy.

4.1.3 Microstructural Investigation

The nucleation sites and mode of growth of the precipitates are illustrated in the series of optical micrographs in Fig. 4.2. Nucleation was observed to occur heterogeneously at grain boundaries and around inclusions or undissolved carbide particles. Growth of the precipitates occurred by broadening of the grain boundary zones and the development of stringers of precipitates within the grains. This mode of precipitation has been observed in a number of other alloy systems; (Nb-N, de Lamotte et al. (1967) , Fe-Mo, Hornbogen (1963), Fe-Sn, Predel et al. (1973)), and has been described as a heterogeneous precipitation process (Hornbogen (1972)).

The precipitate was too fine to be resolved in the optical microscope and it was only by electron microscopy techniques using thin foils and carbon extraction replicas that its nature was revealed. The bright field electron micrograph, Fig. 4.3 showed that the reaction product formed as sheets which were found to consist of a fine dispersion of particulate precipitates when tilted normal to the electron beam. The particle size of the precipitates varied from 20-50 nm in width.

A detailed electron microscopy examination using carbon extraction replication revealed that there was a change in the morphology

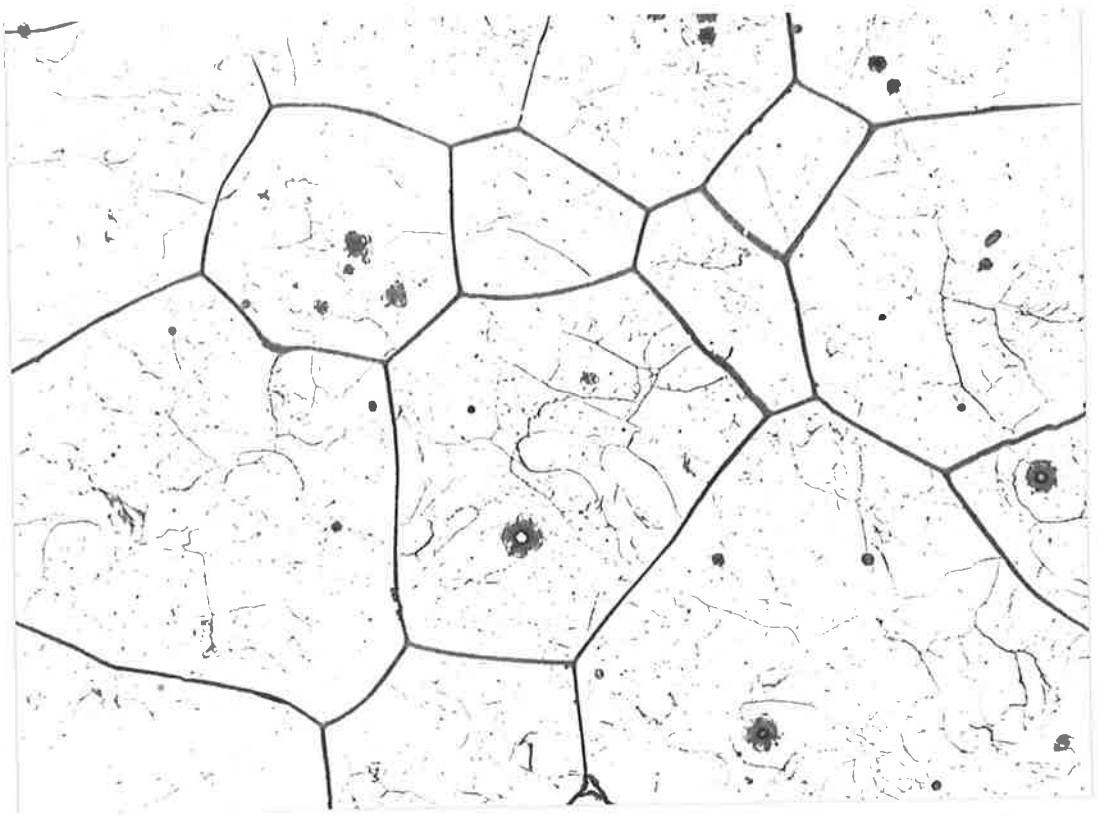

Fig. 4.2a. Fe-13Mn-7Mo-0.8C aged at 750°C for 1 hour.
Optical micrograph x 150

Fig. 4.2b. Fe-13Mn-7Mo-0.8C aged at 750°C for 5 hours.
Optical micrograph x 150

Fig. 4.3. Fe-13Mn-7Mo-0.8C aged at 750°C for 1 hour. Thin foil electron micrograph x 25,000

of the precipitating phase with transformation temperature. The various configurations of the reaction product could be illustrated at the two ageing temperatures, 750°C and 850°C.

(a) Fine Structure at 750°C

Carbon extraction replication after partial transformation at 750°C, Fig. 4.4a, showed that the grain boundary precipitates and the stringers within the grains consisted of closely pack Widmanstatten sheets of fine precipitate particles. The analysis of a selected area electron diffraction ring pattern of the replica Fig. 4.4b, showed the crystal structure of the extracted precipitate was hexagonal close packed with the following lattice parameters:-

$$a = 0.300 \text{ nm}$$

$$c = 0.483 \text{ nm}$$

The structure was identified as Mo_2C by comparison with published data. The relatively coarse particles located in the immediate vicinity of the austenite grain boundary were identified as $M_{23}C_6$ by SAD. Thin foil examination of solution treated specimens showed the presence of 'clean' austenite grain boundaries indicating that these coarse particles also formed during ageing.

(b) Fine Structure at 850°C

Isothermal ageing at 850°C produced two distinct distributions of the Mo_2C phase (Fig. 4.5a). A random dispersion of particulate Mo_2C precipitates, varying in size up to a maximum of 250 nm, formed throughout the matrix. Widmanstatten sheets consisting of particulate and fibrous Mo_2C precipitates formed in a number of directions. Coarse particles of $M_{23}C_6$ were again observed along the austenite grain boundaries.

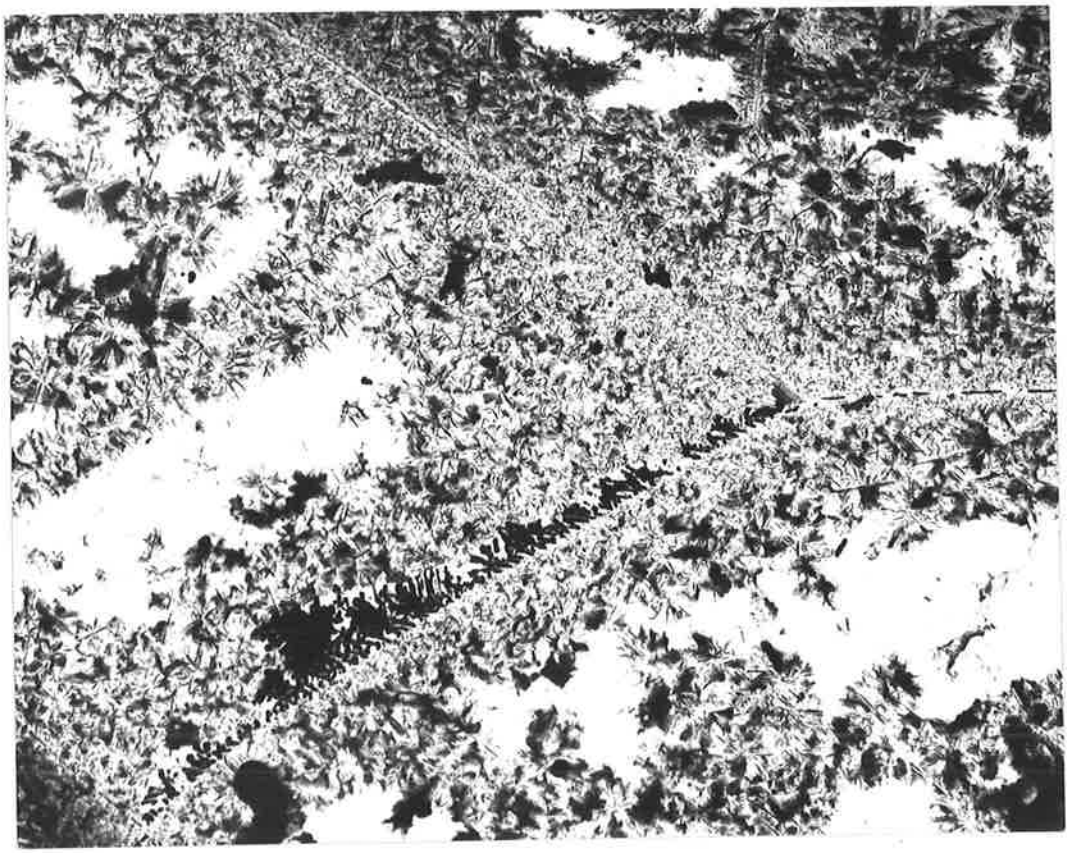

Fig. 4.4a. Fe-13Mn-7Mo-0.8C aged at 750°C for 5 hours. Carbon extraction replica x 12,000

Fig. 4.4b. SAD ring pattern of fine precipitates in fig. 4.4a.

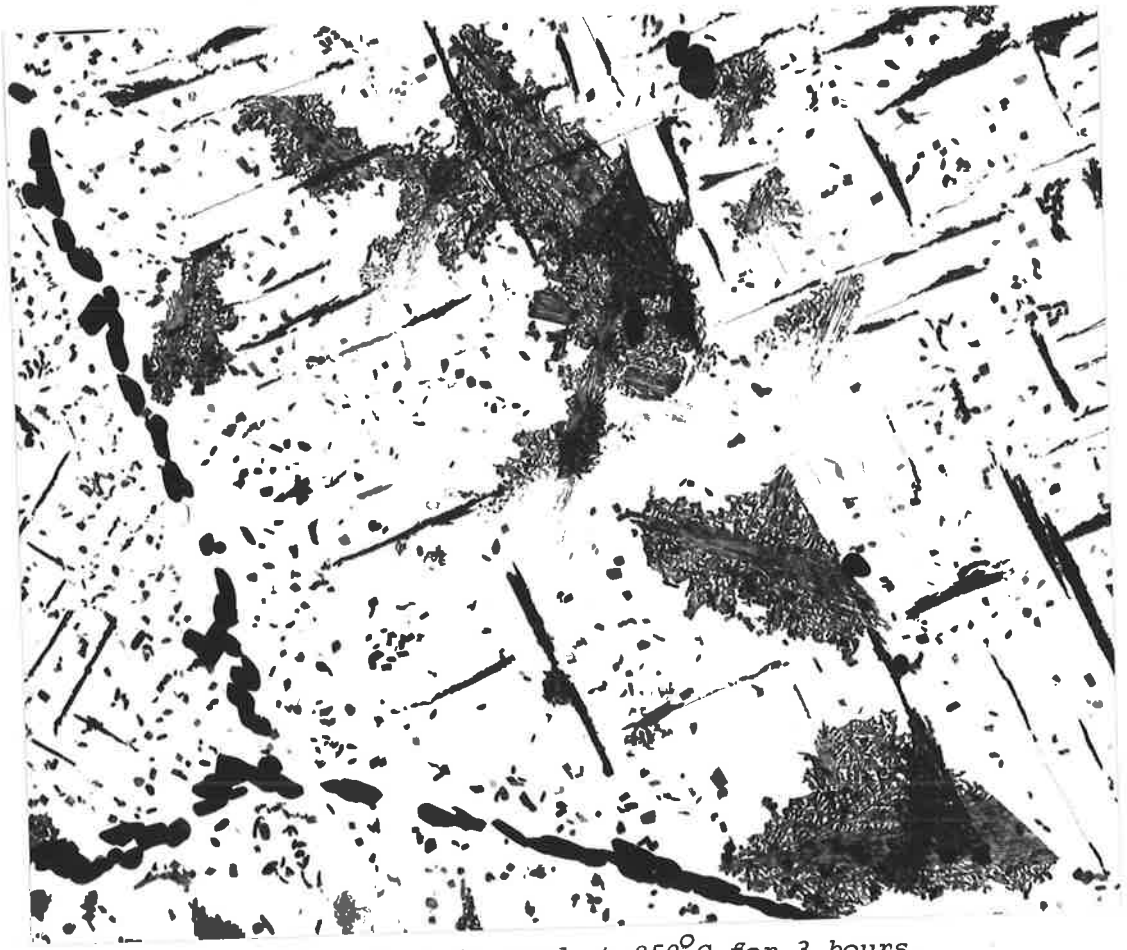

Fig. 4.5a. Fe-13Mn-7Mo-0.8C aged at 850°C for 3 hours. Carbon extraction replica x 13,500

Fig. 4.5b. Fe-13Mn-0.8C aged at 850°C for 3 hours. Carbon extraction replica x 31,000

A Widmanstatten sheet of fibrous and particulate precipitates is shown in greater detail in Fig. 4.5b. The sheet consists of a number of aligned fibres varying in width from 20-50 nm and approximately 5,000 nm in length. It appears from observations of a number of extraction replicas at different ageing times that in the latter stages of the development of the Widmanstatten sheets the fibrous morphology degenerated into a particulate morphology with particles ranging in size from 20-100 nm in width.

Thin foil exanimation showed that the distribution of the precipitates illustrated in the above extraction replicas was a true representation.

The microstructure of the matrix austenite examined by thin foil techniques at peak hardness was found to be stable at room temperature with no indication of decomposition to α or ε martensite. The continuity of the orientation of the austenite through the precipitate regions is shown by the uniform contrast conditions of the matrix in the dark field electron micrograph (Fig. 4.6). The presence of dislocations in the austenite immediately adjacent to the Mo_2C precipitates were always observed.

It was previously noted from optical metallographic studies that Mo_2C precipitates nucleated preferentially in the vicinity of undissolved carbides within the grains. Closer examination of these sites using thin foil techniques (Fig. 4.7a) revealed a network of dislocations around these particles in the solution treated condition due to thermal stresses set up on quenching. Harding and Honeycombe

Fig. 4.6. Fe-13Mn-7Mo-0.8C aged at 750°C for 1 hour.
Thin foil electron micrograph x 21,000

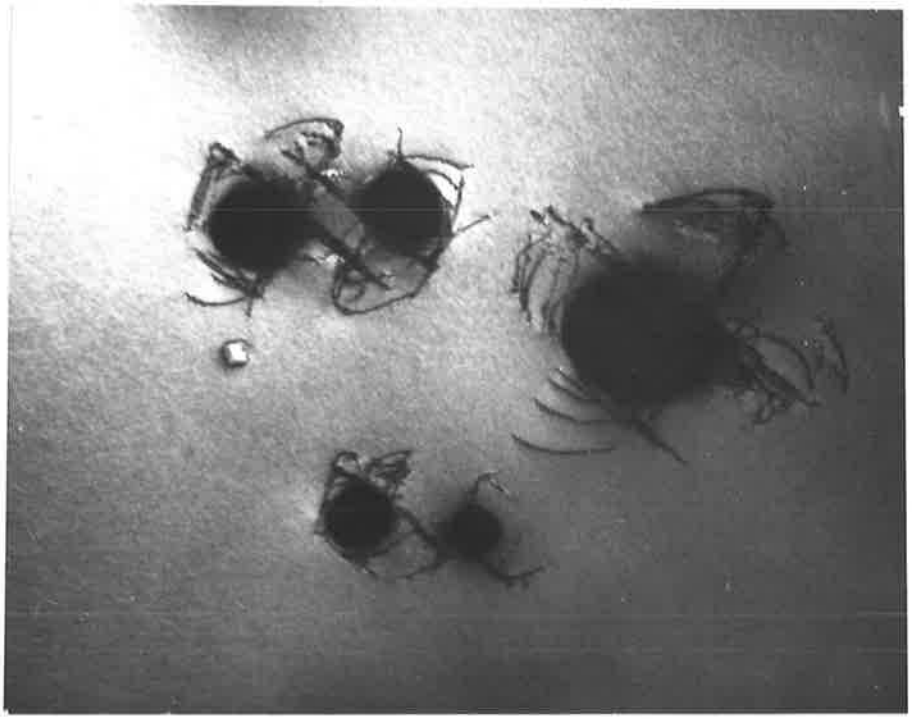

Fig. 4.7a. Fe-13Mn-7Mo-0.8C water quenched from 1300°C.
Thin foil electron micrograph x 25,000

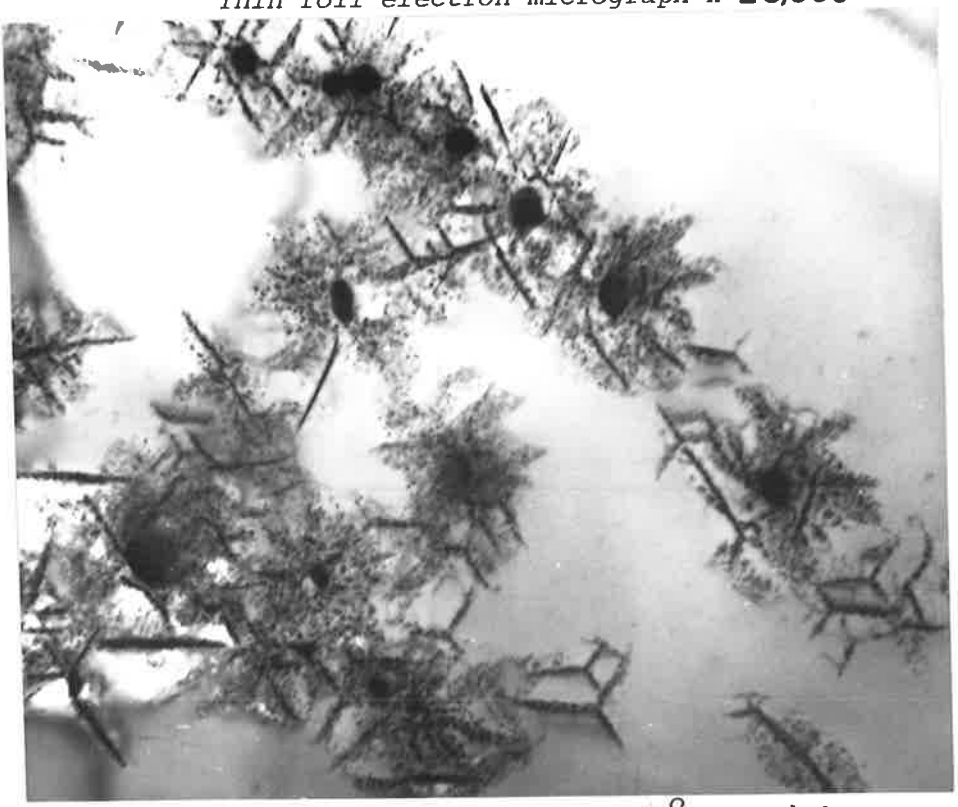

Fig. 4.7b. Fe-13Mn-7Mo-0.8C aged at 750°C for ½ hour.
Thin foil electron micrograph x 15,000

(1966) observed a similar effect around TiC particles in quenched Cr-Ni-Ti austenitic steel. After a short ageing time at 750°C localized precipitation of Mo_2C was observed at these sites which were surrounded by precipitate free regions suggesting that nucleation occurred on the existing dislocations (Fig. 4.7b). Borland and Honeycombe (1970) reported a localized precipitation behaviour of niobium nitride in Cr-Ni-Nb austenitic steels around undissolved particles within the grains and attributed the process to precipitation on quenched-induced dislocations.

4.1.4 Crystallography of Mo_2C Precipitation in Austenite

Two crystallographic aspects of the precipitation of Mo_2C in austenite were examined by thin foil electron microscopy techniques.

(a) Habit plane of the fibrous and particulate sheets.

(b) The orientation relationship between Mo_2C and austenite.

(a) Austenite Habit Plane

The habit planes of the sheets of Mo_2C precipitates in austenite (Fig. 4.8) were determined by trace analysis and found to be (110) type.

(b) Orientation Relationship

The following orientation relationships between Mo_2C and austenite has been reported by Honeycombe (1976) and agrees with the predicted relationship between an h.c.p. structure in a f.c.c. matrix, Jack (1974).

$$[00.1]\ c \quad // \quad [111]\ Y$$

$$[11.0]\ c \quad // \quad [1\bar{1}0]\ Y$$

$$[1\bar{1}.0]\ c \quad // \quad [11\bar{2}]\ Y$$

Fig. 4.8 Fe-13Mn-7Mo-0.8C aged at 750°C for 1 hour. Thin foil electron micrograph x 13,000

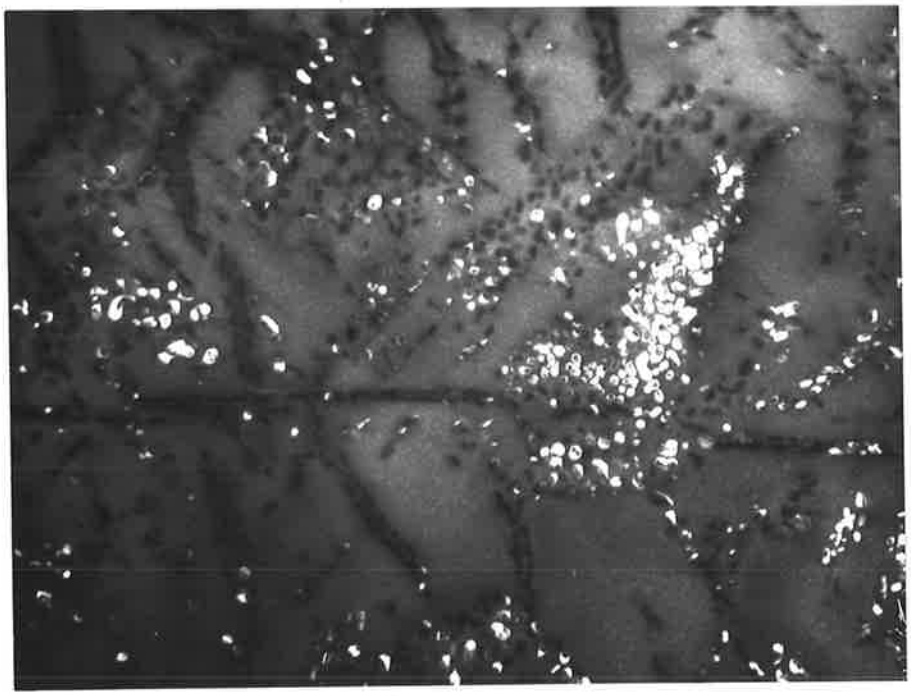

Fig. 4.9 Fe-13Mn-7Mo-0.8C aged at 750°C for 20 hours. Thin foil electron micrograph x 31,000

The $[\bar{1}11]$ zone axis in the austenite phase was readily obtained in the electron microscope by tilting in reciprocal space along (220) Kikuchi pairs in a thick region of the grain. A superimposed spot pattern of austenite and Mo_2C in a thinner region of the same grain at this tilt condition yielded an orientation relationship consistent with this data. A dark field electron micrograph using a strongly diffracting Mo_2C spot (Fig. 4.9) showed that only a portion of the precipitates lit up indicating that several variants of the orientation relationship occurred.

4.1.5. Effect of Cold Working on Ageing Characteristics

The role that dislocations play on the nucleation and propagation of the Mo_2C precipitates was investigated by examining the effects of prior cold working of the solution treated austenite on the kinetics and microstructure of the precipitation reaction. The alloy Fe-13Mn-7Mo-0.8C was deformed a nominal 5, 10 and 20% elongation by uniaxial tension and isothermally aged for periods up to 25 hours at 650°C and 750°C (Fig. 4.10). The age hardening characteristics of both temperatures were markedly affected by the introduction of prior cold working. The hardening rate increased with the degree of deformation while the incubation period for the reaction was greatly reduced. The maximum value of peak hardness was achieved with the greatest amount of deformation.

The microstructure after cold working and subsequent ageing is shown in the electron micrograph in Fig. 4.11. The previously observed Widmanstatten array of sheets of particulate precipitates was replaced with a more uniform distribution of fine precipitates associated with

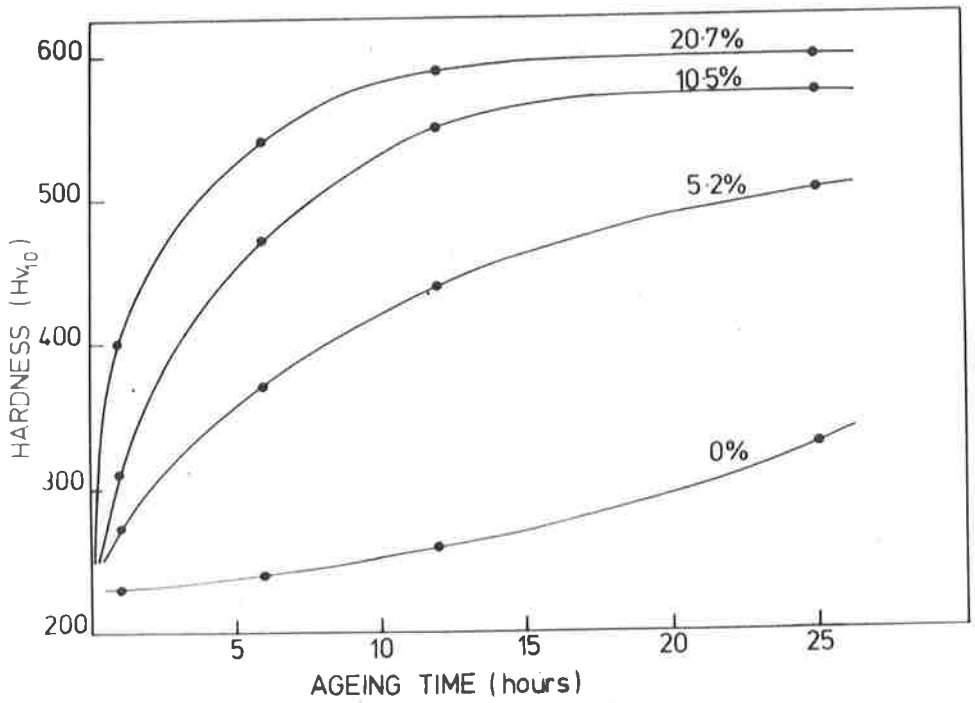

Fig. 4.10a. Effect of prior deformation on ageing characteristics of Fe-13Mn-7Mo-0.8C at 650°C.

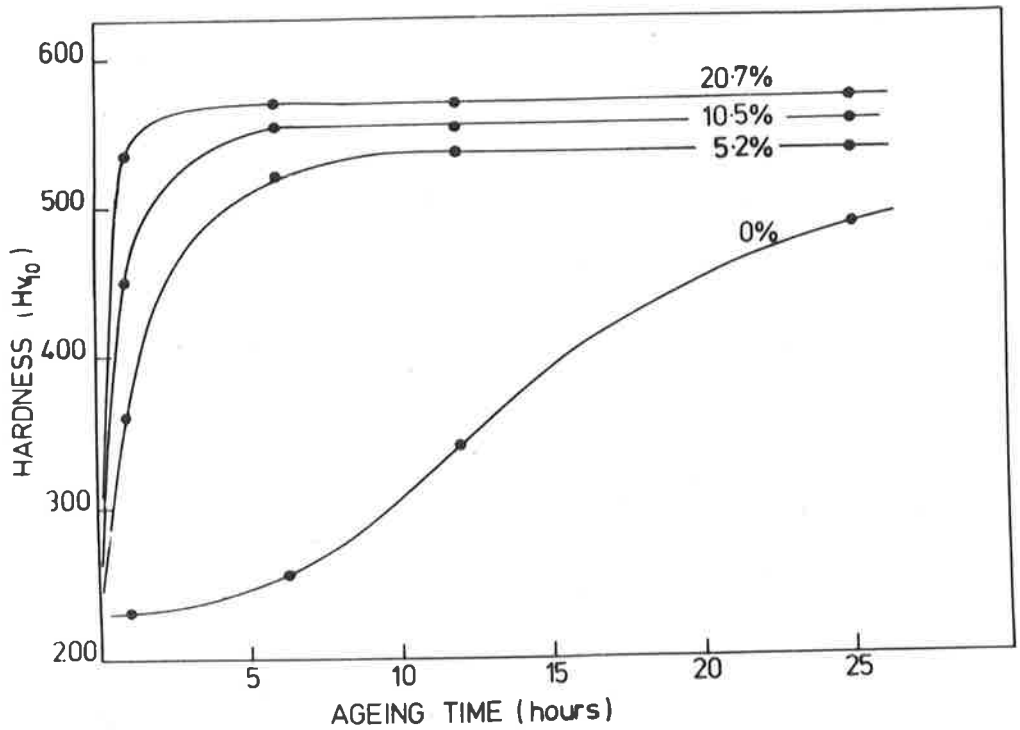

Fig. 4.10b. Effect of prior deformation on ageing characteristics of Fe-13Mn-7Mo-0.8C at 750°C.

Fig. 4.11 *Fe-13Mn-7Mo-0.8C deformed 5% and aged at 750^{O} for 1 hour. Thin foil electron micrograph* x 15,000

line dislocations. Chaturvedi et al. (1968) observed a similar change in precipitate distribution when the dislocation density was increased by deformation prior to ageing.

4.1.6 Summary

The alloy Fe-13Mn-7Mo-0.8C exhibited substantial age hardening in the temperature range 600-850^{o}C due to the heterogeneous precipitation of fine particulate and fibrous Mo_2C in austenite. The following criteria for heterogeneous precipitation, defined by Hornbogen, have been observed:-

(a) precipitation initiated at dislocations.

(b) the orientation of the matrix was unchanged by the precipitation process.

(c) the precipitates formed in sheets with a crystallographic habit plane.

(d) the presence of localized dislocation networks around the growing precipitates, possibly due to strains induced by a volume change, suggests a process for the autocatalytic nature of the reaction.

The observed growth rate of the precipitates was somewhat higher than that expected from normal volume diffusion of Mo in austenite and the rate accelerated with increased dislocation density induced by prior cold working.

4.2 Experimental Results and Observations on Discontinuous Precipitation

4.2.1. Alloy Composition

Inspection of the preliminary microstructural investigations of the Fe-Mn-Mo-C system (Table 3.1) indicated that the alloy Fe-13Mn-4Mo-1.2C contained the optimum Mo/C ratio that yielded the maximum volume fraction (20%) of the d.p. product on isothermal ageing. At higher Mo/C ratios matrix precipitation of Mo_2C predominated at the expense of the d.p. reaction, for example only 1% volume fraction was observed in the alloy Fe-13Mn-7Mo-0.8C after ageing under identical conditions. The paucity of the d.p. product in alloys containing less than 4% Mo could be attributed to their low level of solute content in the solution treated condition since a high degree of super saturation is a dominant factor in alloys exhibiting discontinuous precipitation (Hornbogen 1972).

4.2.2 Microstructural Investigation

The general features of the d.p. reaction are illustrated in the optical micrograph in Fig. 4.12a. Precipitation of lamellar carbide in austenite initiated at grain boundaries and approximately hemispherical shaped colonies formed by growth into the adjacent grain. The reaction is shown schematically in Fig. 4.12b and may be described in the expression:

$$Y_1 \longrightarrow Y_2 + \text{carbide}$$

There was a tendency for well developed nodules to exhibit lamellar coarsening at the advancing interface which also adopted an extremely irregular configuration. The precipitation of Mo_2C in austenite, described in the previous section, occurred simultaneously in the matrix ahead of the d.p. reaction.

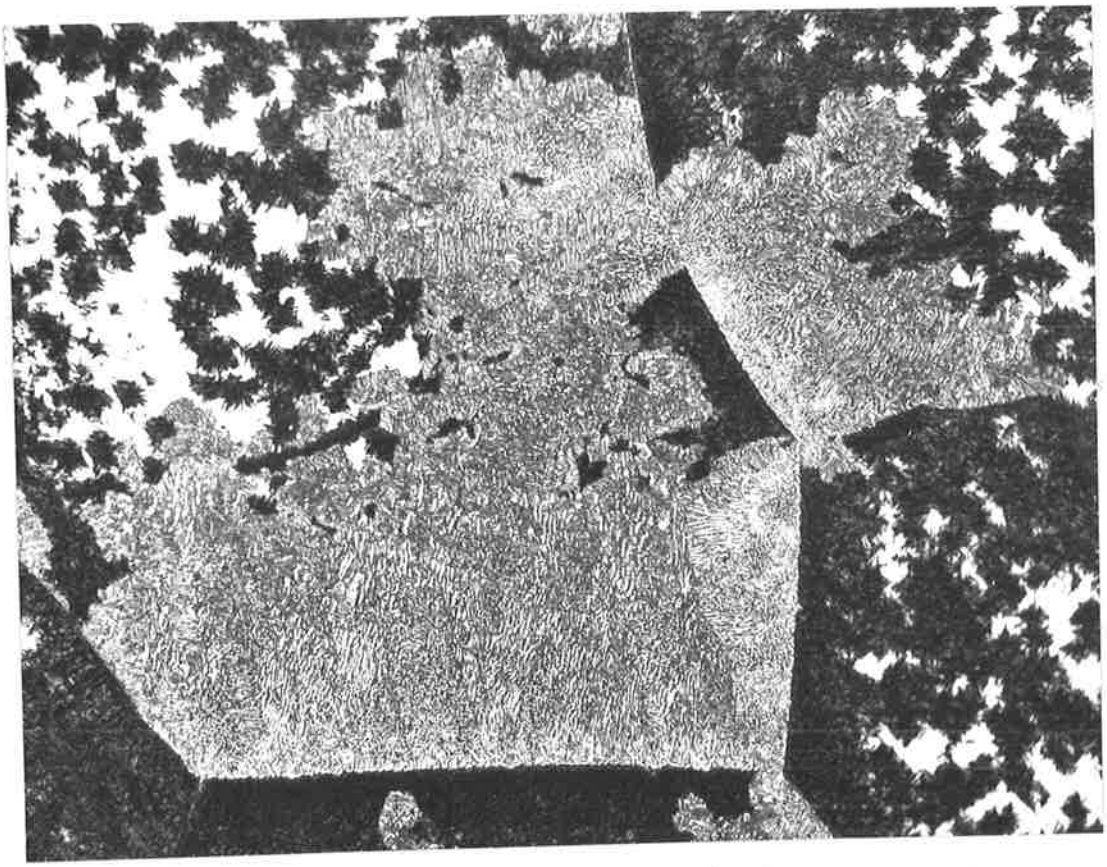

Fig. 4.12a Fe-13Mn-4Mo-1.2C aged at 750°C for 12 hours. Optical micrograph x 500

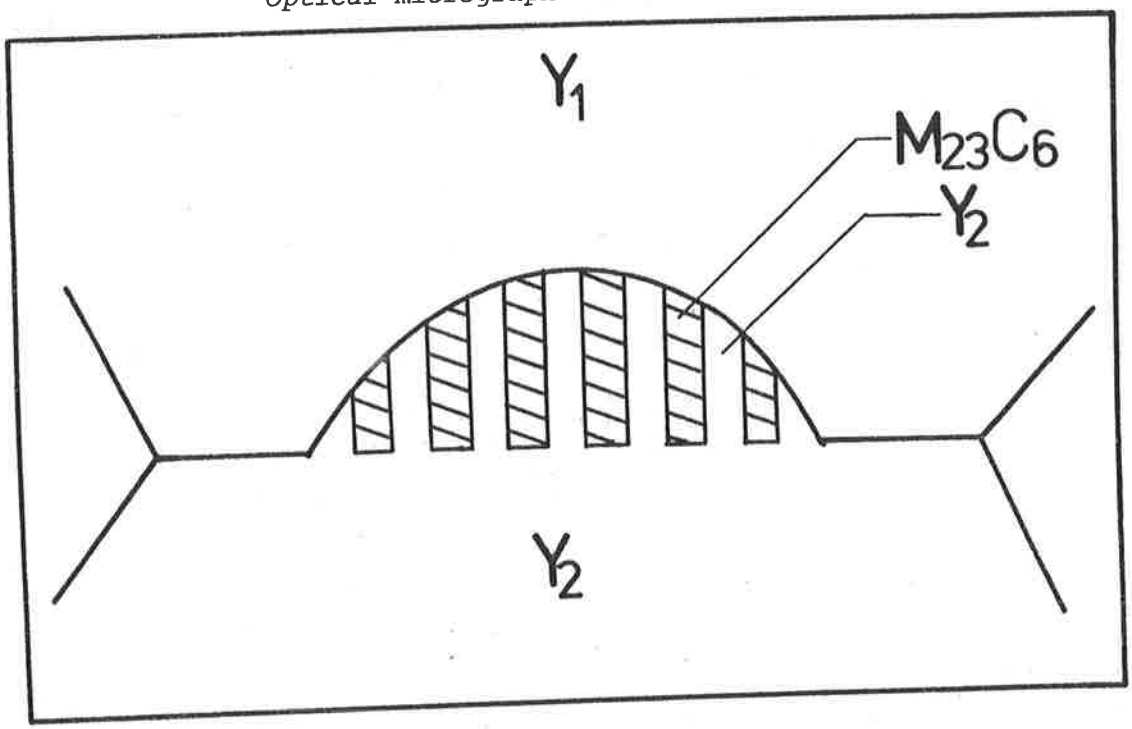

Fig. 4.12b Schematic diagram of a d.p. colony formed on an austenite grain boundary and growing hemispherically into one of the austenite grains (Y_1).

The grain boundary nucleation and early stages of growth of the d.p. reaction were examined by thin foil electron microscopy techniques. It was observed that within 30 minutes of ageing at 750°C coarse carbides had formed at grain boundaries (Fig. 4.13a). Dark field imaging techniques, using a strong diffraction spot from Y_2 showed that its orientation was continuous with the austenite in the colony indicating that the reaction was accompanied by grain boundary migration (Fig. 4.13b). The specimen was tilted to obtain an [001] Kikuchi pole from Y_2 and a spot pattern of the colony was recorded at the same tilt conditions (Fig. 4.14). Analysis of the diffraction patterns revealed the following results:-

(a) The carbide in the colony was a face centred cubic structure with a lattice parameter of 1.062 nm and was identified as $M_{23}C_6$ by comparison with published data.

(b) The carbide and austenite in the colony exhibited a cube-cube orientation relationship in agreement with the findings of Lewis et al. (1965):-

$$(hkl)\ C \quad // \quad (hkl)\ Y$$

$$[uvw]\ C \quad // \quad [uvw]\ Y$$

(c) The parallel [uvw] zone axes of Y_2 and the austenite in the colony confirmed the continuity of the orientation of the austenite across the original site of the grain boundary shown by dark field microscopy.

This reaction is a classical example of a discontinuous precipitation process (Hornbogen 1972, Fournelle et al. 1972 and Tu 1972) and has previously been observed in a host of alloy systems including austenitic manganese steel supersaturated with vanadium (Ainsley et al. 1979) and austenitic stainless steels containing excessive carbon (Kotval et al. 1969, Hillert et al. 1971, Pumphrey et al. 1974).

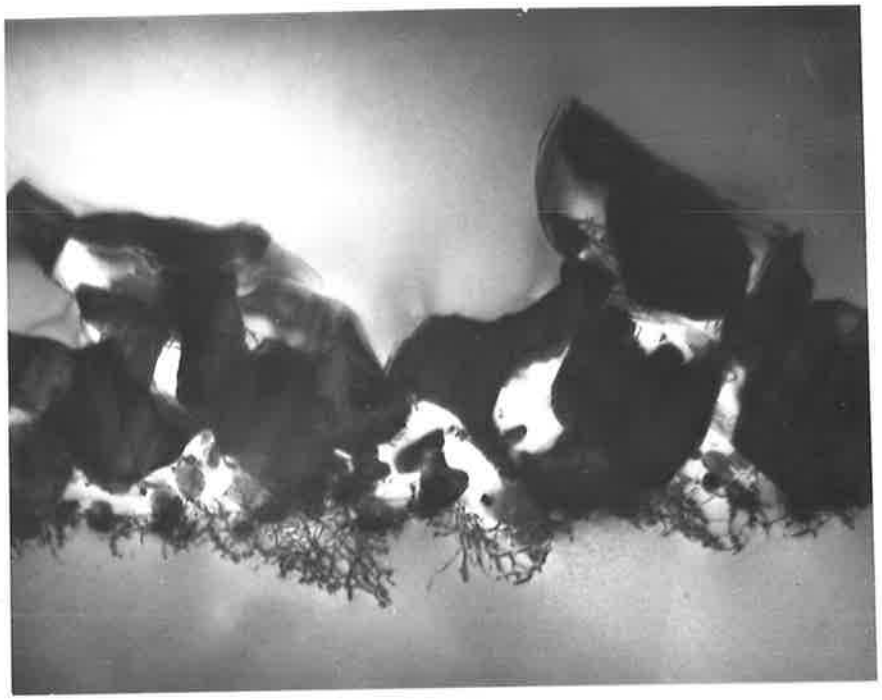

(a)

(b)

Fig. 4.13 Fe-13Mn-4Mo-1.2C aged at 750°C for ½ hour. Thin foil electron micrographs x 22,000

(a) bright field image.
(b) dark field (Y_2) image.

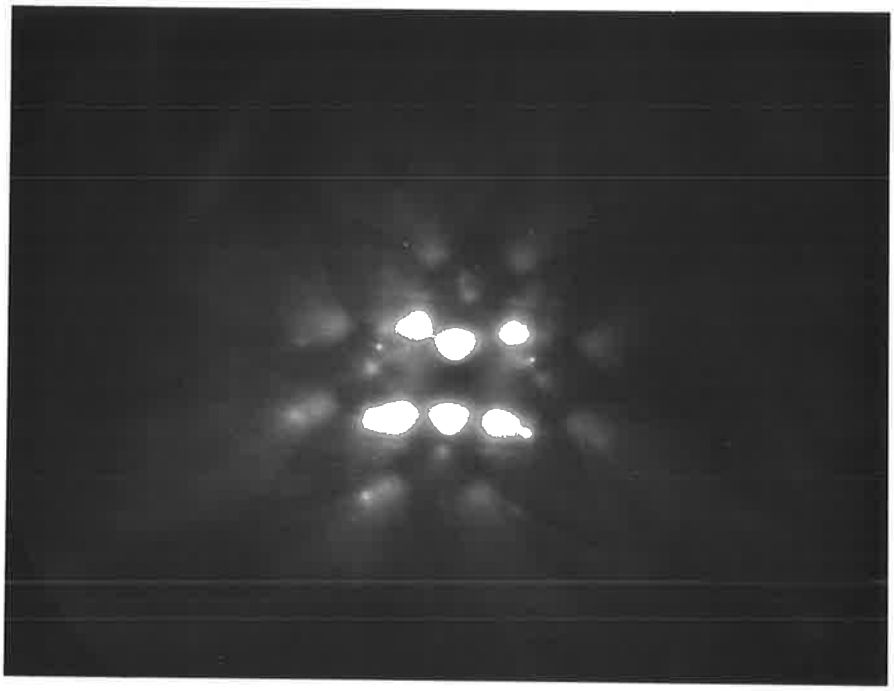

Fig. 4.14a. [001] *Kikuchi pole of* Y_2 *in Fig. 4.13.*

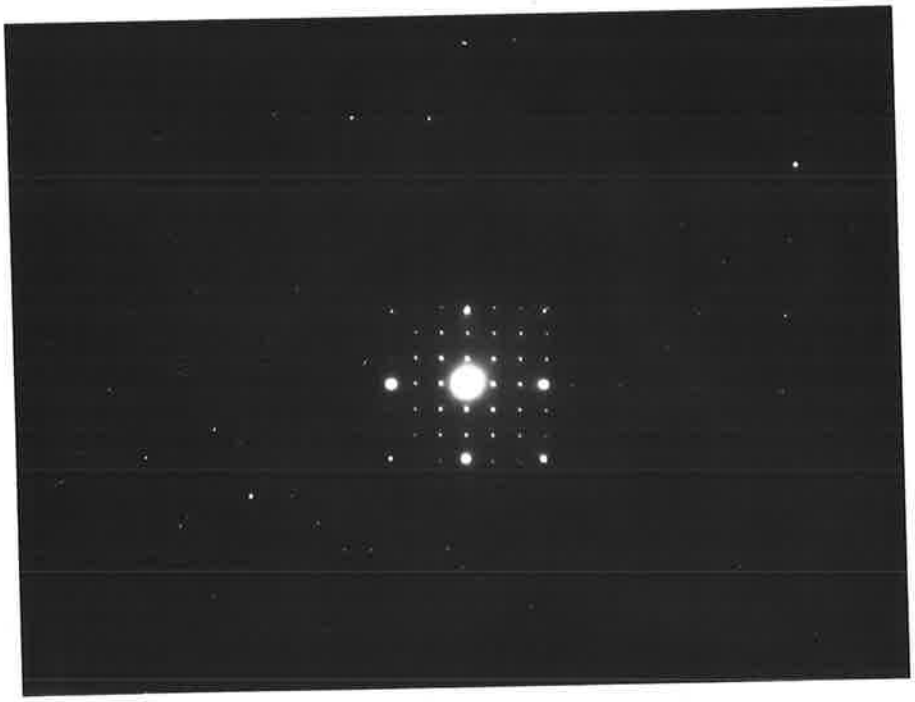

Fig. 4.14b. Superimposed [001] *spot pattern of colony in fig. 4.13.*

4.2.3 Characterization of Y_1/Y_2 Grain Boundary Structure

It has been shown with the aid of grain boundary models, e.g. the Coincident Site Lattice model (Kronberg and Wilson 1949, Brandon et al. 1964) that the growth of a boundary dependent process may be inhibited by an acquired structure of the advancing grain boundary (Demianczuk 1975). The grain boundary migration accompanying the d.p. reaction is favoured by an incoherent high energy boundary which is described in the CSL model by a high Σ value. This criterion was applied in the current study to determine whether the nature of the advancing grain boundary of the d.p. colony was responsible for the observed arrest in the growth of the colonies during isothermal ageing.

The analysis of a Kikuchi pattern from Y_1 and Y_2 yielded the following orientation relationship:-

$$[\overline{.188} \quad .229 \quad .955]\ Y_1 \ // \ [\overline{.317} \quad .534 \quad .784]\ Y_2$$
$$[.712 \quad .701 \quad \overline{.028}]\ Y_1 \ // \ [.469 \quad \overline{.630} \quad .619]\ Y_2$$

The misorientation between these grains was established using the method of Young et al. (1973) and is described by the axis/angle pair:-

$$[\bar{1} \quad 4.069 \quad 7.991] \ /71.2^{o}$$

The associated Σ value for the axis/angle pair $[\bar{1}\ 4\ 8]\ /71.2^{o}$, using the method of Ranganathan (1966), is approximately 949 indicating an extremely low CSL relationship between Y_1 and Y_2.

The analysis of the technique used for determining the axis/angle pair indicated that an experimental error of $\pm 2^{o}$ in both the rotation axis and rotation angle was a conservative estimate. An inspection of a prepared list of CSL relationships for $\Sigma \leq 99$ showed that the Σ value for all pairs considered within the range of the experimental errors was greater than this limit.

It can be concluded that the incoherent, high energy boundary of the advancing d.p. colony was maintained during all stages of the precipitation reaction and the arrest in the growth of the colony was brought about by a change in the nature of the matrix austenite at the Y_1/Y_2 interface.

Since d.p. and matrix precipitation occurred concurrently (Fig. 4.12a) an interaction would be expected between these reactions as both compete for solutes, molybdenum and carbon, in the alloy during ageing. This aspect is examined in detail in the following section.

4.2.4 Summary

Discontinuous precipitation of colonies consisting of lamellar $M_{23}C_6$ and solute depleted austenite accompanied by grain boundary migration occurred in the alloy Fe-13Mn-4Mo-1.2C on isothermal ageing. $M_{23}C_6$, in agreement with previous work in Cr-Ni austenitic steels (Lewis et al. 1965, Pumphrey et al. 1974), adopted a cube-cube orientation relationship with the austenite in the colony. The misorientation between the colony and the matrix into which it was growing suggested a low density of coincidence lattice sites between the two grains inferring that the reaction front consisted of a high energy migrating grain boundary.

4.3 Interaction Between Discontinuous and Matrix Precipitation Reactions

4.3.1 Microstructural Investigation

The simultaneous ageing characteristics of the d.p. and matrix precipitation reactions were examined in the alloy Fe-13Mn-4Mo-1.2C on ageing at 750°C to determine their mutual interaction. The volume fraction of the d.p. product was determined metallographically using the point counting technique while the progress of the matrix precipitate was observed by taking macro hardness measurements. It can be seen in Fig. 4.15 that the maximum volume fraction of the d.p. product was attained before peak hardness of the matrix and remained constant on further ageing. Examination of thin foils of well developed colonies showed that concave depressions in the advancing grain boundaries were frequently associated with the presence of Mo_2C in the matrix ahead of the colonies (Fig. 4.16).

An extraction replica of a d.p. colony and matrix precipitates obtained in the alloy Fe-13Mn-7Mo-0.8C is shown in Fig. 4.17. Localized impediment of the growth of the colony in direct contact with the Mo_2C precipitates is evident. An interesting point illustrated in this micrograph is the variation in the morphology of the carbide in the colonies with alloy composition. The lamellar plates and interlamellar spacings of the carbide in the colony in Fe-13Mn-7Mo-0.8C are about an order of magnitude finer than that observed in the alloy Fe-13Mn-4Mo-1.2C (Fig. 4.13).

A further confirmation that the presence of the matrix precipitate impeded the growth of the d.p. product was obtained by examining the effect of cold working on the ageing characteristics of the d.p. reaction. Since prior deformation accelerated the matrix precipitation

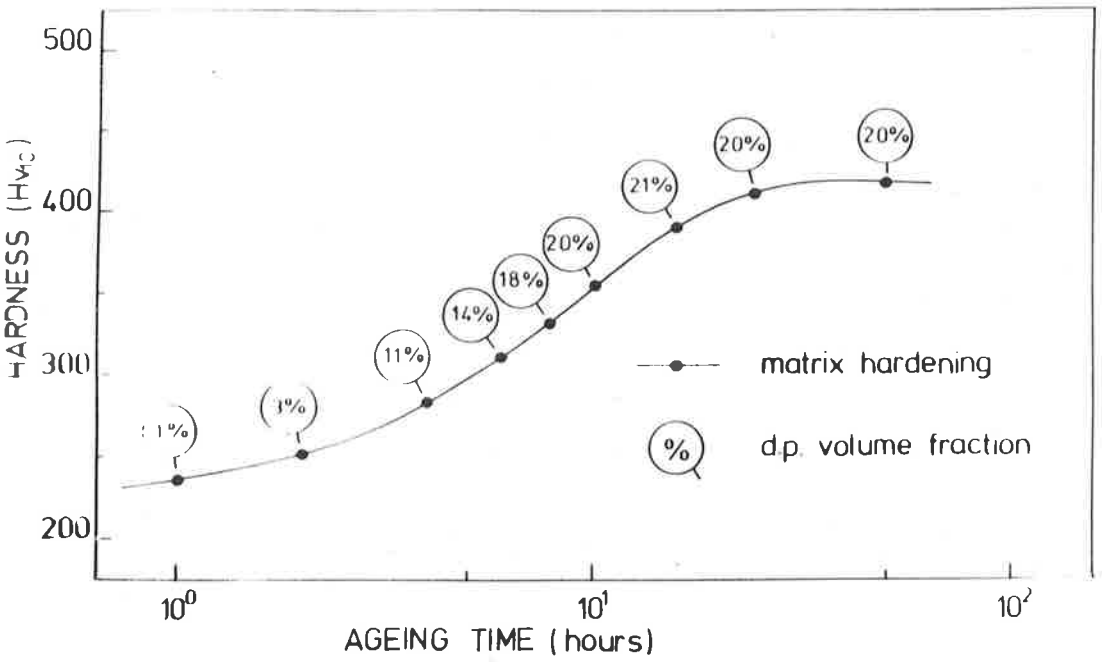

Fig. 4.15 Simultaneous progress of matrix and discontinuous precipitation Fe-13Mn-4Mo-1.2C at 750°C.

Fig. 4.16 Fe-13Mn-4Mo-1.2C aged at 750°C for 5 hours. Thin foil electron micrograph x **14,000**

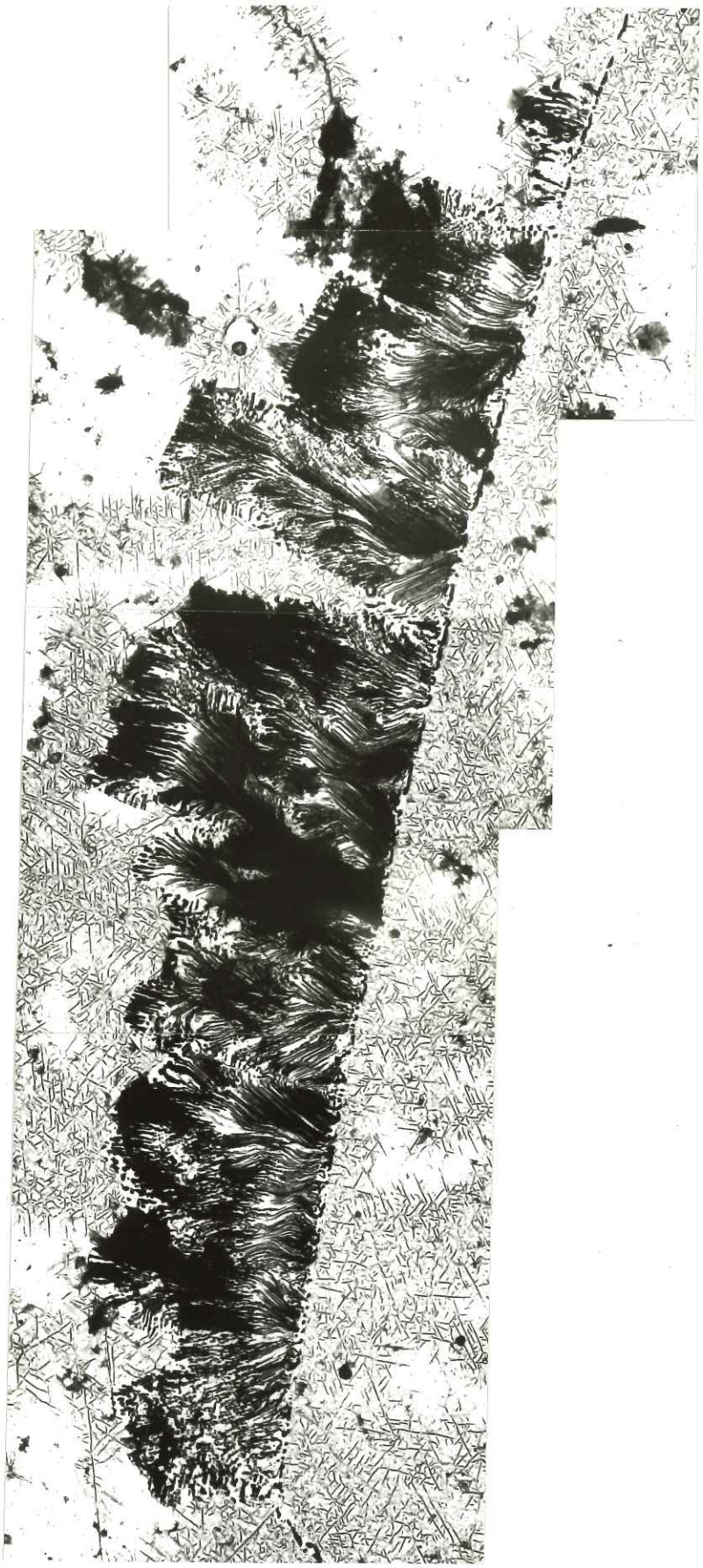

Fig. 4.17 Fe-13Mn-7Mo-8C aged at 750°C for 5 hours.
Carbon extraction replica x 8,500

reaction (Section 4.1.5) a corresponding decrease in the volume fraction of the d.p. product would be expected under these conditions (Hornbogen 1972). Indeed, when the alloy Fe-13Mn-4Mo-1.2C was deformed 20% and aged at 750^{o}C for 25 hours less than 1% volume fraction of the d.p. reaction product was observed by metallographic examination.

There was some evidence to suggest that the presence of the d.p. product enhanced the precipitation of the matrix reaction during ageing. A commonly observed feature during thin foil examination of the d.p. colonies was the development of bands of Mo_2C precipitates at the sites of original grain boundaries (Fig. 4.18). The thickness of these bands were observed to increase with ageing time and the direction of growth was invariably away from the colony into the Y_2 grain. This region, shown in the early stages of the formation of a d.p. colony (Fig. 4.13), was found to consist of a network of dislocations decorated by a fine dispersion of Mo_2C precipitates in the Y_2 grain immediately adjacent to the original Y_1/Y_2 boundary. The dislocations may have originated from lattice strains set up by the change in the lattice parameter of the solute depleted austenite in the colony and the formation of the $M_{23}C_6$ carbide (Pumphrey et al. 1974). It was further noted that the grain boundary formation of Mo_2C precipitates was always accompanied by the presence of coarse $M_{23}C_6$ carbide particles in the grain boundaries, (Fig. 4.4 and Fig. 4.17). It is suggested that similar strain induced dislocations were formed around these particles which then acted as nucleating sites for the matrix precipitation reaction.

Fig. 4.18 Fe-13Mn-4Mo-1.2C aged at 750°C for 2 hours. Thin foil electron micrograph x 10,000

4.3.2 Summary

The extremely irregular configuration of the advancing grain boundaries of the d.p. colonies was caused by bowing of the nodules around the heterogeneously formed Mo_2C precipitates in the matrix. The growth of the d.p. colonies was subsequently arrested after partial transformation by this competing reaction. Increasing the dislocation density of the austenite accelerated the progress of the heterogeneous reaction and consequently greatly retarded the d.p. reaction.

Bands of Mo_2C precipitate particles developed in the austenite (Y_2) in contact with the d.p. colonies at the sites of the original Y_1/Y_2 boundaries where lattice strain induced dislocations have been reported in similar reactions.

4.4 Discussion

It has been shown that two different types of transformation reactions, heterogeneous matrix precipitation of Mo_2C and grain boundary nucleated d.p. of coarse lamellar $M_{23}C_6$ + solute depleted austenite, occur during isothermal ageing of Fe-Mn-Mo-C alloys above 600°C. An attempt will be made in this section to delineate the factors influencing the occurrence of these reaction products.

4.4.1 Heterogeneous Precipitation of Mo_2C in Austenite

It has been shown that Mo_2C precipitates nucleate heterogeneously (Fig. 4.2a) at sites containing the presence of dislocation networks (Figs. 4.7 and 4.13) which are due respectively to:-

(a) thermal stresses around undissolved carbide particles (Fig. 4.7) in agreement with Silcock (1963), Harding et al. (1965) and Chaturvedi et al. (1968) who reported a similar effect on quenching Cr-Ni austenitic steels.

(b) Lattice strains generated at the $M_{23}C_6$/austenite interfaces as a result of the mismatch in these lattice parameters (Fig. 4.13b and 4.18), also observed by Beckitt et al. (1967) and Pumphrey et al. (1974) in Cr-Ni steels.

In addition, the acceleration of the precipitation reaction after prior cold working shown by age hardening effects (Fig. 4.10) and thin foil electron microscopy studies (Fig. 4.11) indicates that precipitation on dislocations is the primary mode of nucleation of Mo_2C in austenite in this system and is analogous to other carbide precipitation processes described in Cr-Ni steels mentioned above.

Further development of the Mo_2C precipitation reaction occurs by the growth of stringers (Fig. 4.4a) which were shown to be invariably associated with dislocations in the immediately adjacent austenite. These dislocations may be considered to have formed as a result of the lattice mismatch between Mo_2C and austenite (Honeycombe 1976) and suggests a mechanism for the autocatalytic nature of the reaction process: Mo_2C precipitates form on pre-existing dislocations punching out further dislocations in the matrix due to lattice strain effects and thus propagating in incremental steps (Fig. 4.8).

The $\{110\}$ habit planes of the sheets of Mo_2C precipitate particles are identical with the reported matrix (fcc) habit planes during repeated precipitation of the θ' phase on dislocations in the alloy Al-4Cu (Guyot et al. 1974) and $M_{23}C_6$ particles in Cr-N_i austenitic steels (Beckitt et al. 1967). It is further noted that the maximum degree of lattice misfit between austenite and Mo_2C occurs in the parallel planes $(11.0)_{Mo_2C}$ and $\{110\}$ (Honeycombe 1976) and may also be a significant factor in determining the habit planes of the Mo_2C precipitate sheets.

4.4.2 Discontinuous Precipitation

The precipitation of coarse lamellar $M_{23}C_6$ during isothermal ageing of Fe-Mn-Mo-C alloys is accompanied by grain boundary migration (Fig. 4.13b) and is a classical example of a d.p. reaction process (Hornbogen 1972, Sunquist 1973). Although most studies of d.p. have been made on much simpler binary alloy systems there is a host of different mechanisms that have been proposed to explain the nature of the driving force of the migrating grain boundaries (Tu and Turnball

1967, Fournelle and Clark 1972, Sulonen 1964, Hillert 1969 and Meyrick 1976). It is, however, generally recognised that the migrating grain boundary provides a rapid, short circuit path for solutes during discontinuous growth (Hillert and Purdy 1978).

A number of observations of an analogous d.p. reaction of $M_{23}C_6$ + solute depleted austenite have been reported in Cr-Ni austenitic steels containing excess carbon (Hillert and Lagneborg 1971) and several possible mechanisms proposed to explain the grain boundary migration process. It was suggested that the change in lattice parameter of the solute depleted austenite gives rise to lattice stresses which provide a driving force for boundary migration into the stressed region. However, in the present work the grain boundary is observed to move away from the stressed region, see for example Fig. 4.13b where dislocations form in the γ_2 grain to accomodate stresses due to both the austenite lattice parameter change and the formation of the $M_{23}C_6$ carbide. A further proposal was that the close orientation relationship (cube-cube) between $M_{23}C_6$ and one of the austenite grains (γ_2) may favour the growth of this grain from surface energy considerations. Nevertheless, it was often observed that the austenite grain boundaries bulge out far ahead of the carbide precipitate (Fig. 4.16) indicating that the d.p. process cannot be explained solely by the effect of a favourable orientation relationship between the colony constituents.

Further discussions of suggested mechanisms of solute segregation at the migrating grain boundary, expounded in depth for d.p. in binary alloy systems and as yet not fully resolved, seem

inappropriate in the current work when one considers the complicated structure of the precipitating carbide phase ($(Fe_{21}Mo_2)C_6$ in which some Fe atoms may be substituted by Mn atoms).

4.4.3 Interaction of the Precipitate Products

Fundamental to the discussion of the simultaneous formation of the heterogeneous Mo_2C and the discontinuous $M_{23}C_6$ carbides during isothermal ageing of Fe-Mn-Mo-C alloys above 600°C (Table 3.1a and Fig. 4.12a) is the question of why these two discrete reaction products occur under apparent equilibrium conditions. A consideration of the relative nucleation and growth rates of these reactions (which compete with each other for available solute) suggests a solution.

It is initially proposed that the d.p. of $M_{23}C_6$ + solute depeleted austenite is the equilibrium reaction in the current alloy system. It has been shown (Benz et al. 1973) that $(Fe,Mn)_{23}C_6 + \gamma$ is the equilibrium structure of the alloy Fe-40Mn-1.2C above 600°C. Since molybdenum is a stronger carbide former than manganese the formation of the carbide $(Fe,Mn,Mo)_{23}C_6$ at temperatures near 600°C in the alloy Fe-13Mn-4Mo-1.2C would be expected assuming that all other factors remain constant. In addition, it is generally considered that grain boundary nucleated reaction products formed during isothermal ageing (for example, decomposition of austenite to pearlite in Fe-C alloys) are the bona fide equilibrium phases. The nucleating sites of the d.p. products are, however, restricted to the austenite grain boundaries by the nature of the transformation reaction and during growth the colonies readily fan out and impinge upon each other.

On the other hand, the nucleation of Mo_2C is catalyzed by the presence of dislocations; a process which has been shown (Cahn 1957) to increase precipitation rates by factors up to 10^{78}. Since the precipitation of Mo_2C can occur at any site containing line defects (Fig. 4.2a) and growth is autocatalytic due to the associated formation of dislocations in the surrounding matrix, it can compete more favourably for available solute than the d.p. carbide. Evidence for this effect is shown by the almost complete elimination of the d.p. reaction by prior deformation (Section 4.3.1) and the acceleration of the heterogeneous matrix reaction (Fig. 4.10 and 4.11).

The growth of the relatively coarse d.p. reaction is effectively impeded by the presence of the heterogeneous matrix reaction ahead of the advancing colony (Fig. 4.17). In a recently proposed mechanism of d.p. (Meyrick 1976) it is suggested that the increased energy of the migrating grain boundary is compensated by solute segregation from supersaturated regions ahead of the developing colony. However, prior matrix precipitation of Mo_2C lowers this driving force for further grain boundary migration. This proposal is substantiated by observations reported by Hornbogen (1972) on alloy systems that undergo simultaneous continuous and discontinuous precipitation. It was shown that the growth of the d.p. reaction is retarded in alloys with a high degree of supersaturation by matrix precipitation ahead of the colonies and that the d.p. reaction is eliminated when the initial degree of supersaturation is lowered.

4.5 Conclusions

Both precipitation reactions examined in this work (coarse lamellar $M_{23}C_6$ and fine Mo_2C in austenite) may be described as discontinuous, heterogeneous and autocatalytic using the criteria defined in the review by Hornbogen (1972). Since the nucleation and growth of these two reaction products have been shown to occur by entirely different processes this classification is too general to adequately differentiate between the two reactions.

In the present study the term 'discontinuous precipitation' has been used to describe the cellular transformation reaction - lamellar $M_{23}C_6$ + solute depleted austenite - that nucleates at grain boundaries and propagates by boundary migration. The orientation of the carbide phase is unrelated to the austenite matrix (γ_1) but has a simple cube-cube relationship with the accompanying solute depleted austenite (γ_2) whose orientation, in turn, is continuous across the original γ_1/γ_2 grain boundary. The adjective discontinuous refers to the composition (and lattice parameter) of the austenite which changes in a discontinuous manner from supersaturated γ_1 to solute depleted γ_2 across the reaction front. The process may also be described as heterogeneous since nucleation is restricted to grain boundaries and as autocatalytic by the nature of the migrating grain boundary process.

On the other hand the term 'heterogeneous matrix precipitation' has been used to describe the formation of Mo_2C in austenite. In this case the orientation of the carbide phase is related to the original austenite matrix and there is no sharply defined interface between the supersaturated and solute depleted austenite regions. Precipitation is not restricted to grain boundaries but occurs at point, line and areal defects in the matrix.

The autocatalytic progress of the reaction can be elucidated by the assumption that dislocations in the austenite emanate from the Mo_2C particles and serve as nucleating sites for further transformation.

4.6 Suggestions for Future Work

1. Burgers Vector analysis of the associated dislocations in the heterogeneous matrix precipitation of Mo_2C in austenite may indicate a mechanism for the reaction process and explain the observed austenite habit plane for the sheets of Mo_2C precipitates..

2. The cause of the change in morphology of the sheets of Mo_2C precipitates from particulate to fibrous at higher ageing temperatures, observed in the course of this study, is unexplained and merits a more detailed investigation.

3. The present study indicates that the solution treated alloy Fe-13Mn-7Mo-0.8C age hardens rapidly to about 500 Hv at $850^{o}C$ after prior deformation and that very little overageing occurs after 25 hours. It is envisaged that subsequent carburization of the matrix austenite to increase its carbon content to 1.2%C at this temperature will produce a steel with the characteristic toughness and work hardening capacity of Hadfield steel coupled with a high initial hardness and improved yield strength. An investigation of the mechanical properties of this alloy under these conditions should be carried out because of its potential practical significance.

APPENDIX 1

1. EXPERIMENTAL TECHNIQUES

1.1 Material preparation

The alloys used in this work were produced from high purity base materials. Surface contaiminants and oxides present on the as-received materials were removed with the following procedures:-

Iron Pickled in 20% sulphuric acid at 50°C for 30 minutes, pickled in 10% sulphuric acid at 20°C for 5 minutes, rinsed in distilled water, rinsed in alcohol and dried in hot air.

Manganese Chemically polished in a solution of $HF-HNO_3-H_2O$ with a volume ratio 5-45-50 at room temperature for 2 minutes, rinsed and dried.

Molybdenum Electropolished at 10 Volts for 5 minutes in a solution containing 100 grams chromic acid, 250 mls phosphoric acid and 100 mls water, rinsed and dried.

Carbon The glazed surface layer of the spectrographically pure carbon rods were removed by abrasion.

1.2 Alloy Preparation

Ingots were produced by melting a 50 gram charge of the correct proportions of each element in an Argon arc furnace. The furnace chamber was reduced to a vacuum better than 10^{-1} torr and flushed several times with high purity Argon. Melting was carried out under a pressure of 1/5 atmosphere of Argon. Residual impurities in the Argon gas were removed by melting a Titanium getter in the furnace

chamber for 10 minutes prior to alloying. The charge was melted for 2 minutes to form an ingot approximately 60 mms long and 12 mms in diameter in a boat shaped impression on a copper hearth. After solidification the ingot was bridged at right angles across the impression and remelted from the centre and the molten metal directed to the extremities of the mould. This procedure was repeated six times to ensure an even distribution of the alloying additions. Since some manganese, which is highly volatile in the molten state, evaporated during the melting process an additional 10% by weight was added to the change prior to melting to compensate for this loss.

1.3 Homogenization

The ingot was hot rolled into an 8 mm diameter rod and the oxidized surface layer removed by grinding and followed by ultrasonic cleaning to remove adhering particles. The rod was sealed in a reuseable mullite tube under a partial pressure of Argon and homogenized at a temperature just below the solvus line for 100 hours. Metallographic examination of the homogenized rod showed an even distribution of undissolved carbides throughout its length.

1.4 Alloy Fabrication

The 8 mm diameter rod was reduced in stages to 3.2 mm by swaging through a range of dies at 1200^{o}C. Final sizing and removal of the oxidized surface layer was obtained by machining to 3.0 mm diameter on a lathe using a tungsten carbide cutting tool.

1.5 Solution Treatment and Ageing

Sections of the 3.0 mm diameter rod were encapsulated in silica tubing under a partial pressure of Argon and soaked at a temperature just above the solvus line for at least one hour and water quenched. The solution treated rods were mounted onto a holding block with epoxy resin and sectioned into 2 mm lengths using a water cooled silicon carbide cutting disc. The epoxy resin was removed by immersion in a bath of trichloroethylene. The samples were re-encapsulated in silica tubing in vacuo for ageing which was subsequently terminated by water quenching. All samples were solution treated by positioning in the same location in one furnace and aged in a bank of identical furnaces regulated by reliable proportional controllers and constantly monitored by a multi-point recorder. The actual furnace temperature was measured with an accurate digital indicator connected to a calibrated thermocouple in close proximity to the specimen and was found to be within $\pm$ 2 degree Celsius of the set points at all times.

1.6 Optical Metallography

Optical specimens were prepared by mounting in cold setting resin and mechanically polishing in the usual manner to a one micron finish. The etchants used were 2% Nital or a saturated Picral solution containing 5% HCl. Optical examination and microphotography were conducted on a Zeiss Ultraphot II microscope. The volume fraction of phases present in the microstructures were determined using the 'point counting' technique; a transparency containing 1500 points was mounted on the projector screen of the microscope and the analysis determined at a magnification of 100 diameters.

1.7 Hardness Testing

A Vickers Hardness testing machine was used with a 10 Kg load and a pyramidal diamond indenter for all gross hardness testing. The specimens were prepared by mounting in cold setting resin and polished to an 8 micron finish. A Vickers Microhardness Tester was used with a 200 gram load for all microhardness testing. Specimens were mechanically polished to a one micron finish and finally electropolished at 20 Volts for 5 minutes at $0^{o}C$ in a solution of 10% perchloric acid - 20% glycerol - 70% ethanol. This was necessary to remove any surface deformation induced by mechanical polishing. All hardness values reported were a mean of five or more impressions.

1.8 Electron Microscopy

Replica and thin foil studies were undertaken on a Philips EM200 electron microscope operating at 80kV and 100kV respectively. This instrument was equipped with a beam tilt facility which was used for either magnetic correction or dark field studies. The specimen holders were a double tilt ($\pm 30^{o}, \pm 30^{o}$) stage and a rotating tilt (350^{o}, $\pm 30^{o}$) stage. Image magnifications were determined from a cross grating replica and the image rotation between the bright field and the electron diffraction pattern was calculated from a superimposed exposure of an MoO_3 crystal and its diffraction pattern. The camera constants of the diffraction patterns were determined for a number of lens settings using a thin polycrystalline gold foil.

1.9 Extraction replicas

Discs 3.0 mm diameter and one mm thick were electropolished under the conditions outlined in section 1.7 and lightly etched with saturated picral containing 5% HCl. A thin layer of carbon was vapour deposited on the etched surface in an Edwards Vacuum Coating Unit.

The carbon film was scored into 1 mm squares and released from the specimen surface by electropolishing at 7 Volts at 20°C for 10 seconds in a solution of 10% HCl - ethanol. The replicas were stripped off the specimen surface in distilled water and collected on electron microscope grids for examination.

1.10 Thin foils

Rods of aged material, 3.0 mm diameter, were sectioned into 0.5 mm thick discs with a water cooled silicon carbide cutting wheel. The discs were wet ground with 1200 grade emery paper to a thickness of 0.05 mm using a holder equipped with a calibrated micrometer screw push rod. The centres of the discs were reduced to approximately 0.01 mm in thickness by dishing in a commercially available Fishione twin jet electropolishing unit using the solution and conditions outlined in section 1.7. The dished specimens were finally perforated by electropolishing in the same solution while being supported by 'Lacomit' coated tweezers between two stainless steel cathodes spaced 40 mms apart. The Voltage ranged from 15 to 25 volts and the temperature of the solution was varied from -5°C to -25°C depending on the phases present in the microstructures. Multiperforated specimens with thin regions suitable for transmission electron microscopy were obtained between the perforations. Immediate washing of the thin foils on removal from the electropolishing solution was found to be absolutely critical in order to eliminate etching. A recommended practice of immersion in chilled (-20°C) ethanol followed by rinsing with a copious quantity of water free ethanol from a wash bottle and drying in a stream of warm air was found to be satisfactory.

APPENDIX 2

SOLUBILITY OF MOLYBDENUM IN AUSTENITIC MANGANESE STEEL.

Experimental Procedure

The following alloys were prepared using the procedures described in Appendix 1:

Fe-13Mn-2Mo-0.8C	Fe-13Mn-2Mo-1.2C
Fe-13Mn-4Mo-0.8C	Fe-13Mn-4Mo-1.2C
Fe-13Mn-6Mo-0.8C	Fe-13Mn-6Mo-1.2C
Fe-13Mn-8Mo-0.8C	Fe-13Mn-8Mo-1.2C
Fe-13Mn-10Mo-0.8C.	

Solvus Line

The alloys were encapsulated in silica tubing and solution treated at 1300^{o}C for one hour to ensure complete dissolution of the carbide phase. Approximate solubility limits were initially obtained by reducing the furnace temperature by 50^{o}C intervals, holding for 2 hours and water quenching. Each specimen was examined metallographically for the presence of undissolved carbides. This procedure was then repeated at 10^{o}C invervals over the previously determined 50^{o}C ranges and the solvus line constructed as a function of the molybdenum content.

Solidus Line

The solidus line was determined in a similar manner. The alloys were solution treated at 1200^{o}C for one hour and the furnace temperature raised by 10^{o}C intervals, held for one hour and water quenched. The onset of grain boundary melting was determined metallographically and the solidus line constructed as a function of molybdenum content. The solubility of molybdenum in austenitic manganese steels is illustrated in Fig. 3.1 .

APPENDIX 3

CRYSTALLOGRAPHIC TECHNIQUES

3.1 Analysis of Kikuchi Patterns

In this work Kikuchi patterns, which occurred prominently in the austenite phase, were utilized in electron diffraction analysis in preference to spot patterns. There are a number of significant advantages in the use of Kikuchi patterns:-

(a) The accuracy of the direction of the electron beam axis determined with the aid of Kikuchi lines is within $\pm 0.1^{o}$ (Ryder et al. 1968). This compares with an error of $\pm 5^{o}$ using spot patterns (Thomas 1965).

(b) The Kikuchi pattern for a given orientation is unique in the majority of cases and the 180^{o} ambiguity associated with spot patterns is eliminated, (Otte et al. 1964).

(c) It is possible to obtain an orientation relationship between two structures using only a single Kikuchi pattern from each phase and without the necessity of tilting to a low index zone axis (Von Heimendahl et al. 1964). This procedure minimizes contamination of the specimen in the electron beam.

(d) Tilting through reciprocal space in a known direction can be systematically carried out with the aid of Kikuchi lines. This is invaluable in obtaining two beam conditions for contrast analysis and at the same time permitting precise determination of the foil orientation. This process is not possible with a two beam spot pattern (Levine et al. 1966).

(e) Since Kikuchi patterns occur readily in thicker regions of the foil where spot patterns are not detected, the effective working area of the thin foil available for analysis is increased.

The analysis of Kikuchi patterns has been greatly facilitated by the development of computer drawn Kikuchi maps (Bomback et al. 1971, Young et al. 1972). The beam direction may be obtained by comparing the Kikuchi pattern with the Kikuchi map of the corresponding crystal structure. However, several difficulties were encountered with the use of these maps. Firstly, the computer drawn Kikuchi maps were based on a standard [001] stereographic projection which is only an approximation of the actual distribution of Kikuchi lines in space. The degree of distortion of the lines on the maps increases with angular distance from the [001] zone axis and is significant at orientations greater than 20^{o} from this axis (Hirsch et al. 1965). Secondly, a number of high indice planes, for example (642), which were frequently observed on Kikuchi patterns are not included in the published maps. Thirdly, the line spacings between Kikuchi pairs obtained in the austenite phase at 100KV differed widely from those on the computer drawn map which was based on copper at 500KV. In addition, the calibration constant of the Kikuchi patterns, which is a function of the camera constant of the electron microscope, differed from that of the Kikuchi map. Finally, there are more accurate methods available for the beam axis determination than that obtained by a simple comparison with the Kikuchi map (von Heimendahl et al. 1964, Johari et al. 1969, Okamoto et al. 1967).

These difficulties were overcome by developing a method of indexing Kikuchi patterns analytically using the measured angles between diffracting planes. The Kikuchi map was simplified and rendered universally applicable

to all F.C.C. structures at any camera length by utilising the medians of the Kikuchi line pairs (Hirsch et al. 1965). The indexed standard triangle, bounded by the poles $[001]$ - $[011]$ - $[\bar{1}11]$, used in all analyses is shown in Fig. A3.1. A computer program was devised to determine the trace of the planes of the F.C.C. structure that pass through the standard triangle and to calculate the angles between planes whose zone axes lie within the bounds of the triangle. By disregarding the planes that do not pass through the triangle and the angles between planes that pass through the triangle but intersect outside its limits, the tedious and time consuming trial and error method of indexing Kikuchi lines, (Otte et al. 1964), was eliminated. The calculated acute angles between intersecting Kikuchi lines satisfying these conditions and indexed in Fig. A3.1 are listed in Table A3.1.

All Kikuchi patterns were initially analysed in terms of this standard triangle. However, there were two possible cases in which the determined zone axis of the pattern had to be further modified:-

(a) In some instances the Kikuchi patterns obtained were a mirror image of the corresponding patterns on the map (Otte et al. 1964). The standard pattern could be achieved by inverting the thin foil in the specimen holder in the electron microscope. However, this procedure may be carried out analytically using matrices (Jaswon 1965).

$$[B] = [A]\ [J]\ [(hkl)^{\frac{1}{2}}]$$

where A is the zone axis in the standard triangle

B is the zone axis of the mirror image

J is an inversion operator

$(hkl)^{\frac{1}{2}}$ is a rotation through 180° about a pole normal to the $[001]$ standard projection, e.g. $[100]$.

$$[B] = [A] \begin{bmatrix} \bar{1} & . & . \\ . & \bar{1} & . \\ . & . & \bar{1} \end{bmatrix} \begin{bmatrix} 1 & . & . \\ . & \bar{1} & . \\ . & . & \bar{1} \end{bmatrix} = [A] \begin{bmatrix} \bar{1} & . & . \\ . & 1 & . \\ . & . & 1 \end{bmatrix}$$

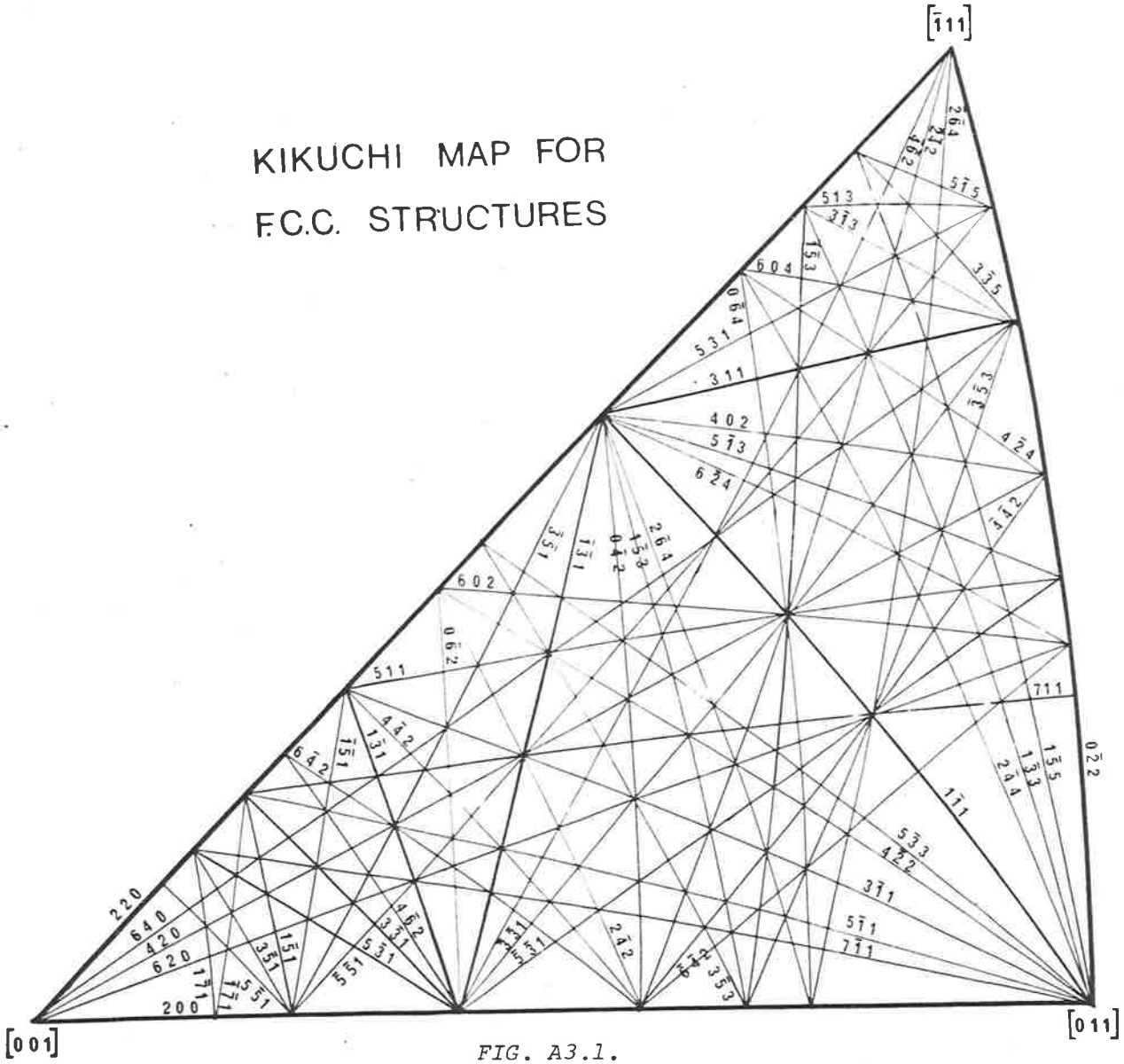

FIG. A3.1.

TABLE A3.1

	$1\bar{1}1$	200	220	$0\bar{2}2$	311	$3\bar{1}1$	$1\bar{3}1$	$\bar{1}\bar{3}1$	$3\bar{1}3$	$1\bar{3}3$	$3\bar{3}1$	$\bar{3}\bar{3}1$	420	402	$0\bar{4}2$
1—1 1		55	90	35	59	29		59		22		82	75	39	39
2 0 0	55		45	90		25	72	72		77	47	47	27		90
2 2 0	90	45		60	31	65	65	31	71	71	90			51	51
0-2 2	35	90	60		90	65			50	13		50	72	72	
3 1 1	59		31	90				63	40	78		40		19	82
3-1 1	29	25	65	65			50	85		51		70	48		66
1-3 1		72	65			50		35			26	61	82		
-1-3 1	59	72	31		63	85	35				61	26	48	82	19
3-1 3			71	50	40					38		81			
1-3 3	22	77	71	13	78	51			38			62	84	59	
3-3 1		47	90				26	61				87	72		
-3-3 1	82	47		50	40	70	61	26	81	62	87		23	59	44
4 2 0	75		18	72		48	82	48		84	72	23		37	66
4 0 2	39		51	72	19			82		59		59	37		78
0-4 2	39	90	51		82	66		19				44	66	78	
4-2 2	19	35	73	55		10		76		41		79	57		57
2-4 2		66	73			42		42				68	90		24
-2-4 2	62	66	30	30	61	90			79	41		21	43	79	24
5 1 1	56		35	90		29	80	66		77		41	19		85
5-1 1	39	16	57	74		9	59	87		61	33	61	39		75
1-5 1		79	57								33		75		
-1-5 1		79	35			80	29				55		53		
5 3 1	73		17	76	14			49	54	88				34	68
5 1 3			44	76					27	65					
5-1 3	29		61	61	30			87		49		70	47	11	68
5-3 1		32	76				40	75			14	79	58		
1-5 3	29	80	61		87	56		30				54	77	68	11
-1-5 3	47	80	44		75	75			65	27		35	58	86	
-5-3 1	84	32		61		56	75	40		74	79	14			58
3-5 1		60	76										86		
-3-5 1	73	60	17		49	81	49	14			74		34	68	34
2-4 4	16	71	76	19	72	45				6		68	90	53	
4-2 4			76	45	45					33		86	83	27	
4-4 2		48	90			25	25	60				86	73		42
-4-4 2	79	48		45		72				58			27	63	42
6 2 0	69		27	77		40	90	55		90	84	29	8		74
6 0 2	43		48	77				79		84		55	32		82
0-6 2		90	48			68	18	18			43	43	65		
5-3 3	14	40	78	50		15		71		36		84	61		52
3-5 3		63	78			39		46				72	86		28
3-3 5			90	30	60				19			80			
-3-5 3	64	63		30	60	87			80	43		19	41	78	
5-1 5			67	54											
5-5 1		46	90										72		
1-5 5	27	82	67	8	83	57			42	5		57	79	64	
-5-5 1	85	46		54	37	68	62	28	77	65	88		20	56	46
7 1 1	56		38	90		28	78	68		77	52	42	20		86
7-1 1	43	11	54	79		14	62	83		65	37	57	36		78
1-7 1		82	54										72		
-1-7 1		82	38								52		56		
6 4 0	81		11	67	23	54	75	41	64	79	79	17		42	60
6 0 4			54	67	23				17	55		64			
0-6 4	37	90	54		85	65						48	68	78	
6-2 4	22		68	55	36			81		43		76	53	17	61
6-4 2		37	79				36	71				83	61		53
4-6 2		58	79				15	50			11	76	83		
2-6 4	22	74	68		81	50		36				61	83	61	17
-2-6 4	52	74	41	19	71	81			68	31		31	53	90	
-4-6 2	72	68	19	41	50	81	50	15	90	52	76	11	33	68	33
-6-4 2	90	37		55		61				68					53

Angles between intersecting Kikuchi Lines within the standard triangle $[001]$ - $[011]$ - $[\bar{1}11]$.

TABLE A3.1 continued

	$4\bar{2}2$	$2\bar{4}2$	$\bar{2}\bar{4}2$	511	$5\bar{1}1$	$1\bar{5}1$	$\bar{1}\bar{5}1$	531	513	$5\bar{1}3$	$5\bar{3}1$	$1\bar{5}3$	$\bar{1}\bar{5}3$	$\bar{5}\bar{3}1$	$3\bar{5}1$
1-1 1	19		62	56	39			73		29		29	47	84	
2 0 0	35	66	66		16	79	79				32	80	80	32	60
2 2 0	73	73	30	35	57	57	35	17	44	61	76	61	44		76
0-2 2	55		30	90	74			76	76	61				61	
3 1 1			61					14		30		87	75		
3-1 1	10	42	90	29	9		80					56	75	56	
1-3 1				80	59		29				40			75	
-1-3 1	76	42		66	87			49		87	75	30		40	
3-1 3			79					54	27				65		
1-3 3	41		41	77	61			88	65	49			27	74	
3-3 1					33	33	55				14			79	
-3-3 1	79	68	21	41	61					70	79	54	35	14	
4 2 0	57	90	43	19	39	75	53			47	58	77	58		86
4 0 2			79					34		11		68	86		
0-4 2	57	24	24	85	75			68		68		11		58	
4-2 2		34	80	38	19							46	66	66	
2-4 2	34		48	72	51									82	
-2-4 2	80	48		62	81			46	74	90		34	15	34	
5 1 1	38	72	62				71			29		84	77	29	
5-1 1	19	51	81			66	88					65	84	47	
1-5 1					66		22				47				19
-1-5 1				71	88	22					69				42
5 3 1			46						28	44		78	61		
5 1 3			74					28					88		
5-1 3			90	29				44				57	75	57	
5-3 1						47	69							65	28
1-5 3	46		34	84	65			78		57			19	68	
-1-5 3	66		15	77	84			61	88	75		19		49	
-5-3 1	66	82	34	29	47					57	65	68	49		
3-5 1						19	42				28				
-3-5 1	90	56		52	73	42	19	34		78	88	44			61
2-4 4	35		47	71	55			87		43			32	80	
4-2 4			74					60					60		
4-4 2		18	66	55	33		55							80	
-4-4 2	82	66	18	45	63					74		52	32	17	
6 2 0	50	83	50		32	83	61				50	84	69	16	78
6 0 2	25	59	75	13								71	90	42	
0-6 2	59	25		83	76						58			58	
5-3 3	5		76	43	25							42	61	70	
3-5 3	29		51	66	48							17	37	86	
3-3 5			60					74	46						
-3-5 3	83			60	78					89		37	17	32	
5-1 5			83					50	23						
5-5 1						33	56								14
1-5 5	47		37	82	66			83	69	54				69	
-5-5 1	77	70	24	39	59	56	33	23	50	66	78	57	39		75
7 1 1	37	70	63		19	85	73					83	78	29	
7-1 1	24	55	77		4	69	88				23	69	89	43	50
1-7 1											50				23
-1-7 1					85	19					66				39
6 4 0	63	83	38	25	46	68	46			52	65	71	52		87
6 0 4			83					37					82		
0-6 4	56		25	87	75			71		65			10	59	
6-2 4			84	35				51		8		51	69	63	
6-4 2		29	77		22		66							69	
4-6 2					44		44				25			90	
2-6 4	40		40	78	59			85		51		6	25	74	
-2-6 4	71		11	72	90			57	85	80				44	
-4-6 2	90	57	11	52	72			36	63	80	90	44	25	25	
-6-4 2	71	77	29		52							63	44		

TABLE A3.1 continued

	$\bar{3}\bar{3}1$	$2\bar{4}4$	$4\bar{2}4$	$4\bar{4}2$	$\bar{4}\bar{4}2$	620	602	$0\bar{6}2$	$5\bar{3}3$	$3\bar{5}3$	$3\bar{3}5$	$\bar{3}\bar{5}3$	$5\bar{1}5$	$5\bar{5}1$	$1\bar{5}5$
1-1 1	73	16			79	69	43		14			84			27
2 0 0	60	71		48	48	18		90	40	63		63		46	82
2 2 0	17	76	76	90			48	48	78	78	90		67	90	87
0-2 2		18	45		45	77	77		50		30	30	54		8
3 1 1	49	72	45								60	60			83
3-1 1	81	45		25	72	40		68	15	39		87			57
1-3 1	49			25		90		18							
-1-3 1	14			60		55	79	18	71	46					
3-1 3											19	80			42
1-3 3		6	33		56	90	64		36			43			5
3-3 1	74					64		43							
-3-3 1		68	86	86		29	55	43	84	72	80	19			57
4 2 0	34	90	63	73	27		32	65	61	86		41		72	79
4 0 2	68	53	27		63							78			64
0-4 2	34			42	42	74	82		52	28					
4-2 2	90	35			82	50	25	58	5	29		83			47
2-4 2	56			18	66	83	59	25							
-2-4 2		47	74	66	18	50	75		76	51	60		83		37
5 1 1	52	71		55	45		13	83	43	88		80			82
5-1 1	73	55		33	63	32		76	25	48		78			66
1-5 1	42					83								33	
-1-5 1	19			55		61								56	
5 3 1	34	87	60								74		50		83
5 1 3											48		23		69
5-1 3	78	43			74							89			54
5-3 1	88					50		58							
1-5 3	44				52	84	71		42	17		37			
-1-5 3		32	60		32	65	90		61	37		17			
-5-3 1		80		80	17	16	42	58	70	86		32			69
3-5 1	61					78								14	
-3-5 1				74		42	65	31	86	61				75	
2-4 4			27		84	84	58		30			49			11
4-2 4		27			90							75			37
4-4 2	74				84	65		42							
-4-4 2		64	90	84		33	58		87	69		15			53
6 2 0	42	84		65	33		26	73	55	79		48		64	85
6 0 2	65	58			58	26		84	30	55		73			69
0-6 2	31			42		73	84								
5-3 3	86	30			87	55	30			25		78			42
3-5 3	61				69	79	55		25			54			
3-3 5												61	23		23
-3-5 3		49	75		15	48	73		78	54	61				38
5-1 5											23				47
5-5 1	75					64									
1-5 5		11	37		53	85	69		42		23	38	47		
-5-5 1	14	71	82	87		28	52	45	81	74	84		73	89	81
7 1 1	54	71		53	46	13		85	42	68		61			82
7-1 1	69	58		37	59	28		80	29	52		74			71
1-7 1						80								36	
-1-7 1						64								53	
6 4 0	27	85	68	79			38	58	68	88	83	37		79	74
6 0 4		50	22								37	83			60
0-6 4		22	50		42	75	80		51			27			
6-2 4	85	37			80	47	22					85			48
6-4 2	85			11	85	54		54							
4-6 2	63					75		32							
2-6 4	51				58	90	65		35			43			
-2-6 4		37	64		27	80	85		66		49	12	73		28
-4-6 2		58	85	74		40	65	32	85	61	71		86		48
-6-4 2		74		85	11	22	47		76	81		26			63

TABLE A3.1 continued

	$\bar{5}\bar{5}1$	711	$7\bar{1}1$	$1\bar{7}1$	$\bar{1}\bar{7}1$	640	604	$0\bar{6}4$	$62\bar{4}$	$6\bar{4}2$	$4\bar{6}2$	$2\bar{6}4$	$\bar{2}\bar{6}4$	$\bar{4}\bar{6}2$	$\bar{6}\bar{4}2$
1-1 1	85	56	43			81		37	22			22	52	72	90
2 0 0	46		11	82	82	34		90		37	58	74	74	58	37
2 2 0		38	54	54	36		54	54	68	79	79	68	41	19	
0-2 2	54	90	79			67	67		55				19	41	55
3 1 1	37					23	23	85	36			81	71	50	
3-1 1	68	28	14			54		65				50	81	81	61
1-3 1	62	76	62			75				36	15			50	
-1-3 1	26	68	83			41			81	71	50	36		15	
3-1 3	77					84	17						68	90	
1-3 3	65	77	65			79	55		43				31	52	68
3-3 1	88	52	37		52	79					11			76	
-3-3 1		42	57			17	64	46	76	83	76	61	31	11	
4 2 0	20	20	36	72	56	7		68	53	61	83	83	53	33	
4 0 2	56					42		76	17			81	90	69	
0-4 2	46	86	79			60			61	53		17		33	53
4-2 2	77	37	24			63		56				40	71	90	71
2-4 2	70	70	55			83				29				57	77
-2-4 2	24	63	77			38	83	25	84	77		40	11	11	29
5 1 1	39					25		87	35			78	72	52	
5-1 1	59	19	4		85	46		75		22	44	59	90	72	52
1-5 1	56	85	69		19	68									
-1-5 1	33	73	88			46				66	44				
5 3 1	23						37	71	51			85	57	38	
5 1 3	50												85	83	
5-1 3	66					52		65	6			51	80	80	
5-3 1	78		23	50	66	65					25			90	
1-5 3	57	83	69			71			51			6		44	63
-1-5 3	39	78	89			52	82	10	69			25		25	44
-5-3 1		29	43					59	63	69	90	74	44	25	
3-5 1	75		50	23	39	87									
-3-5 1	14	54	69			27			85	85	63	51			
2-4 4	71	71	59			85	50	22	37				37	58	74
4-2 4	82					68	22	50					64	85	
4-4 2	87	53	37			79				11				74	85
-4-4 2		46	59					42	80	85		58	27		11
6 2 0	28	13	28	80	64	15		75	47	54	75	90	60	40	22
6 0 2	52					36		80	22			65	85	65	47
0-6 2	45	85	80			58				54	32			32	
5-3 3	81	42	29			68		51				35	86	85	76
3-5 3	74	66	52			88								61	81
3-3 5	84					83	37						49	71	
-3-5 3		61	74			37	83	27	85			43	12		26
5-1 5	73												73	86	
5-5 1	89			36	53	79									
1-5 5	81	82	71			74	60		48				26	48	83
-5-5 1		40	55			14	60	49	73	81	77	83	35	13	
7 1 1	40				75	27		88		42	63	77	73	53	35
7-1 1	55			73	89	42		79		26	48	63	86	68	48
1-7 1			73		16	65									
-1-7 1		75	89	16		49									
6 4 0	14	27	42	65	49		46	63	59	68	90	77	48	27	
6 0 4	60					46		72					86	73	
0-6 4	49	88	79			63	72		59			16	16	35	54
6-2 4	73					59		59				44	73	86	89
6-4 2	81	42	28			68					22			86	73
4-6 2	77	63	48			90				22				65	
2-6 4	63	77	63			77		16	44				31	50	69
-2-6 4	35	73	86			48	86	16	73			31		22	38
-4-6 2	13	53	68			27	73	35	86	86	65	50	22		
-6-4 2		35	48					54	89	73		69	38		

(b) Orientations of zone axes that were obtained outside the standard triangle during tilting operations were derived by symmetry operations. These rotations, for both the standard triangle (A) and the mirror image (B), are illustrated in the [001] projection in Fig. A3.2. The matrix form of the symmetry rotations are shown in Table A3.2.

The zone axes of the indexed Kikuchi pattern were determined analytically using Levine's simplification of the von Heimendahl technique. The procedure involved the solution of 3 simultaneous equations of the form:-

$$\cos\theta = \frac{pu + qv + rw}{\sqrt{u^2 + v^2 + w^2}}$$

where [pqr] is the beam direction

[uvw] is an indexed pole on the Kikuchi pattern

θ is the measured angle between [pqr] and [uvw].

In some cases when 3 different poles were not obtained on the Kikuchi pattern, for example at orientations near the [011] zone axis, the pattern was located on the Kikuchi map (with the same calibration constant) and the beam axis determined using the Okamoto (1967) relation:-

$$p : q : r = \cos\beta : \sin\beta\cos\alpha : \sin\alpha\sin\beta$$

where α is measured directly

β is determined using the calibration constant of the Kikuchi map.

Fig. A3.2

[001] Stereographic Projection.

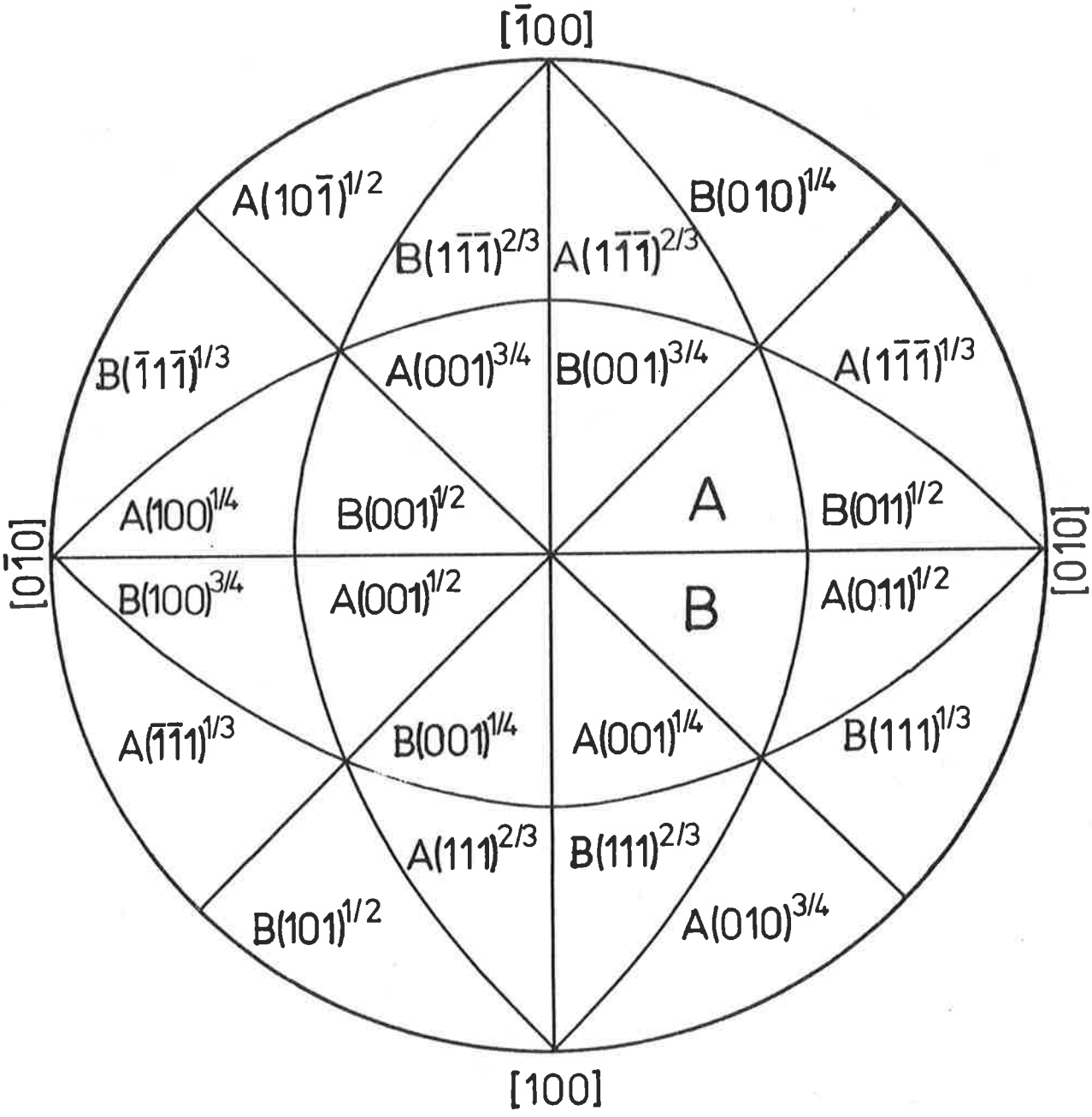

Location of symmetry rotations and reflection operations of zone axes in the standard triangle A .

$$[B] = [A][J] \quad [(100)^{\frac{1}{2}}] \ .$$

TABLE A3.2

Matrix representation of the symmetry rotations illustrated in the [001] Stereographic Projection in Fig. 3.2.

$$(100)^{\frac{1}{4}} = \begin{bmatrix} 1 & . & . \\ . & . & \bar{1} \\ . & 1 & . \end{bmatrix} \qquad (100)^{\frac{1}{2}} = \begin{bmatrix} 1 & . & . \\ . & \bar{1} & . \\ . & . & \bar{1} \end{bmatrix} \qquad (100)^{3/4} = \begin{bmatrix} 1 & . & . \\ . & . & 1 \\ . & \bar{1} & . \end{bmatrix}$$

$$(010)^{\frac{1}{4}} = \begin{bmatrix} . & . & 1 \\ . & 1 & . \\ \bar{1} & . & . \end{bmatrix} \qquad (010)^{\frac{1}{2}} = \begin{bmatrix} \bar{1} & . & . \\ . & 1 & . \\ . & . & \bar{1} \end{bmatrix} \qquad (010)^{3/4} = \begin{bmatrix} . & . & \bar{1} \\ . & 1 & . \\ 1 & . & . \end{bmatrix}$$

$$(001)^{\frac{1}{4}} = \begin{bmatrix} . & \bar{1} & . \\ 1 & . & . \\ . & . & 1 \end{bmatrix} \qquad (001)^{\frac{1}{2}} = \begin{bmatrix} \bar{1} & . & . \\ . & \bar{1} & . \\ . & . & 1 \end{bmatrix} \qquad (001)^{3/4} = \begin{bmatrix} . & 1 & . \\ \bar{1} & . & . \\ . & . & 1 \end{bmatrix}$$

$$(110)^{\frac{1}{2}} = \begin{bmatrix} . & 1 & . \\ 1 & . & . \\ . & . & \bar{1} \end{bmatrix} \qquad (101)^{\frac{1}{2}} = \begin{bmatrix} . & . & \bar{1} \\ . & \bar{1} & . \\ 1 & . & . \end{bmatrix} \qquad (011)^{\frac{1}{2}} = \begin{bmatrix} \bar{1} & . & . \\ . & . & 1 \\ . & 1 & . \end{bmatrix}$$

$$(1\bar{1}0)^{\frac{1}{2}} \quad \begin{bmatrix} . & \bar{1} & . \\ \bar{1} & . & . \\ . & . & \bar{1} \end{bmatrix} \qquad (10\bar{1})^{\frac{1}{2}} = \begin{bmatrix} . & . & \bar{1} \\ . & \bar{1} & . \\ \bar{1} & . & . \end{bmatrix} \qquad (01\bar{1})^{\frac{1}{2}} = \begin{bmatrix} \bar{1} & . & . \\ . & . & \bar{1} \\ . & \bar{1} & . \end{bmatrix}$$

$$(111)^{1/3} = \begin{bmatrix} . & . & 1 \\ 1 & . & . \\ . & 1 & . \end{bmatrix} \qquad (\bar{1}11)^{1/3} = \begin{bmatrix} . & . & \bar{1} \\ 1 & . & . \\ . & \bar{1} & . \end{bmatrix} \qquad (1\bar{1}\bar{1})^{1/3} = \begin{bmatrix} . & . & \bar{1} \\ \bar{1} & . & . \\ . & 1 & . \end{bmatrix} \qquad (\bar{1}1\bar{1})^{1/3} = \begin{bmatrix} . & . & 1 \\ \bar{1} & . & . \\ . & \bar{1} & . \end{bmatrix}$$

$$(111)^{2/3} = \begin{bmatrix} . & 1 & . \\ . & . & 1 \\ 1 & . & . \end{bmatrix} \qquad (\bar{1}\bar{1}1)^{2/3} = \begin{bmatrix} . & 1 & . \\ . & . & \bar{1} \\ \bar{1} & . & . \end{bmatrix} \qquad (1\bar{1}\bar{1})^{2/3} = \begin{bmatrix} . & \bar{1} & . \\ . & . & 1 \\ \bar{1} & . & . \end{bmatrix} \qquad (\bar{1}1\bar{1})^{2/3} = \begin{bmatrix} . & \bar{1} & . \\ . & . & \bar{1} \\ 1 & . & . \end{bmatrix}$$

3.2 Orientation Relationship Between Cementite and Austenite

3.2.1 Experimental Procedure

(a) A low index zone axis of cementite was accurately obtained by tilting until a concentric ring of the first order Laue zone was observed around the central spot pattern. Arcs of high order Laue zones which were visible within $\pm 5^{o}$ of the zone axis were used to indicate the required tilt direction.

(b) A Kikuchi pattern of the austenite adjacent to the cementite was also taken at the same tilt conditions and indexed using the procedure outlined in Appendix 3.1. In general an irrational indice zone axis was obtained and this was found to be ideal for accurate analysis and the elimination of the 180^{o} ambiguity in the austenite.

(c) The specimen was tilted approximately 30^{o} and a second series of diffraction patterns obtained. This final procedure eliminated the 180^{o} ambiguity in the cementite diffraction patterns.

The accuracy of this technique is indicated by comparing the calculated angles between the two determined zone axes of each phase.

Cementite Zone Axis		Austenite Zone Axis	
$[1\ 0\ 2]$	34.77^{o}	$[\bar{1}3\ 17\ 98]$	35.12^{o}
$[2\ 0\ 1]$		$[31\ \bar{2}4\ 92]$	

The calculated angles between the zones of cementite and austenite differ by only 0.35^{o} over a 35^{o} tilt.

3.2.2 Orientation Relationship

By convention the orientation relationship between cementite and austenite is described by defining the austenite directions that are parallel to the principal axes of the cementite. These directions obtained by graphical methods (Stereographic Projection) are subject to $\pm 2^{o}$ error, (Johari et al. 1969). A more accurate analytical approach using matrices outlined by Jaswon et al. (1948) that described the transformation of axes from one cubic system to another cubic system was modified to suit the cubic/orthorhombic system.

Parallel zones or directions $[u \ v \ w]$ in austenite and cementite are obtained from the relation:-

$$\begin{bmatrix} u \\ v \\ w \end{bmatrix}_A = [A]^{-1}[C]\,[L]\begin{bmatrix} u \\ v \\ w \end{bmatrix}_C$$

where A and C are the transformation matrices of austenite and cementite respectively. The matrices consist of the direction cosines of the angles between the determined reference axes and the principal axes of each system.

i.e.

$$[C] = \begin{bmatrix} l_1 & l_2 & l_3 \\ m_1 & m_2 & m_3 \\ n_1 & n_2 & n_3 \end{bmatrix}$$

where l_1 is the cosine of the angle of the determined zone axis $[u_1 \ v_1 \ w_1]_C$ and the principal axis OX_C etc.

L is the matrix describing the change in lattice structure from cubic to orthorhombic.

$$[L] = \begin{bmatrix} a/N & 0 & 0 \\ 0 & b/N & 0 \\ 0 & 0 & c/N \end{bmatrix}$$

where a, b, and c are the lattice parameters of cementite and $N = (a^2 + b^2 + c^2)^{\frac{1}{2}}$:

The indices of parallel planes (h k l) in each system are obtained by the relation:-

$$\begin{bmatrix} h \\ k \\ l \end{bmatrix}_A = [A]^{-1}[C][L][P] \begin{bmatrix} u \\ v \\ w \end{bmatrix}_C$$

where $[P]$ is a matrix defining the normals to the cementite directions:-

$$[P] = \begin{bmatrix} a/bc & 0 & 0 \\ 0 & b/ca & 0 \\ 0 & 0 & c/ab \end{bmatrix}$$

An example of this approach is given below:-

The following pairs of reference axes were determined from electron diffraction patterns:-

$[1\ \ 0\ \ 2]_C$ // $[\overline{13}\ \ 17\ \ 98]_A$

$[2\ \ 0\ \ 1]_C$ // $[31\ \ \overline{24}\ \ 92]_A$

Cross multiplication yields a third set of axes:-

$[0\ \ \overline{1}\ \ 0]_C$ // $[\overline{36}\ \ \overline{39}\ \ 2]_A$

$$[A]^{-1} = \begin{bmatrix} \overline{1.1584} & 1.2579 & \overline{.6785} \\ 1.1041 & \overline{1.1424} & .7336 \\ .6783 & .3651 & \overline{.0372} \end{bmatrix}$$

$$[C][L] = \begin{bmatrix} .3181 & 0 & .9481 \\ .8019 & 0 & .5975 \\ 0 & \overline{1} & 0 \end{bmatrix} \begin{bmatrix} .4722 & 0 & 0 \\ 0 & .5310 & 0 \\ 0 & 0 & .7036 \end{bmatrix}$$

$$\begin{bmatrix} u \\ v \\ w \end{bmatrix}_A = \begin{bmatrix} .3024 & .3603 & \overline{.2439} \\ \overline{.2668} & .3895 & .2563 \\ .2401 & \overline{.0198} & .6060 \end{bmatrix} \begin{bmatrix} u \\ v \\ w \end{bmatrix}_C$$

Substition of the principal axes of cementite yields:-

$$\begin{aligned} [0\ \ 0\ \ 1]_C \quad // \quad & [\overline{2.00} \quad 2.10 \quad 4.97]_A \\ [0\ \ 1\ \ 0]_C \quad // \quad & [1.00 \quad 1.08 \quad \overline{0.06}]_A \\ [1\ \ 0\ \ 0]_C \quad // \quad & [5.04 \quad \overline{4.45} \quad 4.00]_A \end{aligned}$$

B I B L I O G R A P H Y

Aaronson, B.: Climax Molybdenum Symposium on Steel Strengthening Mechanisms (1969), 77.

Ainsley, M.H.: University of Adelaide, (1979), Unpublished work.

Ainsley, M.H, Cocks, G.J. and Miller, D.R.: Metal Science, (1979), 13, 20.

Andrews, K.W., Dyson, D.J. and Keown, S.R.: Interpretation of Electron Diffraction Patterns, (1968), Hilger & Watts Ltd., London.

Avery, H.S.: ASM Metals Handbook, (1961), Cleveland, Ohio.

Bain, E.C., Davenport, E.S. and Waring, W.N.S.: Trans. A.I.M.E., (1932) 100 , 228.

Beckitt, F.R. and Clark, B.R.: Acta Met., (1967), 15, 113

Bee, J.V.: Ph.D. Dissertation, (1974) University of Cambridge.

Bee, J.V. and Edmonds, D.V.: Metallography, (1979), 12, 3.

Benz, R., Elliot, J.F. and Chipman, J.: Met. Trans., (1973), 4, 1975.

Bernshteyn, M.L., Zaymovskiy, V.A. Kozlova, A.G. and Kolupayeva, T.L.: Russian Metallurgy (Metally), (1977). 1, 131.

Bomback, J.L. and Thomas, L.E.: J. Appl. Cryst., (1971), 4, 356.

Borland, D.W. and Honeycombe, R.W.K.: Metal Sci. J., (1970), 4, 14.

Brandon, D.G., Ralph, B., Ranganathan, S. and Wald, R.M.S.: Acta Met., (1964), 12, 813.

Cahn, J.W.: Acta Met., (1957), 5, 169.

Chaturvedi, M.C. and Honeycombe, R.W.K.: J.I.S.I., (1968), 208, 1236.

Cina, B.: Acta Met., (1958), 6, 748.

Cohen, M.: Met. Soc. A.I.M.E. (1962), 224, 638.

Collette, G., Crussard, C., Kohn, A., Plateau, J., Pomey, G., and Weisz, M: Rev. de Met., (1957), 54, 433.

Crocker, A.G.: Acta Met., (1962), 10, 113.

Darken, L.S. and Fisher, R.M.: Decomposition of Austenite by Diffusional Processes, (1962), Edited by Zackay, V.F. and Aaronson, H.I., Interscience, New York.

Daster, Y.N. and Leslie, W.C.: International Conference on the Strength of Metals and Alloys, (1979), 219.

Dautovich,D.P. and Bowles, J.S.: Acta Met., (1972), 20, 1137.

Davenport, A.T., Berry, F.G. and Honeycombe, R.W.K.: Met. Sc. J. (1968), 2, 104.

de Lamotte, E., Huang, Y. and Altstetter. C.: Trans. A.I.M.E. (1967), 239, 1625.

Demianczuk, D.W. and Aust, K.T.: Acta Met., (1975), 23, 1149.

Dippenaar, R.J.: Ph . D. Dissertation, (1970), University of Cambridge.

Dippenaar, R.J. and Honeycombe, R.W.K.: Proc. Roy. Soc ., (1973) A333, 455

Drobnjak, D.J. and Gordon Parr, J.: Met. Trans. (1970), 1, 759.

Drobnjak, D.J. and Gordon Parr, J.: Met. Trans. (1970) 1, 1521.

Filippov, M.A. and Kodes, B.N.: Fiz. Metal. Metalloved (1971), 31, 172.

Fournelle, R.A. and Clark, J.B.: Met. Trans. (1972), 3, 2757.

Freeman, S.: Ph. D. Dissertation, (1970), University of Cambridge.

Gray, J. M. and Yeo, R.B.S.: Trans. ASM, (1968), 61, 255.

Grigorkin, V.I. and Korotushenko, G.V.: Metal. i Term., (1968), No. 2. 48.

Grunes, R.L., D'Antonio, C. and Mukherjee, K.: Mater. Sci. Eng. (1972), 10, 175.

Grunes, R.L., D'Antonio, C. and Mukherjee, K.: Mater. Sci. Eng., (1972), 9, 1.

Guyot, P. and Wintenberger, M.:, J. Materials Science (1974), 9, 614.

Hall, E.R.: ASM Technical Report No. C6-17.1, (1966).

Hall, J.H.: Trans. A.I.M.E., (1929), 84, 382.

Ham, J.L.: Trans. ASM, (1945), 35, 331.

Harding, H.J. and Honeycombe, R.W.K.: J.I.S.I., (1966), 204, 259.

Heimendahl, von M., Bell, W. and Thomas, G.: J. Appl. Phys., (1964), 35, 3614.

Hillert, M.: Mechanism of Phase Transformation in Crystalline Solids, (1969), Institute of Metals Monogram, 33, 231.

Hillert, M. and Purdy, G.R.: Acta Met., (1978), 26, 333.

Hillert, M. and Lagneborg, R.: J. Materials Science, (1971), 6, 208.

Hirsch, P.B., Howie, A., Nicholson, R.B., Pashley, D.W. and Whelan, M.T.: Electron Microscopy of Thin Crystal (1965) Butterworths, Washington, D.C.

Holden, A., Bolten, J.D. and Petty, E.R.: J.IS.I., (1971), 209, 721.

Honeycombe, R.W.K.: Met. Trans., (1976), 7A, 915.

Hornbogen, E.: Trans. A.I.M.E., (1963), 227, 1411.

Hornbogen, E.: Met. Trans., (1972), 3, 2717.

Imai, Y. and Saito, T.: Sci. Rep. RITU, (1962a), A14, 92.

Imai, Y. and Saito, T.: Sci. Rep. RITU, (1962b), A14, 104.

Imai, Y. and Saito, T.: Sci. Rep. RITU, (1962c), A14, 261.

Imai, Y. and Namekata, J.: Sci. Rep. RITU, A21, 260. (1970).

Irvine, K.J. and Pickering, F.B.: Iron and Steel, (1956), 29, 1

Isobe, M.: Sci. Rep. RITU, (1951), A3, 540.

Jack, D.H.: Mater. Sci. Eng. (1974), 13, 19.

Jaswon, M.A.: Mathematical Crystallography (1965), Longmans, London.

Jaswon, M.A. and Wheeler, J.A.: Acta Cryst., (1948), 1, 216.

Johari, O. and Thomas, G.: The Stereographic Projection and its Application: (1970), Interscience, New York.

Kelly, A. and Nicholson, R.B.: Prog. Mater. Sci., (1963), 10, 149.

Kotval, P.S. and Hatwell, H.: Trans. A.I.M.E. (1969), 245, 1821.

Krivobok, V.N.: Trans. Amer. Soc. Steel Treat., (1929), 15, 893.

Kronberg, H.L. and Wilson, F.H.: Trans. A.I.M.E., (1949), 185, 501

Levine, E., Bell, W.L. and Thomas, G.: J. Appl. Physc. (1966), 37, 2141.

Lewis, M.H. and Hattersley, B.: Acta Met., (1965), 13, 1159.

Mangonon, P.O. and Thomas, G.: Met. Trans. (1970), 1, 1577.

Maratray, F.J.: Modern Castings, (May 1964), 203.

Maratray, F.J. and Norman, T.E.: Rev. de Met. (1961), 58, 489.

Meyrick, G.: Scripta Met., (1976), 10, 649.

Middleham, T.S.: Alloy Metals Review, (1964), 12, 2.

Norman, T.E., Doane, D.V. and Solomon, A.: A.F.S. Trans., (1960), 68, 287.

Nishiyama, Z.: Sci. Rep. RITU, (1935), 24, 128

Ohmori, Y., Davenport, A.T., and Honeycombe, R.W.K.: Iron and Steel Inst. of Japan, (1972), 12, 128.

Okamoto, P.R., Levine, E. and Thomas, G.: J. Appl. Phys. (1967), 38, 289.

Oliver and Boyd: Manganese Steel, (1956), London.

Otte, H.M.: Acta Met., (1957), 5, 614.

Otte, H.M., Dash, J. and Schaake, H.F.: Phys. Stat. Sol., (1964), 5, 527.

Petch, N.J.: Acta Cryst. (1953), 6, 96.

Pitsch, W.: Acta Met., (1962), 10, 79.

Pitsch, W.: Arch. Eisenhuttwes, (1963), 34, 381.

Predel, B. and Frebel, M.: Met. Trans. (1973), 4, 243.

Pumphrey, P.H. and Bowkett, K.M.: Phys. Stat. Sol., (1970), (a), 2, 339.

Pumphrey, P.H. and Edington, J.W.: Acta Met., (1974), 22, 89.

Raghavan, K.S., Sastri, S.A. and Marcinowski, M.J.: Trans. TMS-A.I.M.E., (1969), 245, 1569.

Ranganathan, S.: Acta Cryst., (1966), 21, 197.

Rao, H.R.S. and Paranjpe, V.G.: TISCO, (April 1963), 95.

Razik, N.A. Lorimer, G.W. and Ridley, N.: Acta Met., (1974), 22, 1249.

Razik, N.A. Lorimer, G.W. and Ridley, N.: Met. Trans., (1976), 7A, 209.

Remy, L.: Met. Trans. (1977), 8A, 253.

Remy, L and Pineau, A.: Met. Trans. (1974), 5, 963.

Roberts, W.N.: Trans. A.I.M.E., (1964), 230, 372.

Rohrig, V.K.: GieBerei-Praxis, Heft 7/1974.

Russell, J.V. and McGuire, F.T.: ASM Trans., (1944), 33, 103.

Ryder, P.L. and Pitsch, W.: Phil. Mag., (1968), 18, 807.

Saito, T.: Japan Iron and Steel Inst., (1972), 58, 423.

Sastri, S.A.: Proceedings of the International Conference on the Strength of Metals and Alloys (1973), Cambridge, U.K., 596.

Sastri, S.A. and Ray, R.: Met. Trans. (1974), 5, 1501.

Sedriks, A.J. and Mulhearn, T.O.: J.I.S.I., (1964), 202, 907.

Sedriks, A.J. and Mulhearn, T.O.: J.I.S.I. (1966a), 204, 142.

Sedriks, A.J. and Mulhearn, T.O.: J.I.S.I., (1966b), 204, 737.

Shackleton, D.N. and Kelly, P.M.: J.I.S.I., (1969), 207, 1253.

Silcock, J.M.: J.I.S.I. (1963), 201, 409.

Sipos, K., Remy, L. and Pineau, A.: Met. Trans. (1976), 7A, 857.

Sipos, K., Remy, L. and Pineau, A.: Scripta Met., (1975), 9, 927.

Sleeswyk, A.W.: Phil. Mag., (1966), 13, 1223.

Smith, A.E.W.: J.I.S.I., (1957), 186, 425.

Sulonen, M.: Z. Metalk., (1964), 55, 543.

Sundquist, B.E.: Met. Trans. (1973), 4, 1919.

Thomas, G.: Trans. A.I.M.E., (1965), 233, 1608.

Troiano, A.R. and McGuire, F.T.: Trans. ASM, (1943), 31, 340.

Tu, K.N.: Met. Trans. (1972), 3, 2769.

Tu, K.N. and Turnball, D.: Acta Met., (1967), 15, 369.

Venables, J.A.: Phil. Mag., (1962), 7, 35.

White, C.H. and Honeycombe, R.W.K.: J.I.S.I. (1962), 200, 457.

Young, C.T. and Lytton, J.L.: J. Appl. Phys., (1972), 43, 1408.

Young, C.T., Steele, J.H. and Lytton, J.L.: Met. Trans., (1973) 4, 2081.